

The Final Report for NAG1-1474

The Effect of Microgravity on the Growth of Lead Tin Telluride

Principal Investigator: R. Narayanan

Summary: The main objective of this research was to present a model for the prediction of the effect of the microgravity environment on the growth of Lead Tin Telluride.

The attitude change and its relation to the experimental objectives: The main objective for the AADSF experiment on USMP 3 involving LTT growth was to estimate the effect of ampoule orientation on the axial and radial segregation of tin telluride. As the furnace was not situated on a gimbal there was no possibility to reorient the ampoule during the flight. Instead the only way to change the growth orientation was to change the attitude of the orbiter. This was accomplished by vernier rocket firings.

In what follows it must be noted that the orbiter body coordinates are such that the positive z axis points outward from the 'belly', the positive 'x' axis points outwards from the nose and the positive 'y' axis points outwards from the starboard side. The furnace which was in the pay load had its axis aligned with the orbiter's 'z' axis with the hot end closest to the shuttle body. There were basically three orientations that were desired. These corresponded to the ampoule being seen as a heated from above (thermally stable-solutally unstable) configuration, the heated from below (where the instabilities were reversed from the first orientation) configuration and an 'in between' case where the ampoule axis was misaligned with respect to the orbiters 'g_z' axis.

In order to understand the role of each orbiter attitude that was requested it is necessary to have an idea of the first order effects on the residual acceleration levels on the orbiter. The center of gravity of the orbiter (CG) generally did not change very much during the USMP 3 part of the mission as the change in mass was insignificant. A displacement from the CG of the AADSF furnace and the attitude of the orbiter affected the so called 'gravity gradient' force (arising from the centrifugal component of acceleration). This gravity gradient had a major effect on the force fields which at low frequency levels (under 1 Hz) was of the order of $10^{-6} g_e$ where g_e is earth's gravity. A second major effect on the residual forces is the atmospheric drag on the orbiter. This drag can only have a deceleration effect on the vehicle and therefore affect the forces on the particles in the AADSF. This drag was itself affected by the orbiter attitude, the position of the orbiter with respect to the sun (i.e., atmospheric density) and the

orbiting path around the globe as the earth is not a perfect sphere. The deceleration and the tendency for the orbiter to get into an aerodynamically stable mode necessitated the need for vernier booster firings. The forces associated with these corrective measures were of high magnitude (roughly $10^{-3}g_e$ - $10^{-4}g_e$) and were of a high frequency (5-10 Hz).

Keeping in mind the main effects on the residual low frequency acceleration we now turn to the various attitudes that were chosen during the mission. The first attitude had a pitch of 185 degrees and a roll of 7 degrees. This attitude is roughly equal to the orbiter flying in a position of payload to earth and tail into the wind. (also called $-Z_{lv}$, $-X_{vw}$). The drag was very small and the small roll angle served mainly to offer a minor change in the gravity gradient. The cold end of the furnace was closest to earth and the effect was to have a large axial to normal ratio of the axial vector. The second attitude was meant to give a heated from below configuration. At first sight it might appear that the best attitude would be a zero degree pitch. However this was considered to be a risky attitude on account of debris. The second attitude was therefore obtained by considering a deceleration mode of the orbiter. Here the orbiter was placed in a pitch of 90 degrees with a small negative yaw of 17 degrees (in alternate terminology this amounted to an attitude of $-X_{lv}$ and $+Z_{vw}$). The pitch virtually maximized the drag on the orbiter while the yaw served the purpose of adjusting the gravity gradient on the furnace. Because the orbiter was decelerating it had the opposite effect on the fluid particles in the AADSF ampoule relative to the shuttle and the net effect was to accelerate the fluid in the cold end towards the hot end. This was equivalent of generating a thermally unstable and solutally stable configuration. Because the deceleration force was not of a high magnitude the net axial to normal ratio was not very high. Moreover the normal component of the force fields were very small and so in the actual flight one could expect that small changes in the 'dead band' could cause a substantial undesired change in the axial to normal ratio. The last attitude had a pitch of 123 degrees and the net effect of the drag was to change the orientation of the axial vector in the furnace so that it behaved as if it was tilted with respect to g_z of the shuttle. While the choice of orbiter attitudes had to do with the preferred growth direction the reasons for choosing these various growth directions or ampoule orientations resulted from preliminary work done using computational fluid dynamics.

Preliminary estimates of axis orientation using CFD: The computational fluid dynamic calculation procedure is best explained by considering Figure 1 . The ampoule liquid region is assumed to be constant as the solidification rates are normally very small. The boundary conditions indicate hot and cold zones as well as insulating zones. The far field concentration is assumed to be constant and the interface condition respects

mass conservation along with solutal segregation. The effect of the magnitude of the gravity vector is seen in Figures 2 a) and b) and we immediately conclude that the flow at low frequency low amplitude accelerations ($10^{-5}g_e$) will be of a weak torroidal type. Higher amplitude forces will cause solutal convection to come into play but such high amplitude acceleration vectors were not present at the low frequency levels during USMP 3 and were mainly associated with high frequency activities such as booster firings and water dumps. While we do not presently have any predictions on the effects of high frequency g-jitter it is clear from the order of magnitude of the calculated velocity vectors for the case of low frequency with $10^{-5}g_e$ that very little mixing takes place. The velocity is no greater than 10^{-5} cm/ sec. Given an initial liquid region size of 5 cm, this small velocity amounts to an initial mixing time of 10^6 seconds. Meanwhile the solidification is at the rate of 1 cm/ hour. When the liquid region size is about 1 cm the mixing time is about 2×10^5 seconds. Clearly this is insignificant because the entire growth period is about 2×10^4 seconds. In other words we predict that only diffusion controlled growth ought to prevail at $10^{-5}g_e$ and this more true at lower gravitational levels which were experienced during USMP 3.

The effect of a five degree offset with respect to the vertical orientation was calculated and the results are graphically shown in Fig. 2 c. What is seen from this figure is that small tilts give rise to swirling flow and this flow contains the solutal boundary layer to the depleting surface. This may be contrasted with torroidal flow in Fig. 2 a (for the vertical orientation) that sweeps the solute out of the solutal boundary layer. The solutal boundary layer contains most of the rejected SnTe and so swirling flow if anything should help by making diffusive growth more probable. In other words one might conclude that a constant off axis arrangement is better than an on axis aligned ampoule. Fig. 3 is a depiction of the mixing patterns that are seen when the ampoule is subjected to a time dependent tilt. It must be noted that the velocities are still very small and so even in the case when the tilt is a periodic function of time the growth is expected to be diffusion controlled.

In summary we have concluded that diffusive growth was predicted under low frequency g-jitter conditions. The high frequency was not studied but we did conclude that the time constant for the fastest transporting mechanism (heat transfer) was much larger than the corresponding period for high frequency (5 Hz) g-jitter.

Publications: The publications that arose from this work and directly related to the objectives are attached and are listed below:

Mallika, C**., Zhao, A-X,* and Narayanan, R., " A Numerical Model for Predicting the Effect of Gravity-Driven Convection on Mass Diffusivity Measurements in Liquid Metals", Advances in Space Research 24 N.10, p 1303 (1999)

Zhao, A-X,** Narayanan R and Fripp, A.L. " A 3D numerical model for flow profiles in a bridgman tube - the effects of constant and periodic off axis orientation in lowgravity environment, Advances in Space Research 24 N.10, 1307_(1999)

Matisak, B., Zhao, A-X.**, Narayanan, R., and Fripp, A.L., "The Microgravity Environment: Its Prediction and Interpretation and Importance to Materials Processing", J. Crystal Growth, 174, p 90, (1997)

Spin Off Research: Spin off work was accomplished in the area of microgravity effects on convection and interfacial driven convection. These have enhanced our knowledge of convection and have led to the following publications in which the grant is acknowledged :

Zaman*, A.A. and Narayanan R., " Onset of Rayleigh Marangoni Convection in a Bounded Circular Cylinder- The Three Dimensional Case", J. Colloid and Interface Science, 179, p.151, 1996

Zhao*, A-X, Moates,* C and Narayanan R., "Rayleigh Convection in a Closed Cylinder Experiments and a 3-D Model with Temperature Dependent Viscosity Effects", Physics of Fluids, 7,(7),p 1579, 1995

Wagner*.C., Zhao A-X*, Narayanan R and Friedrich.R., " Bilayer Rayleigh- Marangoni convection with and without solidification ", Proceedings of the Royal Soc. A, 451, p 487, 1995

Johnson, D.*, and Narayanan, R., .. " Marangoni Convection in Multiple Fluid Layers and Its Application to Materials Processing", invited Philosophical Transactions of the Royal Society., 356, Ser.A., N. 1739 (1998)

The asterisks are the students who were supported by this project

3D Numerical Model for Flow in a Bridgman Tube

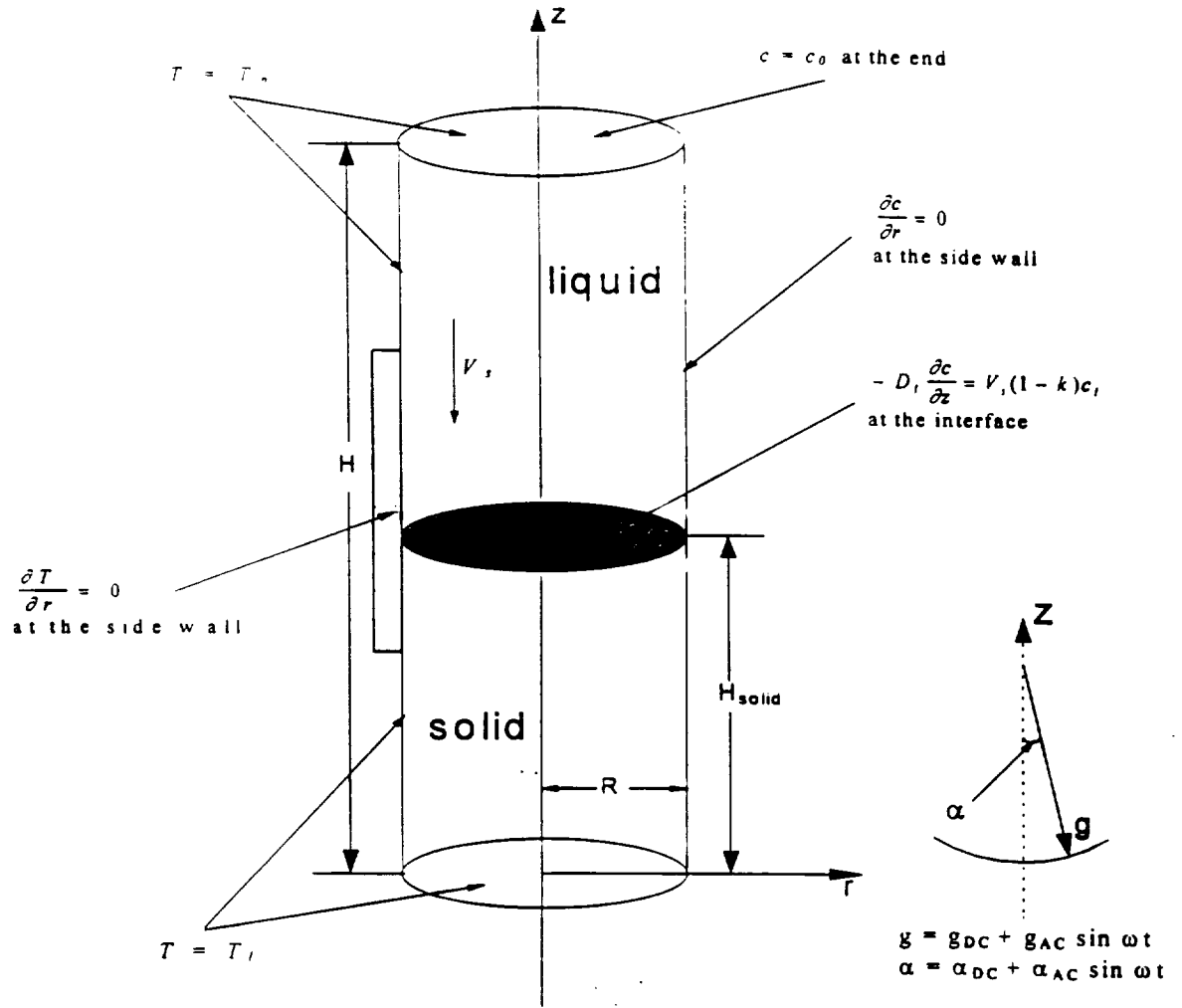


Fig. 1 The schematic of the geometry and thermal and concentration boundary conditions of the calculation.

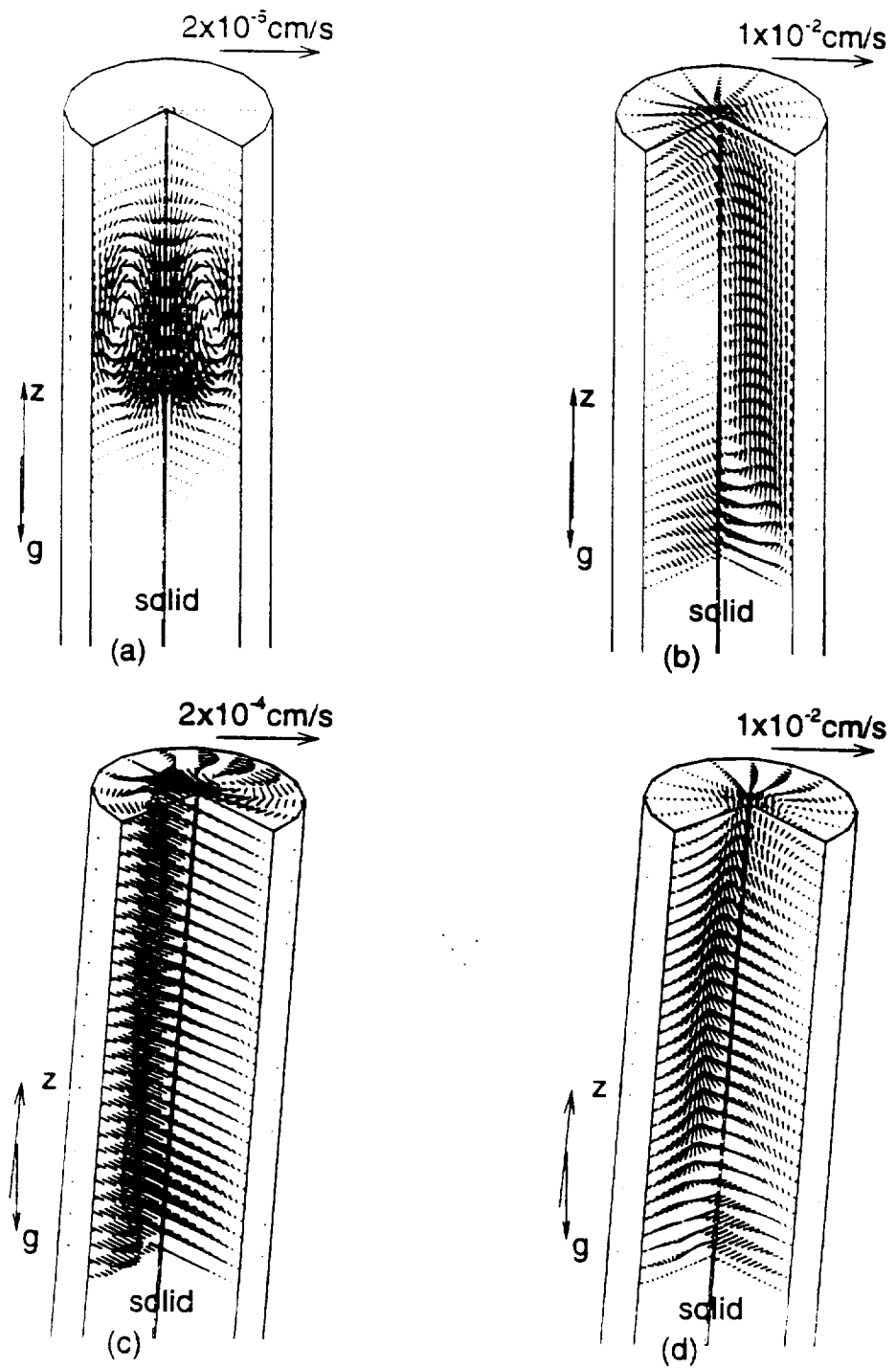


Fig.2. The 3D flow field in the liquid region with constant 'g' and fixed orientation.
 (a) $10^{-5} g_e$, $\alpha = 0^\circ$; (b) $10^{-4} g_e$, $\alpha = 0^\circ$; (c) $10^{-5} g_e$, $\alpha = 5^\circ$; (d) $10^{-4} g_e$, $\alpha = 5^\circ$.

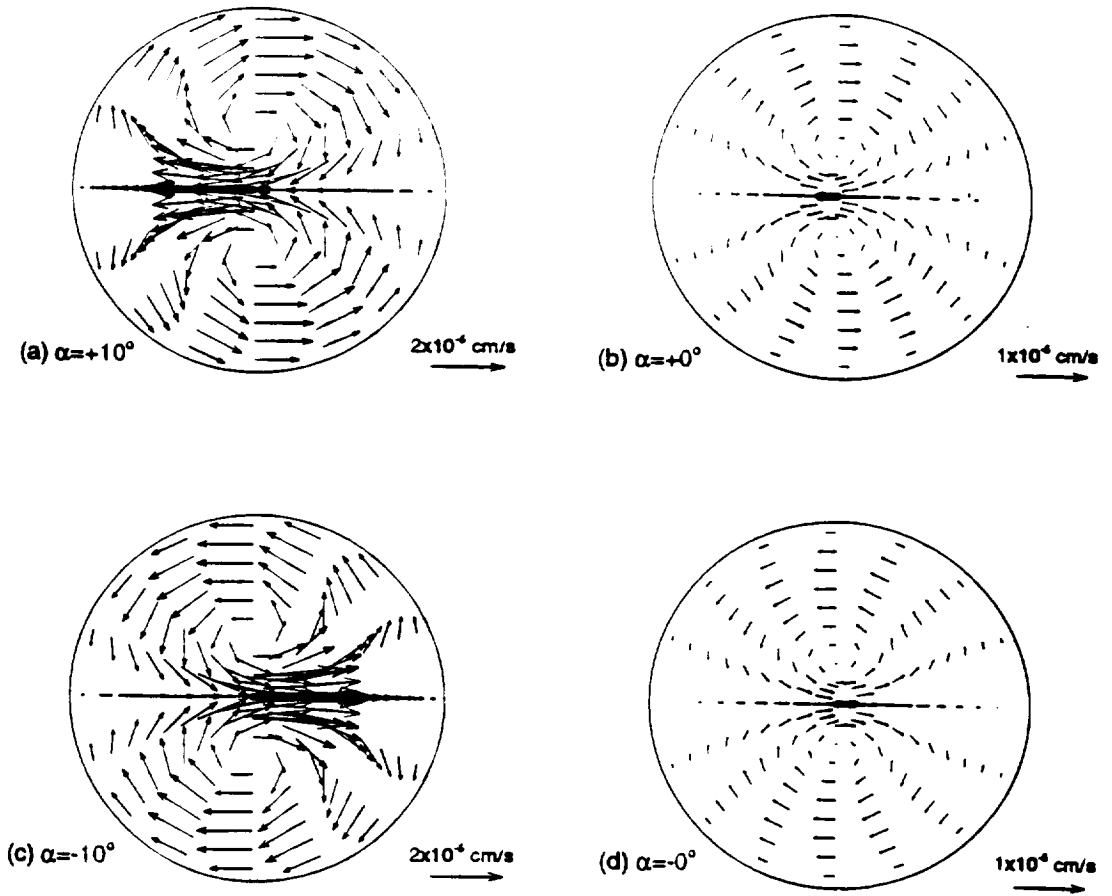


Fig.3. The 2D flow field near the interface under $10^{-5} g_e$. The orientation of the gravity vector is a function of time ($\alpha = 10^\circ \sin \omega t$, $\omega = 2\pi/3600$).



A 3D NUMERICAL MODEL FOR FLOW PROFILES IN A BRIDGMAN TUBE --THE EFFECTS OF CONSTANT AND PERIODIC OFF AXIS ORIENTATION IN A LOW GRAVITY ENVIRONMENT

A. X. Zhao¹, R. Narayanan¹ and A. L. Fripp²

¹Department of Chemical Engineering, University of Florida, Gainesville, FL 32611

²NASA Langley Research Center Hampton, VA 23665

ABSTRACT:

A 3D numerical calculation is performed on a model that depicts the flow profiles due to thermo-solutal convection in a cylindrical tube. The calculations were done with the purpose of delineating the qualitative features of the flow profiles for the cases when the container's axis is perfectly aligned with respect to the mean gravity vector and also when it changes periodically with respect to the gravity vector. It is found that the flow profiles are similar to those of the Rayleigh-Bénard problem in the case of perfect alignment while a swirling pattern appears when the tube's axis is not aligned with the gravity vector. This indicates that it might be preferable to have a slight tilt in the container axis during crystal growth as swirling flow will diminish axial mixing. The solutal convection is the dominant feature of the flow and is affected considerably by the gravity level.

© 1999 COSPAR. Published by Elsevier Science Ltd.

INTRODUCTION

This is a brief report describing the flow profiles that are induced in a low gravity environment in a Bridgman tube in which the fluid occupies a constant volume. The Bridgman tube as considered in this study is merely a circular cylinder that is subjected to radial thermal gradients and axial solutal gradients. Typically, the Bridgman tube is used in the vertical directional solidification of compound semi conductors such as Lead Tin Telluride. The growth of such materials is affected substantially by the convective flow profiles that accompany the process. This convection is due to thermal and solutal gradients that are generated because of the solidification process. Arnold *et al.* (1991) did calculations to model a GaAs space experiment and concluded that three-dimensional flows occur under certain gravitational values and orientations. Their calculations were not concerned with solutal convection. Naumann and Baugher (1992) have made analytical estimates of radial segregation in Bridgman growth for low-level steady and periodic accelerations. In any actual growth process, the liquid zone is ever shrinking and this can be expected to change the flow profiles quite a bit. Nonetheless it would be interesting to have an idea of the flow profiles that are generated when the force conditions on the ampoule are compatible to a time dependent microgravity level and where certain assumptions such as a constant liquid zone is assumed. We present here a numerical model that shows the effects of off axis and a time dependent orientation on the flow profiles in a Bridgman tube. The effect of tilting the otherwise vertical container with respect to gravity is also

described. The calculations were done with the purpose of delineating the *qualitative* features of the flow profiles for the cases when the container's axis is perfectly aligned with respect to the mean gravity vector and also when its axis periodically changes with respect to the gravity vector. The gravitational levels that are assumed range from $10^{-5}g_e$ (or ten micro g) to $10^{-4}g_e$ where g_e is earth's gravity. A value of ten micro g is reasonable as it is a fair representation of the low frequency accelerations experienced on the cargo bay of the U.S. space shuttle or on the future international space station if the Bridgman tube. A level of 100 micro g is not very probable, however we also present calculations that include this extreme case. To the best of our knowledge this is the only study that shows the dominant effect of solutal convection over thermal convection at the higher gravity levels and also the only study where the ampoule axis orientation is varied with time.

Table 1 The Thermophysical Properties Used in the Calculations

Density	7.04 g/cm ³
Kinematic Viscosity	0.0024 cm ² /s
Thermal Diffusivity	0.03 cm ² /s
Solutal Diffusivity	$7 \cdot 10^{-5}$ cm ² /s
Thermal Expansion Coefficient	$1.18 \cdot 10^{-4}$ /C°
Solutal Expansion Coefficient	0.22 /Weight fraction
Segregation Coefficient	0.7

THE MODEL AND THE NUMERICAL SCHEME

The model that is used assumes that the Boussinesq equations hold. Further the calculations were done assuming that the fluid is Lead Tin Telluride reflecting our interest in compound semiconductors. The thermophysical properties of Lead Tin Telluride as used in the calculation are given in Table 1. Figure 1 describes the situation when a container is subject to thermal gradients with a solidifying interface at $z=H-H_{\text{solid}}$. The thermal and concentration boundary conditions imposed on the container are given in Figure 1. No-slip conditions are used at all boundaries including the solid-liquid interface upon which the coordinate system is fixed and which is assumed to move down in the z direction at a constant speed V_s equal to 1 cm/hr. The height of the tube of diameter equal to 1. cm. is given by H and assumed to be 5.0 cm., equally divided between the solid and liquid zones while the insulation zone is assumed to occupy the middle one third. These correspond roughly to the experimental ampoule used in a Lead Tin Telluride experiment that was conducted on USMP 3. The hottest temperature is assumed to be 1150 degrees Celsius while the coldest temperature is fixed to be 700 degrees, the interface being at 900 degrees. The orientation of the gravitational acceleration is expressed in terms of the angle between the gravity and the negative direction of the z-axis. The major assumption is that the liquid length is kept constant. As a result it is assumed that the end of the liquid was at a constant concentration, C_0 equal to 0.2 weight fraction. This is tantamount to a continuous feeding of such liquid at the solidification rate V_s . Before we go on it might be useful to point out that the thermal Rayleigh number is estimated to be about 65 for a gravity level $10^{-4}g_e$ while the solutal Rayleigh using the same length scale is about 147000

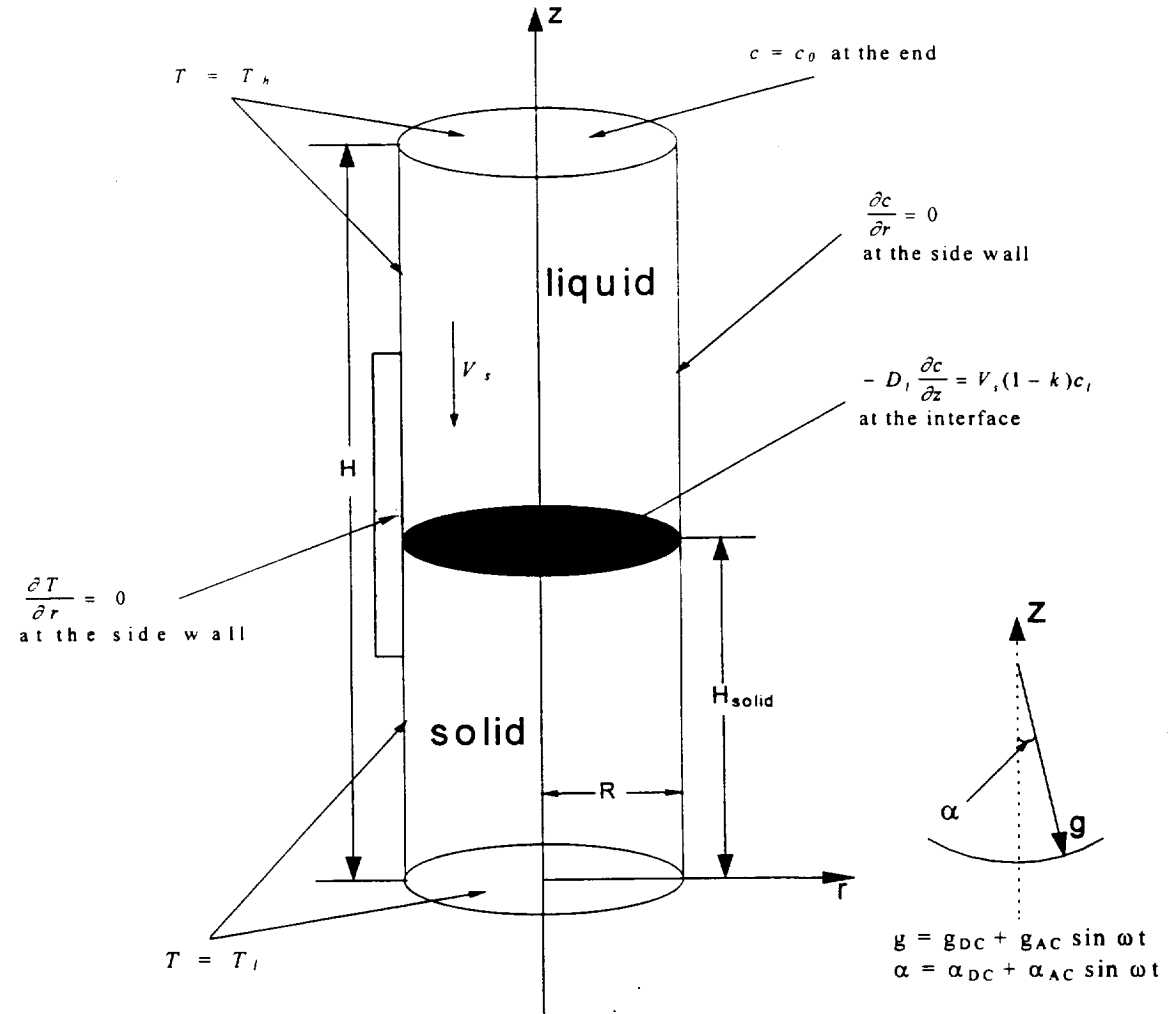


Fig. 1 The schematic of the geometry and thermal and concentration boundary conditions of the calculation.

RESULTS OF THE CALCULATIONS AND CONCLUSIONS

The finite volume method, SIMPLE (cf. Patankar, 1980) was chosen to solve the governing equations. Figure 2 shows the flow profiles at two different gravity levels. Figure 2a describes the pattern that is expected at a constant g level of $10^{-5}g_e$. What is to be observed is vertical stacking of an axisymmetric or torroidal pattern. This vertical stacking may be expected as the top of the ampoule is hotter than the bottom and the lower 'cell' is in the insulation zone. The configuration acts like a fluid that is 'heated from above' and the weak flow is primarily driven by radial gradients. The weakness in the lower cell is primarily due to the effect of the presence of the 'no slip' solid boundary.

The situation changes somewhat for the case of a g level of $10^{-4}g_e$ as seen in Figure 2b, for here the solutal convection begins to play a part. The solutal gradients are unstable in the sense that they promote flow even if the thermal expansion coefficient is negligible. As observed earlier the solutal Rayleigh number is about 147000 whereas the critical solutal Rayleigh number, in the absence of thermal gradients for this aspect ratio

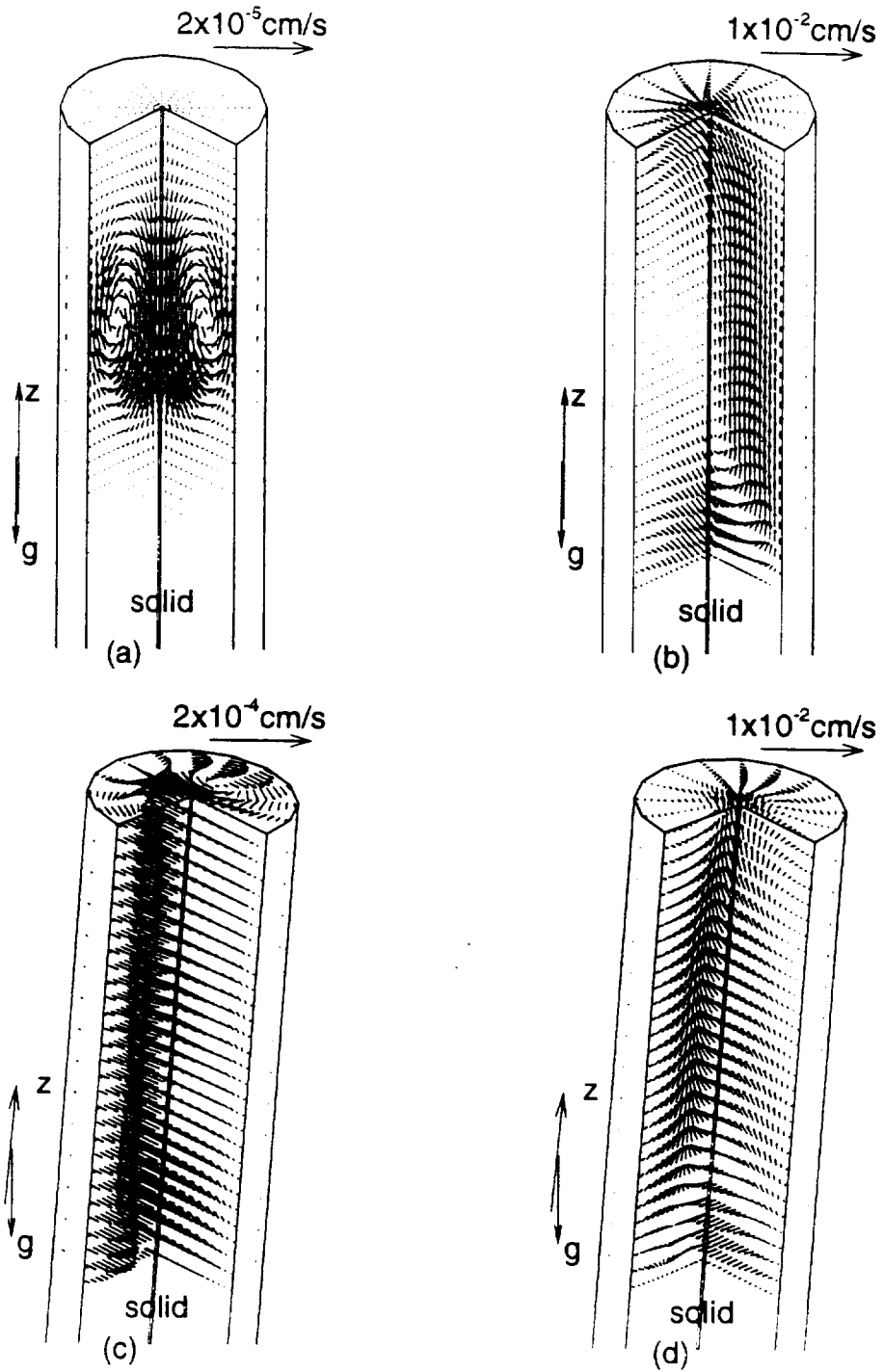


Fig.2. The 3D flow field in the liquid region with constant 'g' and fixed orientation.
 (a) $10^{-5} g_e$, $\alpha = 0^\circ$; (b) $10^{-4} g_e$, $\alpha = 0^\circ$; (c) $10^{-5} g_e$, $\alpha = 5^\circ$; (d) $10^{-4} g_e$, $\alpha = 5^\circ$.

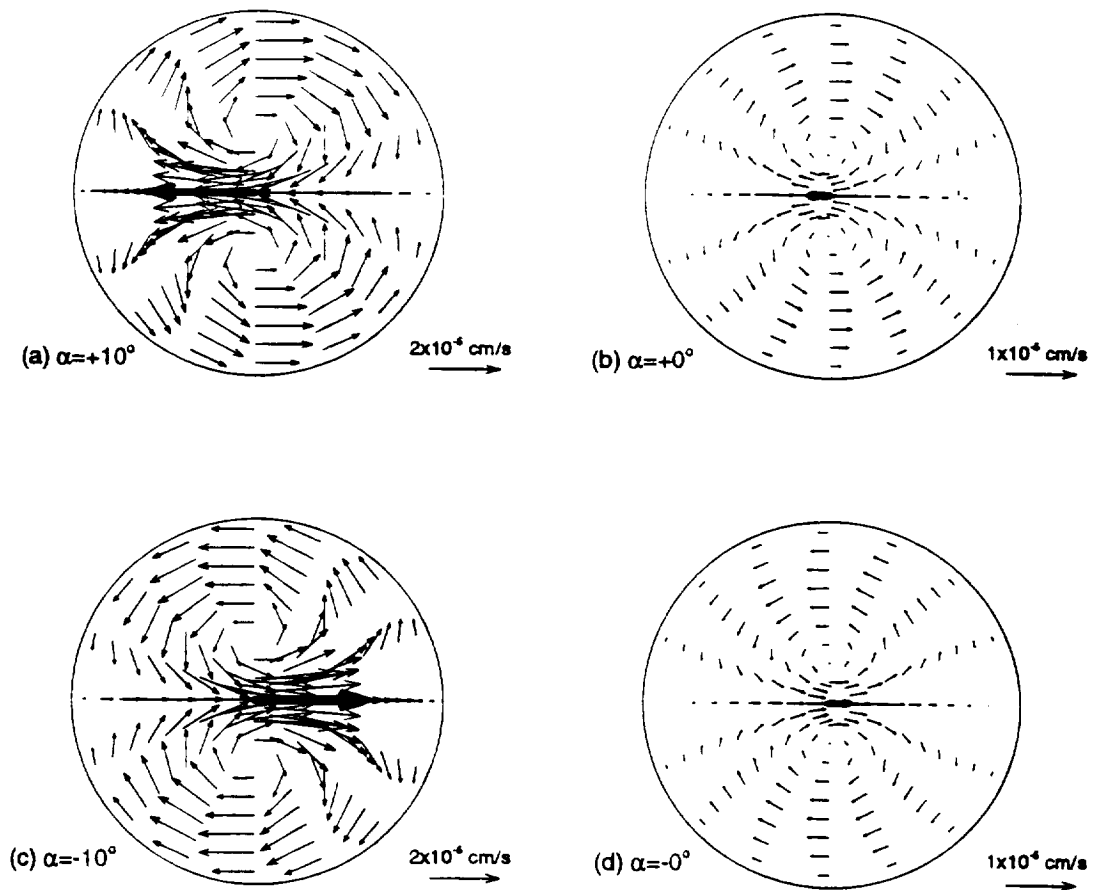


Fig.3. The 2D flow field near the interface under $10^{-5} g_e$. The orientation of the gravity vector is a function of time ($\alpha = 10^\circ \sin \omega t$, $\omega = 2\pi/3600$).

(radius/ height =0.2) turns out to be about 50000 from the calculations of Hardin et. al.. The unicellular patterns that are observed are a result of the solutally driven convection and are expected for this geometry according to the results of the Rayleigh-Bénard problem (cf. Hardin et.al., 1990). Notice further that the vertical stacking arrangement disappeared for the larger 'g' level indicating the dominance of the solutal convection over the thermal convection. Figure 2c shows the flow profiles resulting from a time invariant change of the ampoule axis with respect to the mean gravity vector of $10^{-5}g_c$. What is immediately apparent is the swirling flow that helps contain the rejected solute near the solid liquid interface. The 'z' component of this type of flow is much smaller than the other two components except near the interface and the end of the liquid where all components are set to zero on account of no-slip. It is a concentration induced flow because the velocity components near the interface in Figure 2c are much larger than in Figure 2a. In a real crystal growth configuration such an off axis tilt would help prevent axial mixing and therefore be beneficial to the crystal. If the 'g'- value is increased by an order of magnitude the flow is mostly of a unicellular style except near the interface. This is shown in Figure 2d. Figure 3 depicts the periodic change of the cylinder axis with the gravity vector. The frequency was set to be one cycle per hour. This was an arbitrary choice even though aerodynamic drag causes a readjustment every 20 minutes or so in a typical space orbiter. All the same the results can be expected to be qualitatively similar to those reported here in the case when the frequency is increased three fold. The flow profiles at a constant 'z' plane near the solid liquid interface are given at every quarter cycle, once a periodic steady state is reached. Notice that the direction of the swirl changes every half cycle i.e., when the gravity vector crosses the cylinder axis leading to local mixing near the solid liquid interface.

The effect of gravity level and time periodic off axis alignment show collectively that the convection at low gravity in a bottom or top seeded Bridgman tube is primarily in the solutal driven mode as long as the gravity level is not very small. Moreover a slight tilt with respect to gravity causes the fluid flow to go into a swirling mode so that solute is contained near the solute-generating boundary.

ACKNOWLEDGMENT

We acknowledge NASA for supporting this work under Grant No. NAG-1-1474 and NAG 8 1243 as well as the Florida Space Grant Consortium. The computations were performed on the CRAY/C90 under the NASA National Aerodynamics Simulation (NAS) Program.

REFERENCES

- Arnold, W.A., Jacqmin, D.A., Gaug, R.L., and Chait, A. Three-Dimensional Flow Transport Modes in Directional Solidification During Space Processing, *J. Spacecraft*, 28, pp.238-243 (1991)
- Hardin, G.R., Sani, R.L., Henry, D. & Roux, B.. Buoyancy-Driven Instability in a Vertical Cylinder: Binary Fluids with Soret Effect. Part I: General Theory and Stationary Stability Results, *Int. J. Num Meth. Fluids* 10,79 (1990)
- Naumann R.J., and Baugher, C., Analytical Estimates of Radial Segregation in Bridgman Growth from Low-level Steady and Periodic Accelerations, *J. Crystal Growth*, 121, pp.751-768 (1992)
- Patankar, S.V., Numerical Heat Transfer and Fluid Flow, *Taylor and Francis*, Washington, DC (1980)



ELSEVIER

Journal of Crystal Growth 174 (1997) 90–95

JOURNAL OF **CRYSTAL
GROWTH**

The microgravity environment: its prediction, measurement, and importance to materials processing

B.P. Matisak^{a,*}, A.X. Zhao^b, R. Narayanan^b, A.L. Fripp^c

^a Teledyne Brown Engineering, Huntsville, Alabama 35807, USA

^b University of Florida, Gainesville, Florida 32611, USA

^c NASA Langley Research Center, Hampton, Virginia 23681, USA

Abstract

One of the primary benefits of conducting scientific research in space is to take advantage of the low acceleration environment. For experimenters conducting space research in the field of materials science the quality of the science return is contingent upon the extremely low frequency acceleration environment ($\ll 1$ Hz) aboard the spacecraft. Primary contributors to this low frequency acceleration environment (commonly referred to as the steady-state acceleration environment) include aerodynamic drag, gravity-gradient, and rotational effects. The space shuttle was used on the STS-75 mission as a microgravity platform for conducting a material science experiment in which a lead tin telluride alloy was melted and regrown in the Advanced Automated Directional Solidification Furnace under different steady-state acceleration environment conditions by placing the shuttle in particular fixed orientations during sample processing. The two different shuttle orientations employed during sample processing were a bay to Earth, tail into the velocity vector shuttle orientation and a tail to Earth, belly into the velocity vector shuttle orientation. Scientists have shown, through modeling techniques, the effects of various residual acceleration vector orientations to the micro-buoyant flows during the growth of compound semiconductors. The signatures imposed by these temporally dependent flows are manifested in the axial and radial segregation or composition along the crystal.

1. Introduction

1.1. Motivation for conducting specific materials science experiments in space

Crystal growth research in ground-based laboratories is complicated by the ever present effects of gravity acting on the sample during processing.

Such an effect oftentimes drives natural convection within the sample. In theory, if these same types of experiments are conducted in a microgravity environment, buoyancy-driven convection effects due to gravity are essentially eliminated, thus providing ideal conditions for diffusive growth within the sample. Under a microgravity environment scientists are able to study the low frequency, low acceleration (referred to as the steady-state acceleration regime) effects (if any) on materials. Furthermore, scientists can use a space platform to determine whether the particular direction of the steady-state

* Corresponding author.

acceleration (SSA) vector present at the growth location influences the quality of the space-processed crystal. Results from these types of experiments will allow scientists to validate or update their models and theories in the field of crystal growth research. Such discoveries are expected to improve ground-based processing techniques for crystal processing [1–3].

2. Lead tin telluride grown in space

2.1. Description

The lead tin telluride (PbSnTe) alloy was selected as an experiment within the Advanced Automated Directional Solidification Furnace (AADSDF) to fly aboard the Space Shuttle Columbia as part of the Third United States Microgravity Payload (USMP-3) mission (STS-75) in February and March of 1996. The material was selected as an experiment for investigation under microgravity conditions due to the fact that it can be used to produce infra-red detectors and lasers on Earth. The primary objective of the experiment was to determine the effects (if any) of the SSA environment during the processing of each of the PbSnTe samples. Understanding the microscopic effects during processing in a low-g environment could improve the way these devices are made [4].

2.2. Specific experimental studies of PbSnTe

Even at acceleration levels as small as $5 \times 10^{-6}g$, scientists interested in studying PbSnTe have devised theories on how the crystal microstructure will react to the small but constant accelerations present at the sample location [3]. Contributors to the SSA environment will be discussed later in the paper.

Two possible crystal growth orientations with respect to the SSA (gravity) vector will be addressed. Figs. 1 and 2 summarize these two possible orientations. Fig. 1 is described as the “hot on top” configuration; that is, the SSA vector travels in the direction from the hot temperature portion of the sample to the cooler temperature portion of the

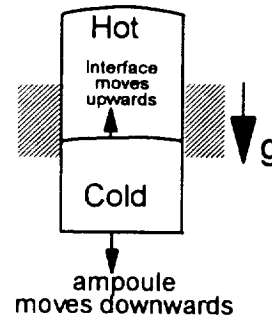


Fig. 1. Hot to cold configuration.

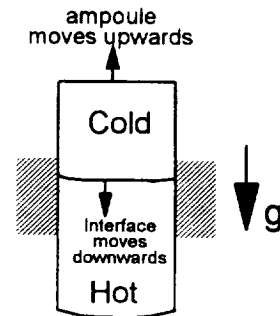


Fig. 2. Cold to hot configuration.

sample. Fig. 2 depicts the “hot on bottom” configuration, where the SSA vector travels in a direction from the cold end to the hot end of the sample.

To understand which orientation is preferred one must first look at the phase diagram [5] of the PbSnTe alloy (Fig. 3). The phase diagram summarizes the equilibrium relationship between the temperature and concentration values of the alloy. From Fig. 4a and Fig. 4b, assume that point “a” defines the alloy at the molten state (that is, beginning with a uniform mixture and the sample has been melted back to the seed). If one then cools the alloy to point “b”, in the two phase region, it will separate into two parts – a solid phase which contains a lower concentration of SnTe and a liquid part which is more concentrated in SnTe. This, in fact, is what is meant by “SnTe is rejected into the liquid.” Further cooling (point “c”) results in an even higher concentration of SnTe rejected into the

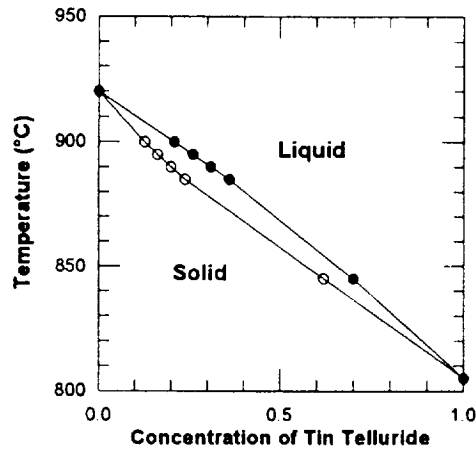
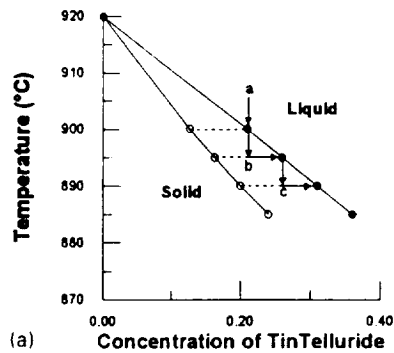
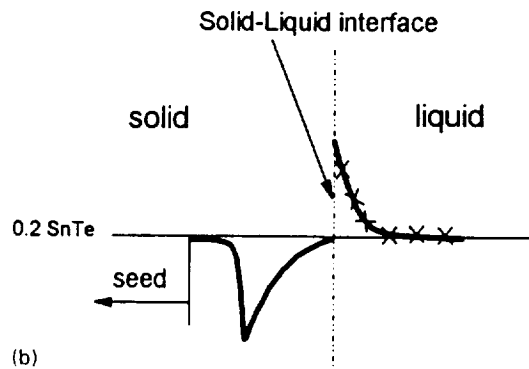


Fig. 3. Phase diagram of PbSnTe [5].



(a)



(b)

Fig. 4. (a) Phase diagram showing the operating lines. (b) Concentration profile of PbSnTe in the solid and liquid.

liquid. In practice, the liquid concentration at the solid–liquid interface will increase continuously and smoothly along the liquidus line and the cooling does not take place stepwise. It is shown in

Fig. 4a as such only for the sake of dramatizing an explanation.

This rich concentration of SnTe just to the right of the solid–liquid interface is dramatically different than the composition of the specie at the far right portion of the liquid. The composition of the hotter liquid is predominantly PbTe. PbTe is more dense than the SnTe that is near the solid–liquid interface. However, the interface is cooler than the bulk liquid and it may be noted that the density decreases with temperature [6]. Therefore, this poses an interesting question and introduces the primary scientific objective for this AADSF experiment. Depending on the orientation of the SSA vector, which configuration is more stable for this particular class of material? The configuration from Fig. 1 depicts a solutally unstable (more dense specie, PbTe, on top of sample), thermally stable (cooler specie, SnTe, on bottom) configuration. The configuration from Fig. 2 depicts a solutally stable (more dense specie, PbTe, on bottom of sample), thermally unstable (cooler specie, SnTe, on top) configuration. Conducting this experiment in the microgravity environment of space will allow scientists to answer this scientific query.

2.3. Orbital dynamics experiment requirements

In order to successfully test the scientific questions of this experiment it is paramount that the SSA vector for both cases be as close as possible to being parallel to the growth axis for each sample. Recall that the vector for the first case travels in a direction from the hot end to the cold region of the AADSF (Fig. 1) and the vector for the second case travels from the cold end to the hot end (Fig. 2). Three primary factors contribute to the steady-state acceleration environment at any location away from the spacecraft center of gravity (c.g.): drag, gravity-gradient, and rotational effects [7]. Drag effects are a function of spacecraft altitude, attitude, and the time in the 11-year solar cycle that the mission takes place (atmospheric density influence). Gravity-gradient effects are primarily a function of the distance away from the shuttle center of gravity (c.g.) and the shuttle attitude. Rotational effects are comprised of radial contributions (a function of shuttle angular velocity

components, ω , and the distance away from the shuttle c.g.) and tangential contributions (a function of shuttle angular acceleration components, α , and the distance away from the shuttle c.g.). Meticulous orbital dynamics studies using the Simulation and Analysis of Multi-Spacecraft On-Orbit (SAMSON) 6-Degree of Freedom (6-DOF) model [8], developed by engineers from Teledyne Brown Engineering at Marshall Space Flight Center (MSFC), were conducted prior to the flight to align the SSA vectors as parallel as possible to the long axis of the respective samples (hot to cold, cold to hot configurations). Due to the location of the AADSF relative to the shuttle c.g., it became evident from the studies that it was not possible to provide perfectly aligned SSA vectors relative to the long axis of the samples. A particular nomenclature was used in defining how well these vectors were aligned with the long axis of the sample. This nomenclature was based on the ratio of the acceleration component along the long axis of the sample, or the “axial” component, to the acceleration component acting perpendicular to the direction of growth, or the “normal” component. The objective for both experimental cases was to obtain as high as possible axial/normal ratio conditions during sample processing.

2.4. Pre-flight and realtime SSA vector results at the AADSF sample location

Orbital dynamics studies of the shuttle were completed to determine the attitudes that provided optimum axial/normal SSA ratios for the AADSF scientific objectives [9]. These shuttle attitudes, along with the predicted axial/normal ratios for the two experiment runs, are provided in Figs. 5–8 respectively. The resulting AADSF attitudes were forwarded to the flight operations teams at both MSFC and the Johnson Space Center (JSC) to incorporate during realtime AADSF science operations.

The Microgravity Analysis Work Station (MAWS) team, represented by flight control engineers with extensive orbital dynamics experience, were located alongside the AADSF science team in the Payload Operation Control Center (POCC) at

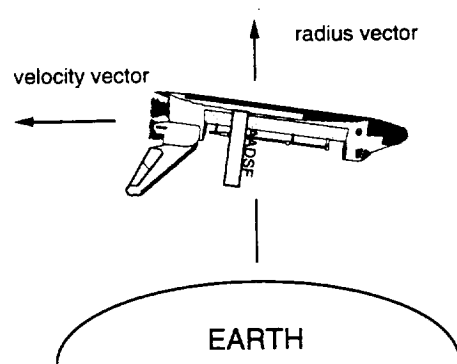


Fig. 5. AADSF hot to cold attitude configuration.

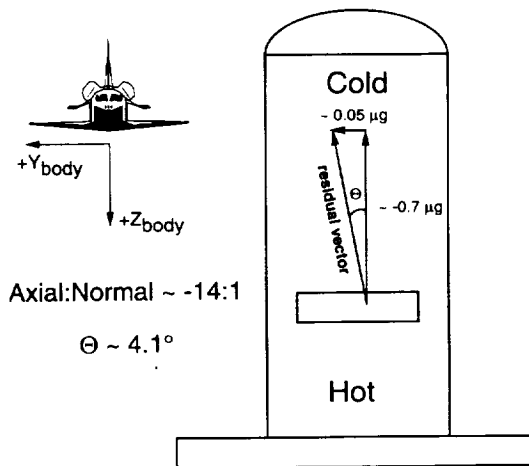


Fig. 6. Pre-flight modeled SSA vector at AADSF, hot to cold configuration.

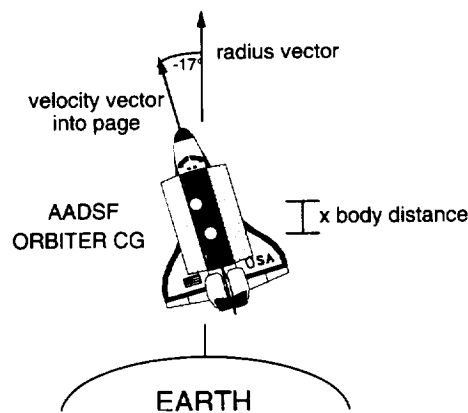


Fig. 7. AADSF cold to hot attitude configuration.

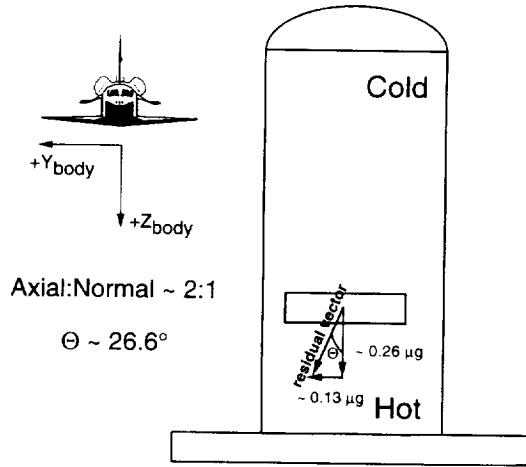


Fig. 8. Pre-flight modeled SSA vector at AADSF, cold to hot configuration.

MSFC. The MAWS team was responsible for monitoring and evaluating the integrity of the SSA environment at the AADSF location during sample processing. The MAWS team was also responsible during the flight for obtaining updated shuttle and atmospheric density parameters and, if necessary, make attitude modifications based on realtime SAMSON 6-DOF simulation runs. Based on real-

time conditions, the MAWS team recommended a modification to the first attitude to reduce undesirable gravity-gradient effects acting normal to the growth axis of the sample. No modifications were made to the second AADSF attitude. Figs. 9 and 10 provide a snapshot of the realtime MAWS result of the SSA environment (as defined in axial/normal SSA ratio terms) during realtime sample processing of both crystals. From the realtime data in Figs. 9 and 10 one can see that it is possible to analytically map the residual acceleration environment on a vehicle platform in Low Earth orbit (LEO) in support of g-sensitive material science experiments. Realtime MAWS results from Figs. 9 and 10 show good correlation with the SAMSON 6-DOF analytical solutions from Figs. 6 and 8. From Figs. 9 and 10 one can observe a few characteristics in the data. For example, observed spikes represent the effects of Vernier Reaction Control System (VRCS) jet firings that were required to maintain the correct shuttle orientation during AADSF sample processing. Straight slopes without spikes represent loss of signal (LOS) periods where the shuttle is temporarily out of communication with the ground. It is interesting to note from Fig. 9 the period around 196 h MET where the axial/normal SSA ratio at AADSF decreased significantly. This event was due to the fact that over that time period

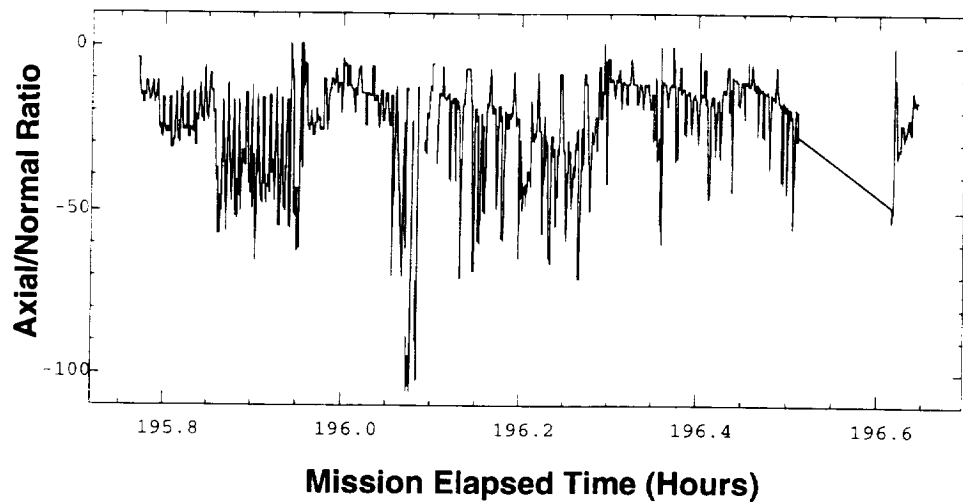


Fig. 9. Realtime snapshot of MAWS results, hot to cold attitude configuration.

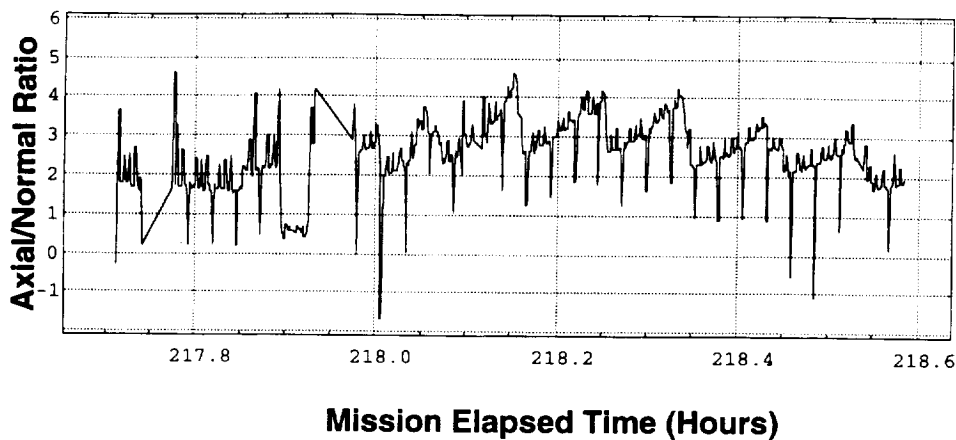


Fig. 10. Realtime snapshot of MAWS results, cold to hot attitude configuration.

the attitude control of the shuttle was temporarily turned off as a result of thermal problems in the VRCS system. The thermal problem was quickly resolved and attitude control was reacquired. Nevertheless, from this event one observes the sensitivity of the SSA environment as a function of shuttle orientation.

3. Conclusion

With the successful completion of these two AADSF PbSnTe science experiments during the USMP-3 mission, the experiment team is currently analyzing the space-processed samples and final results will not be completed for many months. As a result it will not be known for a while whether the questions regarding specific crystal growth processes will be answered. It is only through the opportunity of space flight that scientists can conduct experiments under the influence of microgravity conditions to better understand crystal growth processes that could not otherwise have been obtained in ground-based laboratories. Similar types of microgravity experiments will be conducted on future shuttle and Space Station flights with the goal of further understanding crystal processes.

Acknowledgements

The authors wish to gratefully acknowledge the support by the National Aeronautics and Space Administration (NASA) for this work through the NAS8-41000 contract (BPM) and the NASA Grant NAG-1-1474 (AXZ and RN).

References

- [1] W.A. Arnold, D.A. Jacquim, R.L. Gaug and A. Chait, *J. Spacecraft* 28 (1991) 238.
- [2] R.J. Naumann and C. Baugher, *J. Crystal Growth* 121 (1992) 751.
- [3] A.X. Zhao, G. Guo, R. Narayanan and A.L. Fripp, *AIAA* 96-0254 (1996).
- [4] E. Nelson, *NASA Technical Memorandum* 103775 (1991).
- [5] A.R. Calawa, T.C. Harman, M. Finn and P. Youtz, *Met. Soc. AIME* 242 (1968) 374.
- [6] V.M. Glazov, S.N. Chizhevskaya and N.N. Glagoleva, *Liquid Semiconductors* (Plenum, New York, 1969).
- [7] B.P. Matisak, M.J.B. Rogers and J.I.D. Alexander, *AIAA* 94-0434 (1994).
- [8] B.P. Matisak, *AIAA* 95-4077 (1995).
- [9] B.P. Matisak, Presentation to NASA HQ/MSFC Management on the Residual Acceleration Environment for AADSF on STS-75, January (1996).



A NUMERICAL MODEL THAT SHOWS THE EFFECT OF GRAVITY DRIVEN CONVECTION ON MEASUREMENTS OF MASS DIFFUSIVITY

C. Mallika¹, A. X. Zhao², R. Narayanan² and T.J. Anderson²

¹*Metallurgy Division, Indira Gandhi Centre for Atomic Research, Kalpakkam 603102, India*

²*Department of Chemical Engineering, University of Florida, Gainesville, Florida 32611.*

ABSTRACT

The results of a numerical study that models the three dimensional flow of solutal convection in a cylindrical geometry is presented. The model was developed to estimate the convective flows that accompany the experimental measurement of molecular diffusivity of oxygen ions in liquid metals by the method of electrochemical titration. The model predicts convective flows under certain conditions. The predictions are in qualitative agreement with the experimental results that show an enhancement in the effective diffusivity.

© 1999 COSPAR. Published by Elsevier Science Ltd.

INTRODUCTION

This paper is concerned with the numerical modeling of the transport effects during the measurement of oxygen diffusivity in liquid metals and the qualitative comparison of the model with experiments. Several investigators using electrochemical titrations have measured the diffusivity of oxygen in various liquid metals and the procedures are well discussed. (Tare, 1980). The objective of the present investigation is to obtain a qualitative picture of the dominant convective processes by employing a three dimensional numerical model and also to compare the qualitative results of this model with careful experiments done by Sears et al. (1993) and reconfirmed by the first author of this paper.

Experiments for diffusivity measurements involve the establishing of an oxygen concentration gradient. Calculations that simulate transient and steady state experiments are therefore given for the cases when the oxygen is depleted from the liquid metal sample in two different modes- a bottom depletion mode and a top depletion one. In each mode the liquid metal sample is assumed to be nearly vertical. In the bottom depletion mode the concentration of oxygen at the bottom of the sample is very small and oxygen is depleted from that boundary. Therefore the fluid is gravitationally stable in the bottom depletion mode. For this case, calculations indicate the existence of stable density gradients whereas in the top depletion mode the reverse is true and solutal convection is predicted depending on the experimental conditions. The distribution of the oxygen concentration and the flow patterns that were obtained from the simulation studies indicate that the measured diffusivity can be easily corrupted by solutal convection. This observation is corroborated by experimental results. The experimental diffusivity measurements were strongly affected by convective effects in those top depletion experiments that had a higher initial oxygen concentration. However, the

unsteady state top depletion mode was preferred when the initial oxygen levels were low and the numerical model also confirms this. As evidenced from the modeling, the strength of convection observed in a steady state top heavy arrangement was much larger than the bottom heavy configuration. The results of both experiments as well as modeling indicate that solutal convection is greatly enhanced depending on the experimental conditions. The parameters, which affect the results, are the mode of operation, initial oxygen concentration, tilts and heat leakages.

THE MODEL

Figure 1 is a schematic of the problem that was modeled numerically to obtain three dimensional flow fields. The model that was used assumed that the Boussinesq equations hold. The concentration conditions imposed on the container depended on the mode and place of oxygen removal. These are shown in Figure 1. The calculations were done assuming that the fluid is incompressible and Newtonian. The thermophysical properties of tin used in the calculations are well established and are given in the sources cited by Sears *et al.* (1990). Kao (1993) estimated the solutal expansion coefficient for oxygen in tin as 0.865 /mole fraction, by using a dilute solution assumption and a simple mixing rule. The value of diffusivity used in the calculations that predict the flow was obtained from Sears. *et al.* and was assumed to be $5.7 \times 10^{-9} \text{ m}^2/\text{s}$. No-slip conditions were used at all boundaries. The governing equations, in the general vector form, for the calculations are:

$$\nabla \cdot \vec{V} = 0 \quad (1)$$

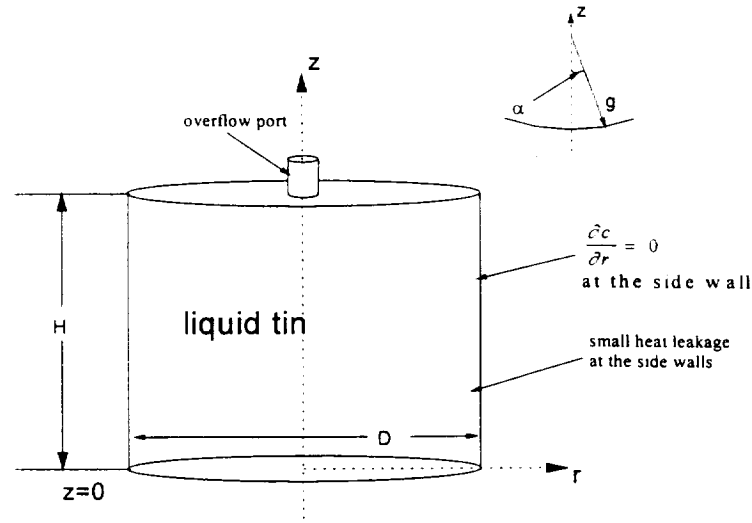
$$\frac{\partial \vec{V}}{\partial t} + \vec{V} \cdot \nabla \vec{V} = -\frac{1}{\rho} \nabla P + \nu \nabla^2 \vec{V} + g[\beta_T(T - T_0) + \beta_c(C - C_0)]\vec{e}_z \quad (2)$$

$$\frac{\partial T}{\partial t} + \vec{V} \cdot \nabla T = \nabla \cdot \left(\frac{k}{\rho C_p} \nabla T \right) \quad (3)$$

$$\frac{\partial C}{\partial t} + \vec{V} \cdot \nabla C = D \nabla^2 C \quad (4)$$

where \vec{V} , P , T and C are the velocity, pressure temperature and concentration fields. The subscript '0' means a reference state such as the initial state. ν , k , ρ , C_p and D are the kinematic viscosity, thermal conductivity, density, specific heat and mass diffusivity respectively while β_T and β_c are the thermal and solutal expansion coefficients.

The equations were solved numerically using a SIMPLE algorithm, a method developed by Patankar (1980). The diameter of the cylindrical cell was assumed to be 0.73 cm as this was the dimension of the cell used in the experiments of Sears *et al.* and in the present study. The heights of the cell used in the calculation varied according to the different cases studied and are reported in Table 1.



Bottom Depletion:

$$c \Big|_{z=0} = 0$$

$$\frac{\partial c}{\partial z} \Big|_{z=H} = 0$$

Top Depletion:

$$\frac{\partial c}{\partial z} \Big|_{z=0} = 0$$

$$c \Big|_{z=H} = 0$$

Fig. 1. Schematic representation of the cell used in the numerical calculations.

RESULTS AND DISCUSSION

As the emphasis in this study was an understanding of the qualitative features of the numerical simulations of the physical experiment, these features are discussed along with the experimental results. Figure 2 represents the unsteady convection that arises in the top and bottom depletion modes during the electrochemical titrations. Note that in both modes of oxygen depletion the container is assumed to be slightly tilted (z -axis was 2° from the vertical line) with respect to gravity. This is within reason for it is impossible to restrict the container's orientation within 2° in the actual experiments. Also a heat leakage of 2 degrees is assumed to exist at the sidewalls. At first sight it would appear that the bottom depletion mode ought to be solutally stable, as the arrangement is bottom heavy with respect to density gradients. However, convection can always be expected on account of the small tilt. Even though the tilt is extremely small, it is not negligible causing the concentration gradient to become oblique with respect to the gravity vector and generating convection immediately. The top depletion mode on the other hand is conditionally unstable even if the container geometry were vertical as the fluid is in a top-heavy arrangement and the tendency to give rise to convection is a function of the height of the sample and the initial concentration of oxygen in the tin. In fact it may be noted from Figure 2 that the convective flows are strong in the top depletion case. The fact that the oxygen is quickly depleted in the top depletion mode is also very apparent and this causes an apparent increase in the diffusivity values. This is also seen in the experimental results given in Table 1. The effect of initial concentration is seen in the comparison of Figure 2 with Figure 3. The essential difference between these two figures is the initial concentration at the start of the titration procedure. There is however a difference in the liquid aspect ratios between Figures 2 and 3. The liquid depths and initial conditions as well as mean temperatures that were assumed in order to obtain Figures 2 through 4 correspond to the experimental values given in Table 1 while the diameter was assumed to be 0.73 cm. The different liquid

aspect ratios are of little consequence as the diffusion boundary layer length is comparable in both calculations. The diffusion boundary layer changes with slowly time and as the effective aspect ratio is determined by the diffusion boundary layer, it can be considered constant for all practical purposes. To understand how initial concentration plays a role, we recall the unsteady Rayleigh- Bénard problem. We then observe that under the top depletion scenario a large initial concentration results in a steep unstable density gradient and this gives way to an ever more top-heavy arrangement. Here the large concentration gradient only makes matters worse and promotes convection ultimately corrupting the diffusivity measurements. On the other hand when we consider the bottom depletion case we observe that the concentration gradient corresponds to a bottom heavy arrangement and that a steeper concentration gradient simply makes the system even more stable.

Table 1. Experimental Conditions and Results for the Diffusivity of Oxygen in Liquid Tin

Titration mode		Height of tin (cm)	Temperature (K)	Initial oxygen mole fraction	Diff. Coefficient (m ² /s)
Transient ^a	Bottom	0.389	994	2.4 x 10 ⁻⁴	7.57 x 10 ⁻⁹
	Top	0.389	994	2.4 x 10 ⁻⁴	2.26 x 10 ⁻⁸
Transient	Bottom	0.520	845	7.7 x 10 ⁻⁶	3.43 x 10 ⁻⁹
	Top	0.520	845	7.7 x 10 ⁻⁶	4.63 x 10 ⁻⁹
Steady state	Bottom heavy	0.579	971	^b 6.3 x 10 ⁻⁵	3.05 x 10 ⁻⁸
	top heavy	0.579	971	^c 6.3 x 10 ⁻⁵	4.98 x 10 ⁻⁸

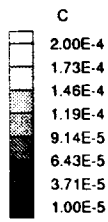
^a Results reported by Sears *et al.* (1993)

^b The oxygen concentration at the top, ^c The oxygen concentration at the bottom

From the above it is concluded that large initial concentrations of oxygen in the liquid metal favor a bottom depletion titration method while for small initial concentrations a top depletion mode can be stable. Figure 1 shows that the convection is weak in the top depletion mode because the initial concentration is lower here than in Figure 2. Neither figure shows the concentrations at the depleting surface, which may be assumed for all practical purposes, to be zero mole fraction. The simulations of the steady state transport as shown in Figure 4 depict the convection to be greater here than in the top depletion mode of unsteady transport. This happens because the characteristic length in this model is the whole sample height whereas in the transient mode it is the thickness of the concentration boundary layer, which in turn is a function of time. Note that the Rayleigh number, a dimensionless group that arises from the scaling of such problems and one which is indicative of the strength of the convection is proportional to the cube of the characteristic length scale (cf Narayanan, 1984). It may be noted that the solutal Rayleigh number for the top-heavy system is estimated to be 13859 whereas the calculated value for the bottom heavy configuration is -22595. Hence the strength of convection is expected to be more in the top-heavy arrangement which is in accordance with the observation. However a slight tilt with the steady state mode is far worse than a similar tilt on the unsteady mode because

variable in both aspect ratio is purposes. To problem. We then unstable density concentration gradient measurements. On concentration gradient apply makes the

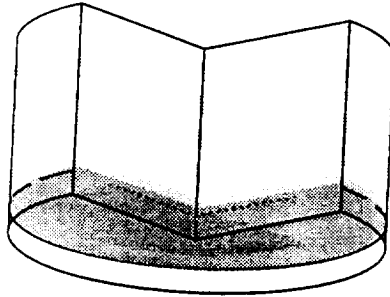
fluid Tin



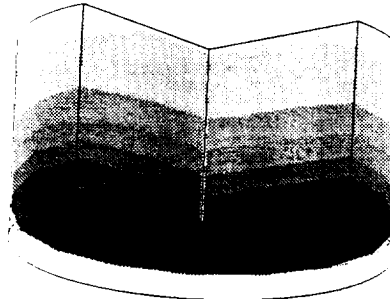
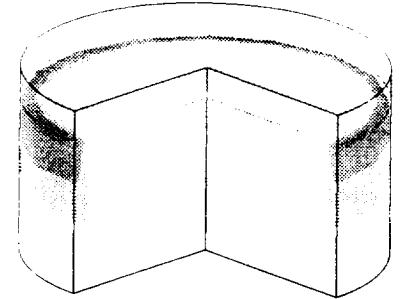
0.05cm/s →

bottom-depletion

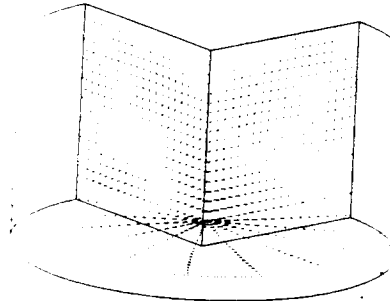
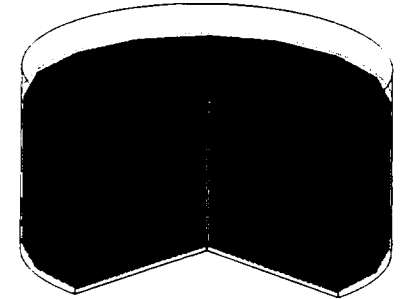
top-depletion



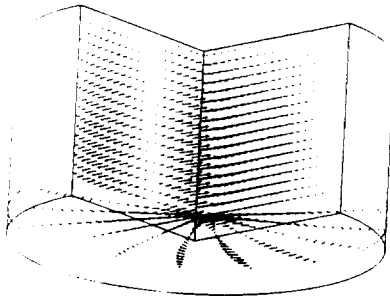
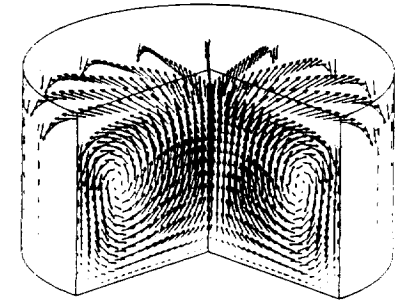
t= 50s



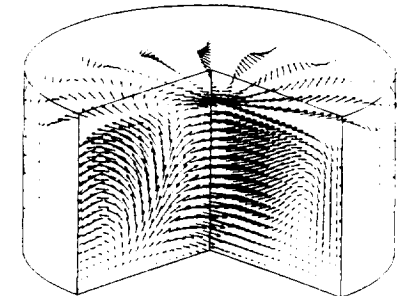
t= 600s



t=50s



t=600s



favor a bottom stable. Figure 3 on is lower here may be assumed, port as shown in transport. This in the transient me. Note that the and one which is length scale (cf. n is estimated to e the strength of the observation. ly mode because

Fig. 2. Comparison of concentration distribution and flow patterns at higher initial oxygen concentration

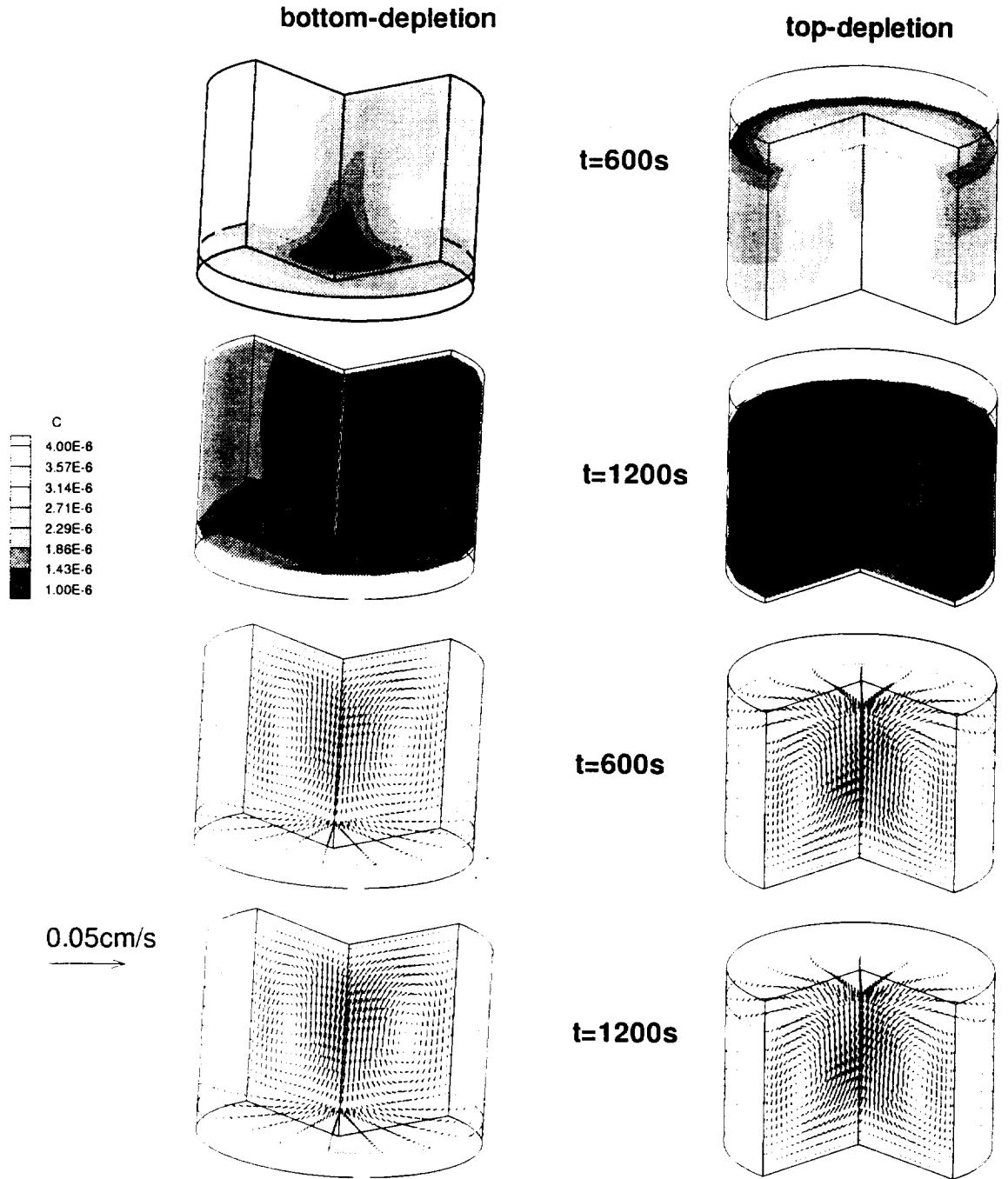
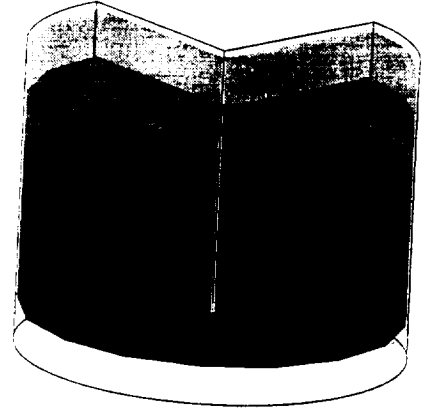
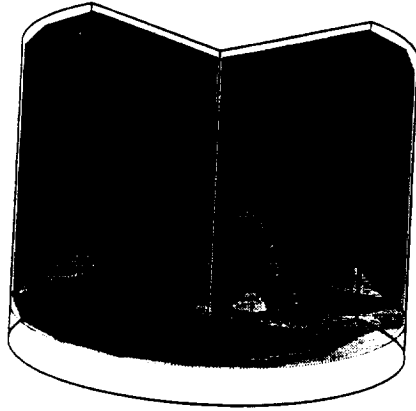
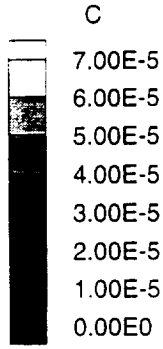


Fig. 3. Comparison of concentration distribution and flow patterns at lower initial oxygen concentration

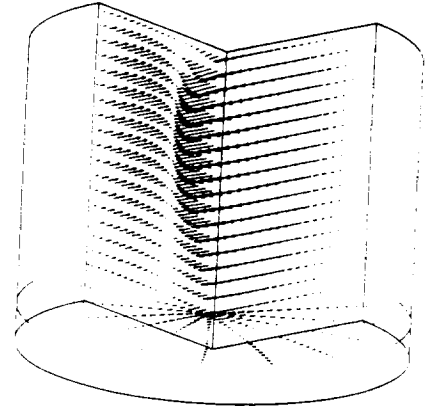
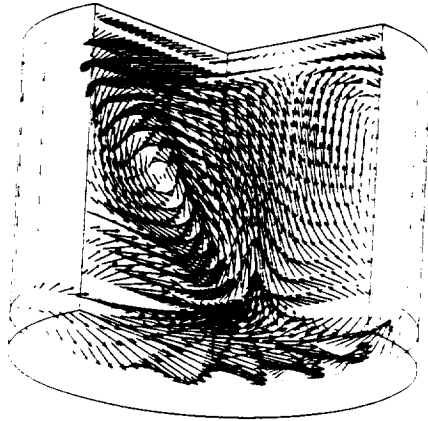
on

top heavy

bottom heavy



0.01cm/s
→



centration

Fig.4. Comparison of concentration distribution and flow patterns between top heavy and bottom heavy configurations in steady studies

the characteristic length scales are so different and the steady state convection that results because of imperfections due to tilts etc. corrupt the diffusivity measurements more severely.

We conclude that electrochemical titration procedures for diffusivity measurements must be interpreted very carefully for the titration mode affects the measured diffusivities in varying degrees. The convective flows that occur are influenced by tilts, heat leakages, initial concentration of oxygen and modes of operation be they steady or transient.

ACKNOWLEDGMENT

We gratefully acknowledge NASA for support through grants NAG 8-1243 and NAG 1-1474

REFERENCES

- Kao, K.Y., *Electrochemical measurements of natural convection in vertical Bridgman configurations*, M.S. Thesis, University of Florida, Gainesville, Florida, (1993).
- Narayanan, R., "Some Differential Inequalities for Thermohaline Convection in Containers of Arbitrary Shape", *International Journal of Engineering Science*, 22, pp. 927-938. (1984)
- Patankar, S., *Numerical Heat Transfer and Fluid Flow*, Taylor and Francis, (1980)
- Sears, B., Anderson, T.J., Narayanan, R., and Fripp, A.L. The detection of solutal convection during electrochemical measurement of the oxygen diffusivity in liquid tin, *Met. Trans.* 24B, pp.91-100, (1993)
- Tare, V. B., Ramana Rao, A.V., and Ramanarayanan, T. A., *Solid Electrolytes and Their Applications* (Edited by E.C. Subbarao), Chapter 5. Plenum, New York. (1980)



AIAA 96 - 0738

**Onset of 3 - D Rayleigh - Marangoni Convection in a
Bounded Circular Cylinder**

**A. A. Zaman and R. Narayanan
Department of Chemical Engineering
University of Florida
Gainesville, FL 32603**

**34th Aerospace Sciences
Meeting & Exhibit
January 15-18, 1996 / Reno, NV**

Onset of 3 - D Rayleigh - Marangoni Convection in a Bounded Circular Cylinder¹

Abbas A. Zaman and Ranga Narayanan²

Department of Chemical Engineering

University of Florida

Gainesville, FL 32611

Abstract

In this study, pattern formation at the bifurcation point from the quiescent state for free surface convection in circular containers is determined. A linearized instability calculation that employs three-dimensional disturbances in the presence of physically realistic side wall boundary conditions is made. The results of the present study will provide a very useful asymptotic limit for nonlinear numerical computations. Under restrictive conditions the current calculations check favorably with those of earlier workers. The results of these studies are shown to be compatible with the experiments of Koschmieder and Prahl.

Introduction:

The onset of flow from a quiescent state, when a layer of fluid is heated from below with an upper free surface, is one of the classical problems of fluid mechanical instabilities (1) and also the subject of many investigations. In this problem, a layer of fluid with an upper free surface is subjected to a temperature gradient that is perpendicular to the interface and one of the goals is to find the critical conditions and the associated pattern for the onset of flow from an erstwhile quiescent state. Curiously, there is a dearth of good experiments on this problem and most of these have been conducted in geometries of large lateral extent while the theories that model these experiments assume the absence of vertical side walls. When a free surface is absent, convection is driven solely by the gravitational field giving rise to 'Rayleigh' convection while the inclusion of a free surface means that surface tension gradients also determine the onset conditions as well as the planform of convective flow. The convective flow driven solely by surface tension gradients is known as the Marangoni effect (2) and the physical nature of this problem has been recently reviewed by Koschmieder (3). The present paper is concerned with the effect of lateral side walls on convection with a free surface. The objectives of this work were to 1) delineate the critical conditions and patterns at the onset of free surface convection and indicate, for particular fluid systems, the regions where experiments are best conducted and 2) compare the calculations to recent experiments of Koschmieder and Prahl (4).

Instability of the quiescent state is often analyzed by linearizing the boundary value problem about the trivial state and inspecting the eigen-spectrum. The associated Marangoni and Rayleigh numbers are the critical operating parameters or bifurcation points while the eigenfunctions represent the patterns at the onset point. Theoretical work on convective onset for purely Marangoni flow in bounded containers with realistic boundary conditions was done by Vrentas et al. (5), Winters et al. (6), Dijkstra (7), Duh (8), Van der Vooren and Dijkstra (9). These papers were, however, restricted to calculations of two dimensional disturbances in either a right circular cylinder or in a rectangle. Chen et al. (10) attempted to study the pattern formation at the onset in a right circular cylinder but the results of their study are suspect in that the large aspect ratio results were not consistent with the

¹This communication is a brief summary of a paper which is to appear in the Journal of Colloid and Interface Science (1995)

²Communications to be addressed to this author

wide geometry calculations of the classical theory by Nield (11), at least for the case of 'zero' azimuthal dependence. Moreover, the side wall conditions of 'insulation' are rarely compatible with experimental conditions that attempt to satisfy the so called 'conducting' case i.e; the situation where the side walls have the same thermal conductivity as the operating fluid in question. Recently, Wagner, Narayanan and Friedrich (12), assuming a flat surface, have completed three-dimensional nonlinear calculations. Here too, the restrictions on the problem were severe in that the gravitational field was entirely eliminated and the side walls were assumed to be thermally insulating. Nevertheless their results were curious in that they indicated a lack of transcritical behavior for small aspect ratios and also showed a transition from three to two dimensional flow as the supercritical Marangoni number was increased. Note that their results were obtained for the pure Marangoni problem. Other studies in bounded geometries for lateral boundary conditions of vanishing vertical component of vorticity (cylindrical geometry) or vanishing stress (rectangular geometry) were performed by Rosenblat et al. (13 and 14) and McTaggart (15). Dijkstra (16) recently has given the results for a realistic rectangular geometry. A common result of all of the three-dimensional calculations is that the aspect ratio and geometry strongly affect the flow structure at and beyond the critical or onset point.

On account of the restrictions either on the dimensionality or the nature of the boundary conditions or the gravitational level, these earlier calculations have limitations and are not quite compatible with experiments. The present work is motivated by the absence of any 3-D calculations of the convection problem in a laterally bounded container where both Rayleigh and Marangoni effects are taken into account and also where realistic conditions on the side walls are imposed. We expect that such a study with both buoyancy and interfacial tension gradients will provide very useful information on the development of planform structure and will provide the real basis for future nonlinear numerical studies which in turn are necessary for the correct interpretation of experiments. This, therefore, is the underling reason for the present communication.

The Model

The model that was analyzed describes a liquid such as oil underlying a gas such as helium or air as depicted in Figure 1. The governing equations were derived in a manner similar to that of Vrentas et al. (5) with different scale factors. The lower solid boundary has a constant temperature T_0 and the upper solid surface has a temperature T_1 respectively. T_1 is the temperature of the interface in the conductive state. To simulate the convection the Boussinesq form of the continuity, Navier-Stokes and energy equations were used. In what follows the free surface is assumed to be non deformable. This assumption is mildly restrictive for the case of a liquid superposed by a quiescent gas as seen by the results of Zhao et al.(17). However in the case of the pure Marangoni problem relaxation of this assumption is known to lead to a long wave length instability in an unbounded container. The equations of continuity, momentum, and energy were non-dimensionalized using different scales (18) and then linear instability theory was applied. The solution technique rests on a spectral decomposition in the manner used by Chen et al. (10) and Hardin et al. (19). The 'radial' spectral functions that were used depend on the side wall conditions. The flow pattern at the onset of convection was obtained from the calculation. These were determined from the eigenfunctions while the eigenvalues were identified as the critical Marangoni numbers. The Rayleigh and Biot numbers as well as aspect ratios and azimuthal mode 'm' were fixed in any given calculation. Only the steady equations were considered because the principle of exchange of stability was assumed. Earlier calculations of Vidal and Acrivos (20) as well as Takashima (21) indicate this for the unbounded layer case.

Discussion of the Results

General Comments:

In order to check the reliability of the numerical scheme and the accuracy of the spectral representation, the first three critical Marangoni numbers or bifurcation points were calculated for the axisymmetric case ($m=0$) and $Ra=0$ for a variety of aspect ratios at Biot numbers equal to 1 and 100 and these were compared with the corresponding results of Vrentas et al. (5). All of these results are depicted in Table 1. Moreover, the first bifurcation point was compared with the corresponding results of Vrentas et al. (5) for the case of $Ma=0$, and $Bi=100$, and these are shown at the bottom of Table 1. We see a discrepancy for the pure Marangoni problem only at small aspect ratios while the comparison for the pure Rayleigh problem is very good. This discrepancy is reduced for large aspect ratios.

	Bi	A = 1		A = 2		A = 4		A = 8	
		This Work	Reference'						
Ma for First Bifurcation Point	1	229.5	206.0	133.9	125.0	119.0	120.7	115.3	117.2
	100	4579.0	4272.5	3585.0	3589.4	3316.4	3376.1	3264.0	3318.8
Ma for Second Bifurcation Point	1	542.8	531.6	184.0	167.1	131.8	128.2	118.4	119.4
	100	7281	7030.5	4360.0	4197.5	3492.7	3521.4	3311.0	3365.7
Ma for Third Bifurcation Point	1	972.3	1022.9	292.3	282.3	152.9	149.0	124.3	126.1
	100	10060.0	10051.1	5285.0	4948.9	3813.5	3863.6	3391.0	3446.1
Ra for First Bifurcation Point	100	1978.6	1939.0	1252.9	1234.9	1111.3	1110.8	1087.5	1094.5

Table 1. Comparison of the first three critical Ma for $Ra=0$ and the first critical Ra for $Ma=0$ for various A and Bi assuming insulating side walls and $m=0$, with Vrentas et al. (5).

Comparison with Experiments:

As mentioned earlier, there are very few experiments in bounded geometries for the combined Rayleigh-Marangoni problem. Notable are those of Koschmieder and Prahl (4). It is observed that in an experiment one cannot fix the Rayleigh number and measure a critical Marangoni number, as

the real operating variable is the temperature difference and this variable occurs in both of the dimensionless groups. Therefore the critical temperature differences were calculated and the corresponding critical Rayleigh and Marangoni numbers were reported in Table 2 for the same conditions as reported by Koschmieder and Prahl (4).

Case	m	Calculated Ma	Comments	Koschmieder &
1	0	109.94	A=2.16, Ra/Ma = 1.225, Bi= 0.85, depth of air layer = 0.5 mm depth of the fluid = 2.593 mm	Ma= 87.5, m = 0 $\Delta T = 7.16^\circ\text{C}$
	1	116.67		
	2	114.83		
	3	119.66		
2	0	104.50	A= 2.655, Ra/Ma = 0.81, Bi= 0.696, depth of air layer = 0.5 mm depth of the fluid = 2.109 mm	Ma= 81, m = 2 $\Delta T = 8.14^\circ\text{C}$
	1	108.00		
	2	104.70		
	3	106.70		
3	0	98.80	A= 3.295, Ra/Ma = 0.526, Bi= 0.56, depth of air layer = 0.5 mm depth of the fluid = 1.699 mm	Ma= 76.5, m = 3 $\Delta T = 9.55^\circ\text{C}$
	1	103.10		
	2	99.31		
	3	99.81		
4	0	97.90	A= 4.145, Ra/Ma = 0.81 Bi= 0.7, depth of air layer = 0.5 mm depth of the fluid = 2.12 mm	Ma= 74, m= 3 $\Delta T = 7.4^\circ\text{C}$
	1	100.84		
	2	98.30		
	3	98.32		
5	0	94.07	A= 2.82, Ra/Ma = 3.25, Bi= 1.39, depth of air layer = 0.5 mm depth of the fluid = 4.22 mm	Ma= 75, m = 3 $\Delta T = 3.77^\circ\text{C}$
	1	98.80		
	2	93.79		
	3	94.90		

Table 2. Comparison of the experimental results of Koschmieder and Prahl with calculations for various m and with conducting side wall conditions.

The thermophysical properties of the silicone oil/air system used in the experiments are given in Table 3 along with the properties of helium which is a gas that will be used by us in future experiments. The results for various 'm' are also given in Table 2. The side wall conditions in the calculations were assumed to be of the 'conducting' type. It is seen that most of our calculated critical Marangoni

numbers are above the experimental measurements by about 22%. This therefore requires an explanation.

One reason that the predicted critical Marangoni numbers are uniformly greater than the measured Marangoni numbers is partly due to the transcritical nature of Rayleigh Marangoni convection. Recent unpublished nonlinear calculations done by the second author of this study show that the transcritical region for the experiments are within 5% of the critical.

Another reason for the discrepancy is due to possible imperfections induced by side walls. In studies involving the influence of side walls, small depths mean that the diameter of the containers must also be small. This leads to the possibility that side wall imperfections will influence the onset conditions and patterns. These imperfections become more pronounced when the temperature differences are substantial and it is to be noted that the critical temperature difference for onset increases with a decrease in liquid depth. Thus even small imperfections can cause us to lose the bifurcation or sudden onset nature of the problem. A weak flow ensues and an increase in the temperature difference causes the solution to move along the vicinity of the first branch emanating from the first bifurcation point.

A third reason for the discrepancy between the model and experiments is due to an uncertainty in thermophysical properties. The 'over prediction' of the critical Marangoni numbers is entirely consistent with the fact that visual detection of the onset point is known within 10% and most but not all of the thermophysical properties are known within 10%. The greatest uncertainty in thermophysical properties is in the dynamic viscosity. It has been our past experience (22) that Dow Corning silicone oils which are labeled 100 centipoise often have a mean dynamic viscosity of about 15-20% less than what that label would indicate. This fact alone is enough to explain the apparent discrepancy between our predicted results and those reported by Koschmieder and Prahl making their adjusted results very close to our predictions. These facts in conjunction with the imperfections cited above can explain the theoretical over prediction of the experimentally determined critical Marangoni numbers.

	α °C ⁻¹	ν cm ² /s	κ cm ² /s	k W/cm K	ρ g/cm ³	$(-\partial\sigma/\partial T)$ oil-fluid dyne/cm. °C
Silicone Oil	0.00096	1	0.001095	0.001588	0.968	0.05
Air	0.00333	0.157	0.1818	0.000262	0.0012	
Helium	0.003326	1.22	1.770	0.0015	0.0001627	

Table 3. Physical properties of fluids used in typical experiments.

We now comment on the predicted and observed patterns. The predicted pattern at the onset of convection is the same as obtained by Koschmieder and Prahl for the aspect ratio of 2.16 but differs from the experimental ones for the other aspect ratios that are reported in Table 2. The calculated bifurcation points or critical Ma_c that correspond to the various values of 'm', are clustered for all aspect ratios greater than 2.16. In fact for the larger aspect ratios it is seen that the first two critical Ma are within about 1 % of each other. Now it may be noted from the work of Tavantzis et-

al. (23) and Matkowsky and Reiss (24) that characteristics of the solutions along the first branch are strongly influenced not only by the eigenvector at the first bifurcation point but also by the eigenvectors that are associated with the subsequent nearby eigenvalues. As a result small imperfections on problems with moderate aspect ratios, where bunching of solutions takes place will easily cause us to experimentally obtain patterns that are different from the ones that are predicted by the first bifurcation point obtained by linear theory which assumes perfect or ideal conditions. In other words, mild imperfections and clustering of bifurcation points cause us to believe that there is no substantial contradiction between the predicted patterns in our results and those of Koschmieder and Prahl (4). While this is so, it suffices to say that experiments are better predicted by calculations that consider both the non ideal or 'imperfect' nature of walls and the transient nonlinear interactions so as to allow us to go beyond the onset point of convective flow and also consider transcritical behavior.

Figures 2a through 5b represent the three-dimensional patterns and the corresponding planforms at a specific 'z' level for various values of 'm'. It is clear that for 'm' = 0 we have axisymmetry while for 'm' = 1 the flow is exactly antisymmetric every π radians. When 'm' = 2, 3 the antisymmetry occurs every $\pi/2$ and $\pi/3$ radians. The calculations are shown for case 5 in Table 2 and it may be seen that the experiments of Koschmieder and Prahl (4) indicate a 'm' = 3 flow while calculations predict 'm' = 2 to be the most unstable. However the modes 'm' = 0, 2, and 3 are within 1% of each other and given the difficulty in controlling temperature differences, it is conceivable that pattern switching could easily take place.

We point out that the second author has, in collaboration, with others recently conducted experiments in three different aspect ratios (2.53, 1.49 and 0.75). The modes that are predicted by our method for these aspect ratios are $m=0$, $m=0$ and $m=1$ respectively and coincide precisely with those observed in these experiments. Moreover the mode $m=2$ is very close to the $m=0$ mode for the aspect ratio 2.53 and the experiments also bear this out by generating pattern switching behavior.

Summary:

The critical conditions and patterns for the onset of three-dimensional convection in bounded circular containers were obtained. It was found that for a large range of aspect ratios the axisymmetric mode or 'm=0' mode is the most unstable and that codimension 2 points occur for either large or somewhat small (< 1.0) aspect ratios. The comparison with existing experimental patterns is within reason but not exact and we have rationalized that this is possibly due to the effect of imperfections on geometries that encourage closely bunched eigenmodes. A reason for the apparent discrepancy between predicted and experimentally determined critical Ma is that the experimental results have assumed the correctness of the viscosity of the test fluid as stated by the manufacturer and we believe that the actual viscosity is substantially less. We believe that this is the major reason that might explain the difference in reported critical values of the experiment and those predicted by the theory. Calculations in deep layers and narrow containers show promise of future experimental verification.

Acknowledgment:

Support from NSF grant CTS 93 07819 and part support from NASA 1-1474 is gratefully acknowledged. The computations were performed on the Cray C-90 at the Pittsburgh Supercomputing Center.

References

1. Bénard, H., Rev. Gén. Sciences Pure Appl., 11, (1900).
2. Pearson, J. R. A., J. Fluid Mech. 4, 489 (1958).
3. Koschmieder, E. L., "Bénard cells and Taylor vortices", Cambridge University Press, (1993).
4. Koschmieder, E. L. and Prahl, S. A., J. Fluid Mech. 251, 571 (1990).
5. Vrentas, J. S., Narayanan, R. and Agrawal, S. S., Int. J. Heat and Mass Transfer 24(9), 1513 (1981).
6. Winters, K. H., Plesser, T. and Cliffe, K. A., Physica D 29, 387 (1988).
7. Dijkstra, H. A., J. Fluid Mech. 243, 73 (1992).
8. Duh, J. C., IKI/AIAA Microgravity Science Symposium Proceedings, (1991).
9. Van der Vooren, A. I. and Dijkstra, H. A., Computers and Fluids 17(3), 467 (1989).
10. Chen, J.-C., Chen, J.-Y., and Hong, Z.-C., Paper IAF 91-393, 42, Cong. Int. Astronautical Federation, Montreal, October (1991).
11. Nield, D. A., J. Fluid Mech. 19, 341 (1964).
12. Wagner, C., Friedrich, R. and Narayanan, R., Phys. Fluids 6(4), 1425 (1994).
13. Rosenblat, S., Davis, S. H., and Homsy, G., J. Fluid Mech. 120, 91 (1982a).
14. Rosenblat, S., Davis, S. H., and Homsy, G., J. Fluid Mech. 120, 123 (1982b).
15. McTaggart, C. L., J. Fluid Mech. 134, 301 (1983).
16. Dijkstra, H. A., Micrograv. Sci. Technol. VII/4, 307 (1995).
17. Zhao, A. X., Wagner, C., Narayanan, R., and Friedrich, R., "Bilayer Rayleigh-Marangoni Convection -- Transitions in Flow Structures at the Interface," to appear in Proc. Roy. Soc. A, 451 (1995).
18. Zaman, A. A., and Narayanan, R., "Interfacial and Buoyancy Driven Convection - The Effect of Geometry and Comparison with Experiments," to appear in the Journal of Colloid and Interface Science, (1995).
19. Hardin G. R., Sani, R. L., Henry, D. and Roux, B., Int. J. Num. Methods in Fluids 10, (1990).
20. Vidal, A. and Acrivos, A., Phys. Fluids 9(3), 615 (1966).
21. Takashima, M., J. Phys. Soc. of Japan, 50(8), 2745 (1981).
22. Zhao, A. X., Moates, C. and Narayanan, R., Phys. Fluids, 7(7), 1576 (1995).
23. Tavantzis, J., Reiss, E.L., and Matkowsky, B. J., SIAM J. Appl. Math. 34(2), 322 (1978).
24. Matkowsky, B. J. and Reiss, E. L., SIAM J. Appl. Math. 33, 230 (1977).

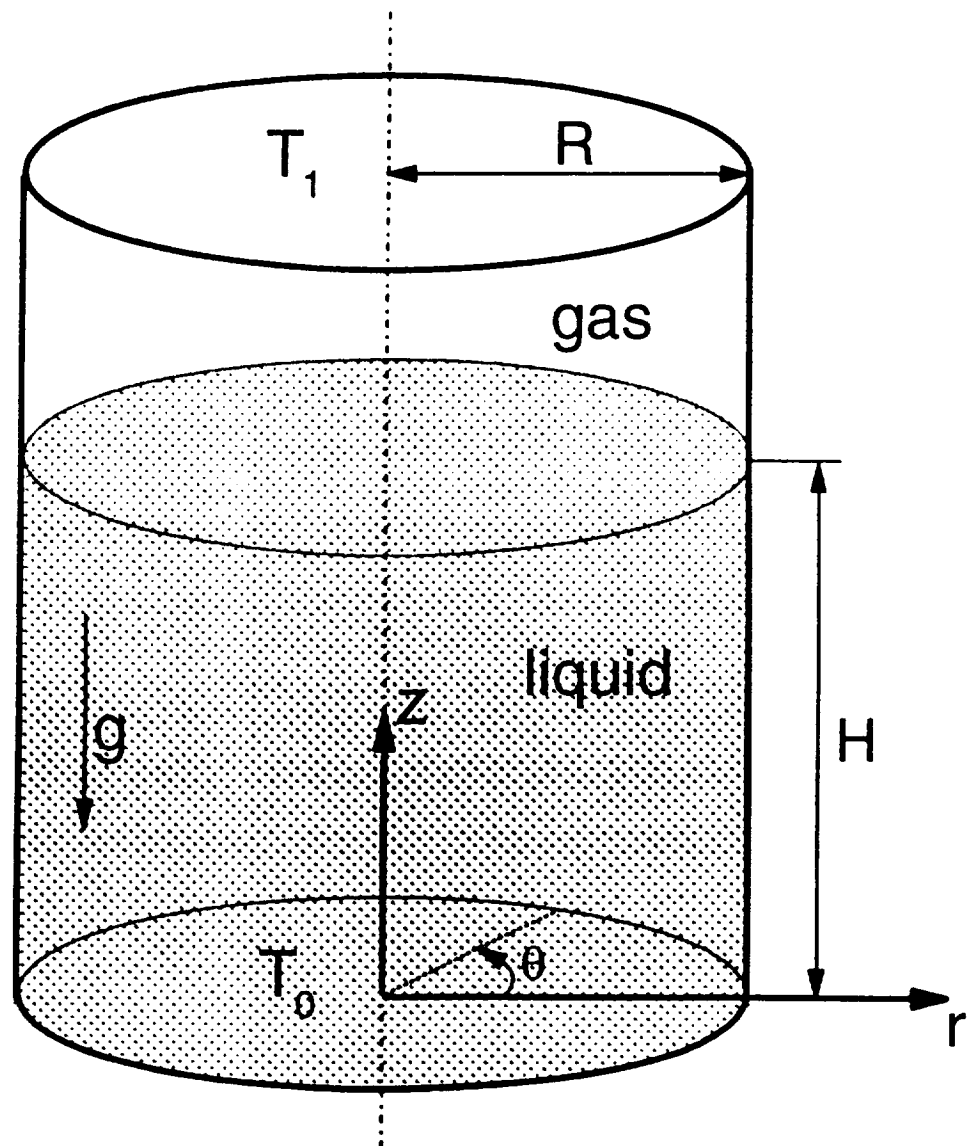
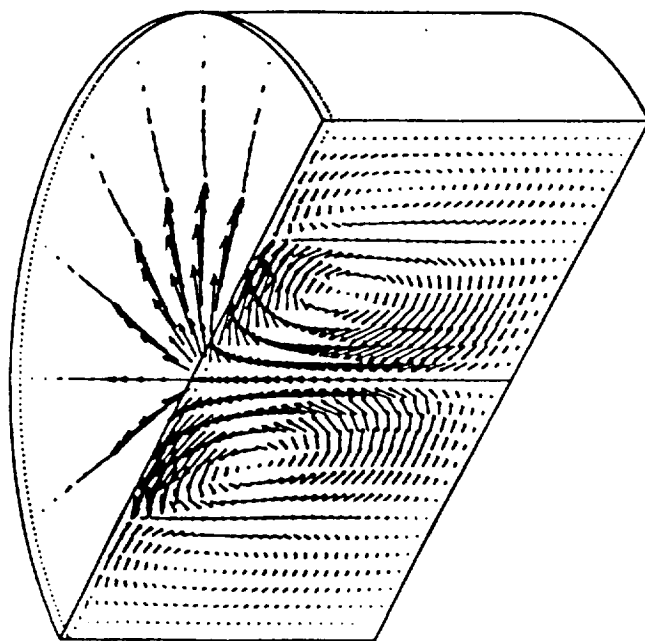
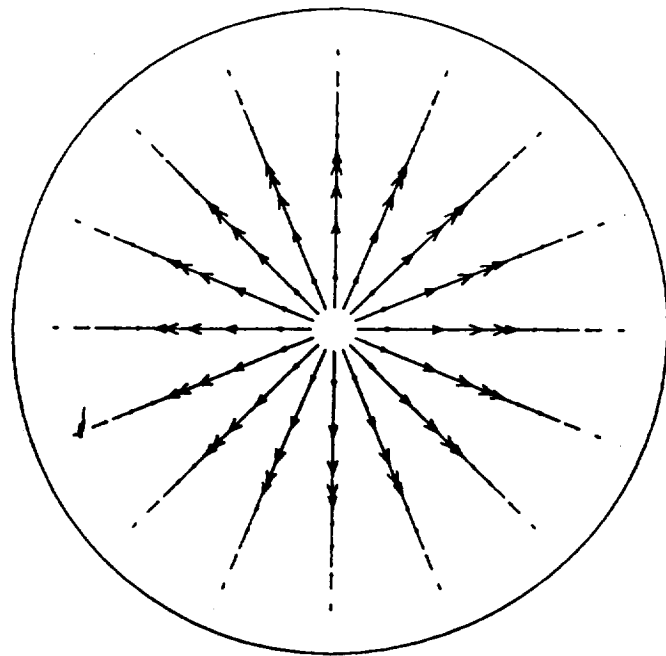


Figure 1. Schematic of the physical system.

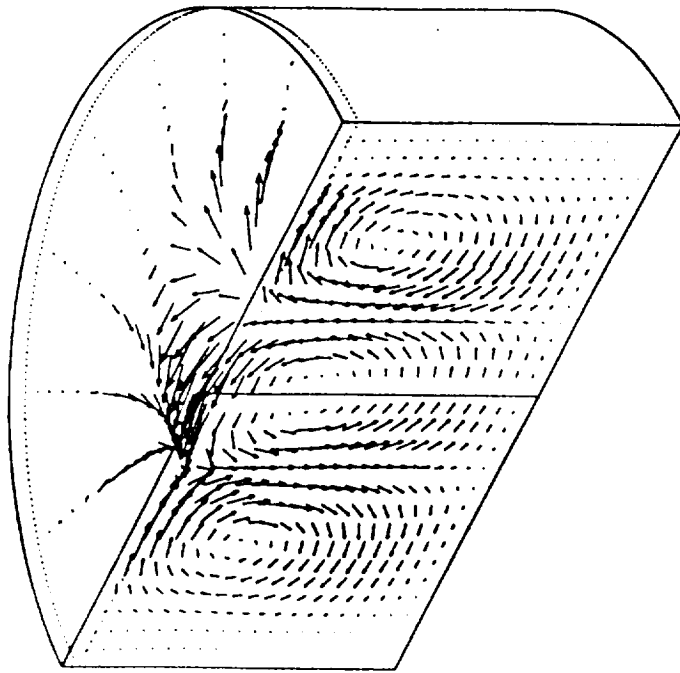


(a)

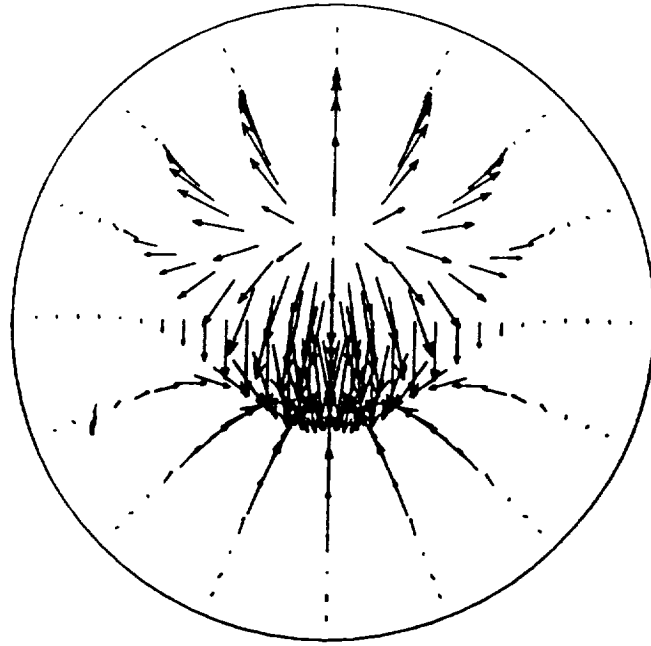


(b)

Figure 2. Depiction of 3-D profiles and planforms of the velocity eigen solutions at $m=0$ with $Ra=305.85$, $Ma=94.07$, and $A=2.82$.

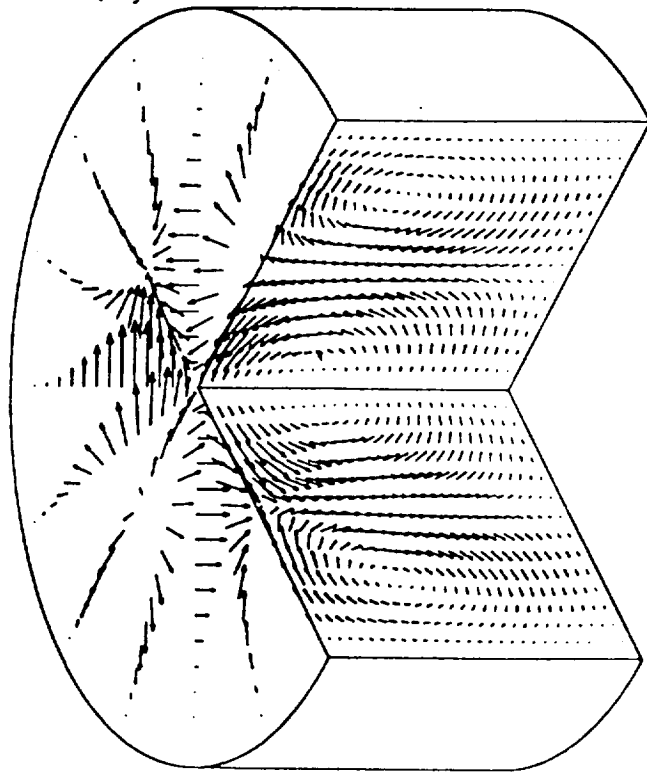


(a)

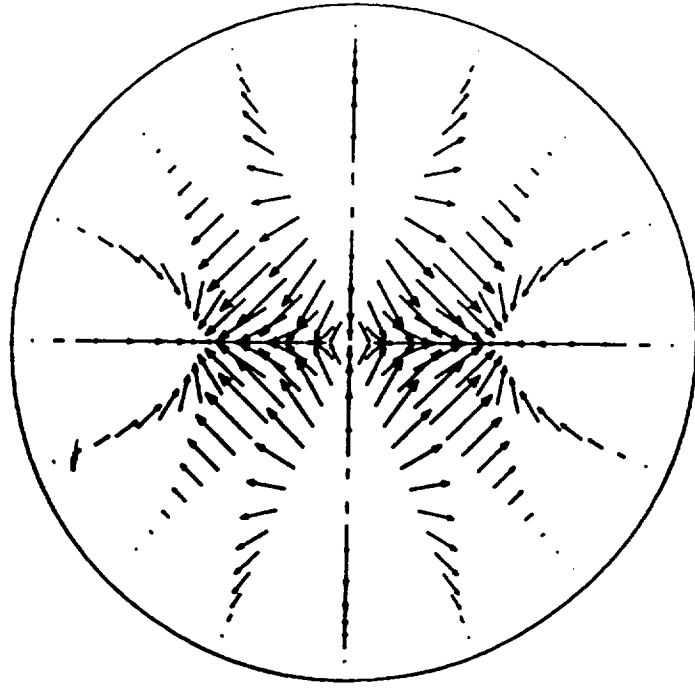


(b)

Figure 3. Depiction of 3-D profiles and planforms of the velocity eigen solutions at $m=1$ with $Ra=319.35$, $Ma=98.28$, and $A=2.82$.

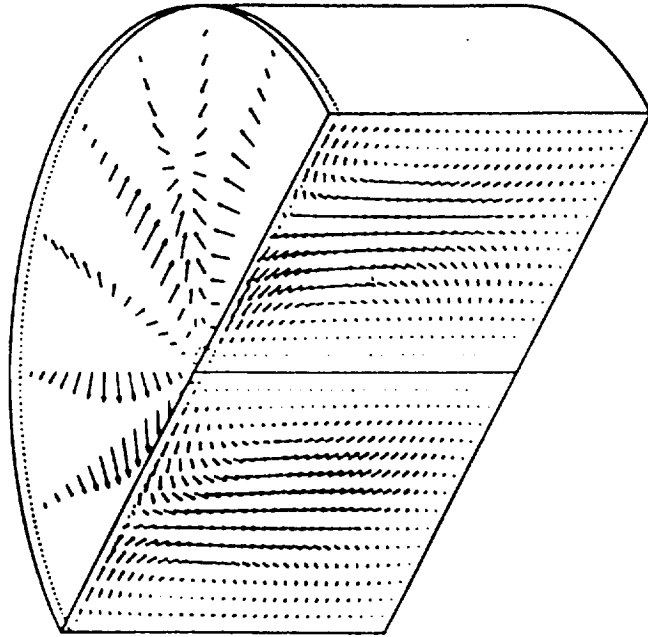


(a)

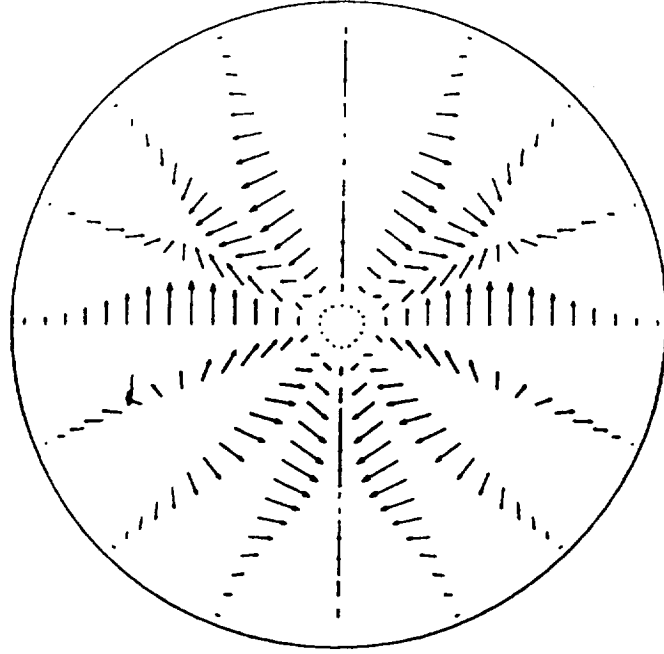


(b)

Figure 4. Depiction of 3-D profiles and planforms of the velocity eigen solutions at $m=2$ with $Ra=304.85$, $Ma=93.8$, and $A=2.82$.



(a)



(b)

Figure 5. Depiction of 3-D profiles and planforms of the velocity eigen solutions at $m=3$ with $Ra=308.43$, $Ma=94.9$, and $A=2.82$.

Interfacial and Buoyancy-Driven Convection—The Effect of Geometry and Comparison with Experiments

ABBAS A. ZAMAN AND RANGA NARAYANAN¹

Department of Chemical Engineering, University of Florida, Gainesville, Florida 32611

Received June 28, 1995; accepted October 25, 1995

In this study, pattern formation at the bifurcation point from the quiescent state for free surface convection in circular containers is determined. A linearized instability calculation that employs three-dimensional disturbances in the presence of physically realistic side wall boundary conditions is made. The results of the present study will provide a very useful asymptotic limit for nonlinear numerical computations. Under restrictive conditions the current calculations check favorably with those of earlier workers. The results of these studies are compared with the experiments of Koschmieder and Prahl (*J. Fluid Mech.* 251, 571, 1990). © 1996 Academic Press, Inc.

Key Words: Marangoni–Bénard convection; instability; pattern formation; bifurcation.

INTRODUCTION

The onset of flow from a quiescent state, when a layer of fluid is heated from below with an upper free surface, is one of the classical problems of fluid mechanical instabilities (1) and also the subject of many investigations. In this problem, a layer of fluid with an upper free surface is subjected to a temperature gradient that is perpendicular to the interface and one of the goals is to find the critical conditions and the associated pattern for the onset of flow from an erstwhile quiescent state. Curiously, there is a dearth of good experiments on this problem and most of these have been conducted in geometries of large lateral extent, while the theories that model these experiments assume the absence of vertical side walls. When a free surface is absent, convection is driven solely by the gravitational field giving rise to “Rayleigh” convection, while the inclusion of a free surface means that surface tension gradients also determine the onset conditions as well as the planform of convective flow. The convective flow driven solely by surface tension gradients is known as the Marangoni effect (2) and the physical nature of this problem has been recently reviewed by Koschmieder (3). The present paper is concerned with the effect of lateral side walls on convection with a free surface. The problem

of pattern formation as affected by side walls is strongly connected to crystal growth by the Bridgman technique. In fact, during crystal growth, the aspect ratio is ever changing on account of the moving interface. But this is not the only reason why this problem is being studied. Convection experiments are necessarily done in closed containers and the correct interpretation of these experiments requires a theory that is closely connected to them. Moreover detailed numerical calculations that examine the splitting of solutions and generation of cascaded bifurcation as the aspect ratio of the containers increase must be checked with appropriate asymptotic models of which the current study is an important one.

Experiments by Koschmieder and Prahl (4) on convection in a laterally bounded container show the marked effect that the geometry has on pattern selection. The theoretical investigations of the onset of free surface convection in bounded containers are restricted and are approximate in many ways and none thus far have been posed so as to closely replicate experimental conditions. As a result, it has not been heretofore possible to examine whether the essential qualitative features of the actual problem have been retained by the approximate models. It is therefore the objective of this work to delineate the critical conditions and patterns at the onset of free surface convection and indicate, for particular fluid systems, the regions where experiments are best conducted. Another objective is to compare the calculations to recent experiments of Koschmieder and Prahl (4).

Instability of the quiescent state is often analyzed by linearizing the boundary value problem about the trivial state and inspecting the eigenspectrum. The associated Marangoni and Rayleigh numbers are the critical operating parameters or bifurcation points, while the eigenfunctions represent the patterns at the onset point. Theoretical work on convective onset for purely Marangoni flow in bounded containers with realistic boundary conditions was done by Vrentas *et al.* (5), Winters *et al.* (6), Dijkstra (7), Duh (8), and Van der Vooren and Dijkstra (9). These papers were, however, restricted to calculations of two-dimensional disturbances either in a right circular cylinder or in a rectangle. Some of these studies indicated the existence of a transcritical region in the vicinity of the onset of flow. This means that convec-

¹ To whom correspondence should be addressed.

tive flow could begin ahead of the theoretically predicted bifurcation point or onset point. The same studies also showed that the transcritical region decreases as the width of the container increases. Chen *et al.* (10) attempted to study the pattern formation at the onset in a right circular cylinder but the results of their study are suspect in that the large aspect ratio results were not consistent with the wide geometry calculations of the classical theory by Nield (11), at least for the case of "zero" azimuthal dependence. Moreover, the side wall conditions of "insulation" are rarely compatible with experimental conditions that attempt to satisfy the so called "conducting" case, i.e., the situation where the side walls have the same thermal conductivity as the operating fluid in question. Recently, Wagner *et al.* (12), assuming a flat surface, have completed three-dimensional nonlinear calculations. Here too, the restrictions on the problem were severe in that the gravitational field was entirely eliminated and the side walls were assumed to be thermally insulating. Nevertheless their results were curious in that they indicated a lack of transcritical behavior for small aspect ratios and also showed a transition from three- to two-dimensional flow as the supercritical Marangoni number was increased. Note that their results were obtained for the pure Marangoni problem. Other studies in bounded geometries for lateral boundary conditions of vanishing vertical component of vorticity (cylindrical geometry) or vanishing stress (rectangular geometry) were performed by Rosenblat *et al.* (13, 14) and McTaggart (15). Dijkstra (16) recently has given the results for a realistic rectangular geometry. A common result of all of the three-dimensional calculations is that the aspect ratio and geometry strongly affect the flow structure at and beyond the critical or onset point.

On account of the restrictions either on the dimensionality or on the nature of the boundary conditions or the gravitational level, these earlier calculations have limitations and are not quite compatible with experiments. The present work is motivated by the absence of any 3-D calculations of the convection problem in a laterally bounded container where both Rayleigh and Marangoni effects are taken into account and also where realistic conditions on the side walls are imposed. We expect that such a study with both buoyancy and interfacial tension gradients will provide very useful information on the development of planform structure and will provide the real basis for future nonlinear numerical studies which in turn are necessary for the correct interpretation of experiments. This, therefore, is the underling reason for the present communication.

THE MODEL

The model that was analyzed describes a liquid such as oil underlying a gas such as helium or air as depicted in Fig. 1. The governing equations were derived in a manner similar to that of Vrentas *et al.* (5) with different scale factors and

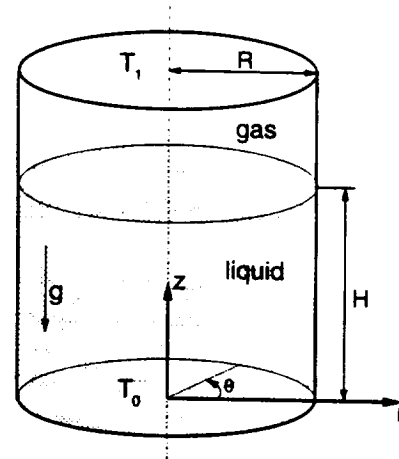


FIG. 1. Schematic of the physical system.

so, for brevity, the intermediate details are dispensed with. The lower solid boundary has a constant temperature T_0 and the upper solid surface has a temperature T_1 , respectively. T_i is the temperature of the interface in the conductive state. To simulate the convection the Boussinesq form of the continuity, Navier–Stokes, and energy equations were used.

In order to get nondimensional forms of the above-mentioned equations, the scale factors for radial and axial distance, velocity, time, and pressure were introduced. These are R , H , $\sigma_1 \beta H / \mu$, $(H)^2 / \kappa$, and $\sigma_1 \beta$, respectively. Here σ_1 , which is usually positive, is the temperature coefficient of surface tension, β is the temperature gradient in the liquid, κ is the thermal diffusivity of the lower or liquid phase, μ is its dynamic viscosity, and H is its depth. The dimensionless temperature T was scaled with respect to the temperature gradient in the liquid phase. In what follows, the free surface is assumed to be nondeformable. This assumption is mildly restrictive for the case of a liquid superposed by a quiescent gas as seen by the results of Zhao *et al.* (17). However, in the case of the pure Marangoni problem relaxation of this assumption is known to lead to a long wavelength instability in an unbounded container.

The linearized equations of continuity, momentum, and energy will be given below. Here P is the pressure field and Ra is the Rayleigh number referred to the lower phase and Ma is the Marangoni number, while Pr is the Prandtl number. U , V , and W are the dimensionless radial, azimuthal, and vertical components of velocity, respectively. Assuming the Boussinesq approximation, the perturbed form for the dependent variables follows.

The continuity equation is

$$\frac{1}{Ar} \frac{\partial}{\partial r} (rU) + \frac{1}{Ar} \frac{\partial V}{\partial \theta} + \frac{\partial W}{\partial z} = 0. \quad [1]$$

The r , θ , and z components of the equations of motion for an incompressible Newtonian fluid become

$$\text{Pr}^{-1} \frac{\partial U}{\partial t} = -\frac{1}{A} \frac{\partial P}{\partial r} + \left(\nabla^2 - \frac{1}{A^2 r^2} \right) U - \frac{2}{A^2 r^2} \frac{\partial V}{\partial \theta} \quad [2]$$

$$\text{Bi} = \frac{hH}{k}, \quad [12]$$

$$\text{Pr}^{-1} \frac{\partial V}{\partial t} = -\frac{1}{Ar} \frac{\partial P}{\partial \theta} + \left(\nabla^2 - \frac{1}{A^2 r^2} \right) V + \frac{2}{A^2 r^2} \frac{\partial U}{\partial \theta} \quad [3]$$

$$\text{Pr}^{-1} \frac{\partial W}{\partial t} = -\frac{\partial P}{\partial z} + \nabla^2 W + \text{Ma}^{-1} \text{Ra} T. \quad [4]$$

The energy equation is

$$\frac{\partial T}{\partial t} = \text{Ma}^{-1} \nabla^2 T + W. \quad [5]$$

Here A is the aspect ratio (R/H) and the Laplacian operator is

$$\nabla^2 = \frac{1}{A^2 r} \frac{\partial}{\partial r} \left(r \frac{\partial}{\partial r} \right) + \frac{1}{A^2 r^2} \frac{\partial^2}{\partial \theta^2} + \frac{\partial^2}{\partial z^2}. \quad [6]$$

For the lower solid surface that bounds the system no slip was assumed, yielding vanishing velocities. The temperature is assumed to be uniform at the bottom.

At the interface we have Newton's law of cooling

$$\frac{\partial T}{\partial z} + \text{Bi} T = 0. \quad [7]$$

A momentum balance at the interface gives the following conditions for the tangential component

$$\frac{\partial U}{\partial z} + \frac{1}{A} \frac{\partial T}{\partial r} = 0 = \frac{\partial V}{\partial z} + \frac{1}{Ar} \frac{\partial T}{\partial \theta}. \quad [8]$$

The equation of state for the interfacial tension was used. This takes into account the temperature dependence σ_1 of the interfacial tension in a manner similar to the equation of state for the density, in the Boussinesq approximation.

The Rayleigh and Marangoni numbers are given by

$$\text{Ma} = \frac{\sigma_1 \beta H^2}{\mu \kappa} \quad [9]$$

$$\text{Ra} = \frac{\rho \alpha \beta g H^4}{\mu \kappa}, \quad [10]$$

where α is the coefficient of thermal expansion.

The Prandtl (Pr) and Biot number (Bi) are given by

$$\text{Pr} = \frac{\mu}{\rho \kappa} \quad [11]$$

where h is the heat transfer coefficient and k is the thermal conductivity.

The thermal conditions on the side walls are either perfect insulation or perfect conduction. In the latter case the conductivity of the side walls are the same as that of the liquid so that both will have the same constant vertical temperature gradient in the trivial state.

The trivial solution to the above problem is given by the quiescent, conductive state in the liquid layer with the hydrostatic pressure gradient balancing the buoyancy. Linear instability theory was applied, by expanding the unknown variables in a perturbation series around the trivial solution. The solution technique rests on a spectral decomposition in the manner used by Chen *et al.* (10) and Hardin *et al.* (18). The "radial" spectral functions that were used depend on the side wall conditions. The flow pattern at the onset of convection was obtained from the calculation. These were determined from the eigenfunctions while the eigenvalues were identified as the critical Marangoni numbers. The Rayleigh and Biot numbers as well as aspect ratios and azimuthal mode m were fixed in any given calculation. Only the steady equations were considered because the principle of exchange of stability was assumed. Earlier calculations of Vidal and Acrivos (19) as well as Takashima (20) indicate this for the unbounded layer case. The three-dimensional linearized equations were converted into a simpler set using the transformations (10)

$$\begin{aligned} U(r, \theta, z) &= U'(r, z) \cos m\theta \\ V(r, \theta, z) &= V'(r, z) \sin m\theta \\ W(r, \theta, z) &= W'(r, z) \cos m\theta \\ P(r, \theta, z) &= P'(r, z) \cos m\theta \\ T(r, \theta, z) &= T'(r, z) \cos m\theta \end{aligned} \quad [13]$$

and

$$\begin{aligned} U' &= -\frac{\partial \varphi}{\partial z} \\ V' &= \frac{\partial \omega}{\partial z} \\ W' &= \frac{1}{Ar} \frac{\partial}{\partial r} (r\varphi) - \frac{m}{Ar} \omega. \end{aligned} \quad [14]$$

The dependent variables φ , ω , and T' were then expanded into various spatial components by applying a spectral representation as follows:

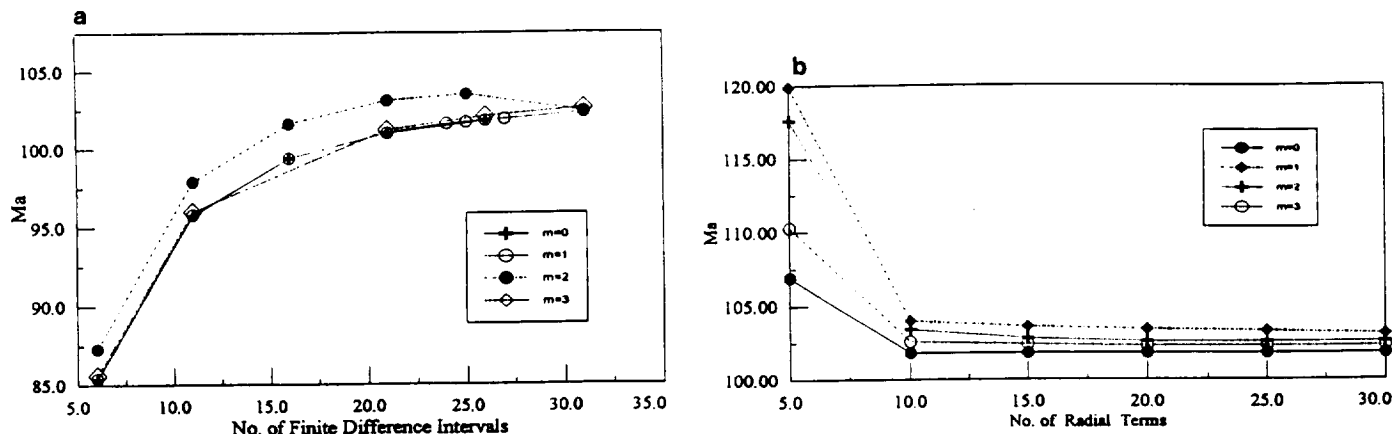


FIG. 2. (a) Variation of critical Ma number with the number of vertical grids for the case of Ra = 100, Bi = 1, and A = 8. (b) Variation of critical Ma number with the number of radial terms for the case of Ra = 100, Bi = 1, and A = 8.

$$\begin{aligned}
 \varphi &= \sum_{j=1}^n A_j^m(z) X_j^m(r) \\
 \omega &= \sum_{j=1}^n B_j^m(z) Y_j^m(r) \\
 T' &= \sum_{j=1}^n C_j^m(z) Z_j^m(r).
 \end{aligned}
 \tag{15}$$

The Appendix contains some of the essential details on the form of the spectral functions. The residuals obtained as a result of incorporating the spectral representation were made orthogonal to the basis functions as required in a Galerkin technique. This resulted in a set of ordinary differential equations that depended on the vertical coordinate. These were then finite differenced in the "vertical direction" with second-order accuracy and a set of linear homogeneous algebraic equations were obtained where Ra and Bi as well as aspect ratio and *m* were treated as input variables and the critical Marangoni numbers were obtained as eigenvalues. This last procedure was accomplished using an IMSL code G8CRG.

Figure 2 shows an example of the variation of critical Marangoni numbers with the number of vertical grid points and number of radial eigenfunctions used. It was typically seen that 25 radial terms and 30 vertical grid points sufficed to delineate the physical nature of the problem.

DISCUSSION OF THE RESULTS

General Comments

In order to check the reliability of the numerical scheme and the accuracy of the spectral representation, the first three critical Marangoni numbers or bifurcation points were calculated for the axisymmetric case (*m* = 0) and Ra = 0 for a variety of aspect ratios at Biot numbers equal to 1 and 100

and these were compared with the corresponding results of Vrentas *et al.* (5). All of these results are depicted in Table 1. Moreover, the first bifurcation point was compared with the corresponding results of Vrentas *et al.* (5) for the case of Ma = 0 and Bi = 100 and these are shown at the bottom of Table 1. We see a discrepancy for the pure Marangoni problem only at small aspect ratios while the comparison for the pure Rayleigh problem is very good. A brief explanation for this is offered.

The study of Vrentas *et al.* (5) involved two separate cases. These were the pure Marangoni and the pure Rayleigh problems. The eigenfunction in the former was the temperature field at the free surface and resulted from the consideration of a matrix of order *n* where *n* represents the number of radial terms during the spectral expansion. However, when Vrentas *et al.* (5) considered the pure Rayleigh problem the eigenmatrix was of order *n*² where now the number of radial and vertical terms in the eigenfunction expansion were equal. Had they looked at the combined Rayleigh–Marangoni case they would have an order *n*² matrix as well, no matter what value of Ra was chosen. Now, the larger the number of radial and vertical terms, the more accurate the result. And so we can expect the accuracy of the combined Rayleigh–Marangoni problem, in the limit of Ra = 0, to be lower than the pure Marangoni problem unless a very large number of terms are used. In the present study an eigenmatrix of order *n*(*k* – 1) results where *k* is the number of finite difference intervals in the vertical direction and *n* is the number of radial terms. Therefore the rate of convergence in our problem where Ra = 0 is different and lower than that in the pure Marangoni case studied by Vrentas *et al.* (5). This is why we have a discrepancy between our results. This discrepancy is reduced for large aspect ratios and as expected the comparison is quite favorable when the pure Rayleigh problem is considered.

Table 2 shows the calculated lowest critical Marangoni

TABLE 1
 Comparison of the First Three Critical Ma for $Ra = 0$ (Bifurcation Points) and the First Critical Ra for $Ma = 0$ for Various A and Bi Assuming Insulating Side Walls and $m = 0$, with Vrentas *et al.* (5)

	Bi	A = 1		A = 2		A = 4		A = 8	
		This work	Reference (4)						
Ma for first bifurcation point	1	229.5	206.0	133.9	125.0	119.0	120.7	115.3	117.2
	100	4579.0	4272.5	3585.0	3589.4	3316.4	3376.1	3264.0	3318.8
Ma for second bifurcation point	1	542.8	531.6	184.0	167.1	131.8	128.2	118.4	119.4
	100	7281.0	7030.5	4360.0	4197.5	3492.7	3521.4	3311.0	3365.7
Ma for third bifurcation point	1	972.3	1022.9	292.3	282.3	152.9	149.0	124.3	126.1
	100	10060.0	10051.1	5285.0	4948.9	3813.5	3863.6	3391.0	3446.1
Ra for first bifurcation point	100	1978.6	1939.0	1252.9	1234.9	1111.3	1110.8	1087.5	1094.5

numbers for a variety of aspect ratios and various m at different values of Ra and Bi . The last column of Table 2 gives the critical Marangoni numbers obtained from Nield (11) for the case of infinitely wide layers. It can be seen that the calculated results approach Nield's results for aspect ratios greater than 8 and are within the asymptotic values of Nield (11) by 1.2% for all the values of m assumed. It is further noted that the results of Chen *et al.* (10) did not approach Nield's values for the case of $m = 0$ and are therefore in disagreement with our calculations. It is felt that this is a consequence of inaccuracies in their calculations and in fact this is one reason that caused us to repeat the computations. We comment on this further in the Appendix.

Table 3 shows the comparison in critical Marangoni numbers between the case of insulated and conducting side walls and in nearly all cases it can be seen that the case of conducting side walls leads to higher Marangoni numbers, thereby indicating greater stability to disturbances. In this regard the problem is similar to the pure Rayleigh problem wherein one can show from self-adjoint operators that conducting side walls in a container of arbitrary shape leads to greater stability. A similar proof is not available for the combined Rayleigh-Marangoni problem. Likewise it can be shown from self-adjoint operators that the critical Rayleigh numbers in cylindrical containers scales with geometry such that

TABLE 2
 Critical Marangoni Number for Various m , Bi , and Ra for Insulating Walls

Ra	Bi	m	Critical Marangoni numbers for					Nield's result
			A = 1	A = 2	A = 3	A = 4	A = 8	
100	0	0	175.4	82.3	74.7	71.1	68.2	68.9
		1	107.8	87.2	73.1	71.6	68.7	
		2	145.6	87.3	72.2	70.8	68.1	
		3	235.2	89.9	77.9	69.6	68.2	
0	1	0	229.5	133.9	121.8	119.0	115.3	116.1
		1	177.7	133.6	127.2	119.5	115.9	
		2	203.5	142.5	119.0	118.5	115.5	
		3	297.8	143.2	123.6	118.2	115.1	
100	0.2	0	184.3	90.2	81.6	78.4	75.2	75.9
		1	119.3	93.9	81.4	78.5	76.1	
		2	155.0	96.7	78.9	78.4	75.0	
		3	246.2	98.2	84.7	76.8	75.2	

TABLE 3
Comparison of Critical Ma for Insulating and Conducting Side Walls and Various Ra, Bi, and m

Ra	Bi	m	Wall condition	Critical Marangoni Numbers for				
				A = 1	A = 2	A = 3	A = 4	A = 8
1	100	0	Insulating	219.8	120.7	108.5	105.7	101.8
			Conducting	239.5	121.9	109.5	105.6	101.8
1	100	2	Insulating	289.8	130.3	110.6	104.7	101.5
			Conducting	369.3	138.7	110.3	105.6	101.8

$$\frac{\partial(RaA^4)}{\partial(1/A)} < 0. \quad [16]$$

No such analytical result is available for the combined Rayleigh–Marangoni problem because of the non-self-adjoint nature of the linearized equations. Nevertheless, calculations were performed to inspect the behavior of critical Marangoni numbers with aspect ratios and these are shown in Fig. 3. Only for the case of $m = 1$ do local maxima and minima occur, whereas for all other values of m a nonmonotonic variation of Marangoni numbers with aspect ratios could not be detected. In fact there are regions where the Marangoni number changes very little and thereafter for a further increase in aspect ratio a drop in the computed critical Marangoni numbers is not seen.

Comparison with Experiments

As mentioned earlier, there are very few experiments in bounded geometries for the combined Rayleigh–Marangoni problem. Notable are those of Koschmieder and Prahl (4). It is observed that in an experiment one cannot fix the Rayleigh number and measure a critical Marangoni number, as the real operating variable is the temperature difference, and this variable occurs in both of the dimensionless groups.

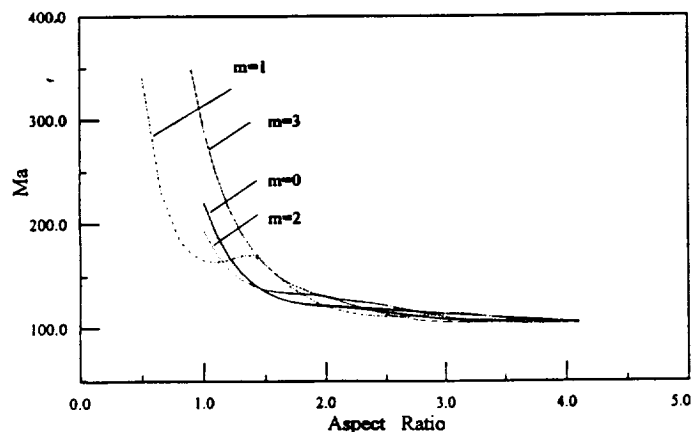


FIG. 3. Critical Marangoni numbers versus aspect ratio for various modes for the case of $Ra = 100$ and $Bi = 1$.

Therefore the critical temperature differences were calculated and the corresponding critical Rayleigh and Marangoni numbers are reported in Table 5 for the same conditions as reported by Koschmieder and Prahl (4). The thermophysical properties of the silicone oil/air system used in the experiments are given in Table 4 along with the properties of helium which is a gas that will be used by us in future experiments, on account of its high thermal conductivity, and for which some calculations are reported in this paper. The results for various m are also given in Table 5. The side wall conditions in the calculations were assumed to be of the “conducting” type. It is seen that most of our calculated critical Marangoni numbers are above the experimental measurements by about 22%. This therefore requires an explanation.

One reason that the predicted critical Marangoni numbers are uniformly greater than the measured Marangoni numbers is partly due to the transcritical nature of Rayleigh Marangoni convection. Recent unpublished nonlinear calculations done by the second author of this study show that the transcritical region for the experiments are within 5% of the critical.

Another reason for the discrepancy is due to possible imperfections induced by side walls. In studies involving the influence of side walls, small depths mean that the diameter of the containers must also be small. This leads to the possibility that side wall imperfections will influence the onset conditions and patterns. These imperfections become more pronounced when the temperature differences are substantial, and it is to be noted that the critical temperature difference for onset increases with a decrease in liquid depth. Thus even small imperfections can cause us to lose the bifurcation or sudden onset nature of the problem. A weak flow ensues and an increase in the temperature difference causes the solution to move along the vicinity of the first branch emanating from the first bifurcation point.

A third reason for the discrepancy between the model and experiments is due to an uncertainty in thermophysical properties. The “overprediction” of the critical Marangoni numbers is entirely consistent with the fact that visual detection of the onset point is known within 10% and most but not all of the thermophysical properties are known within

TABLE 4
Physical Properties of Fluids Used in Typical Experiments

	α ($^{\circ}\text{C}^{-1}$)	ν (cm^2/s)	κ (cm^2/s)	k (W/cm K)	ρ (g/cm^3)	$(-\partial\sigma/\partial T)$ oil-fluid ($\text{dyn}/\text{cm } ^{\circ}\text{C}$)
Silicone oil	0.00096	1	0.001095	0.001588	0.968	0.05
Air	0.00333	0.157	0.1818	0.000262	0.0012	
Helium	0.003326	1.22	1.770	0.0015	0.0001627	

10%. The greatest uncertainty in thermophysical properties is in the dynamic viscosity. It has been our past experience (21) that Dow Corning silicone oils which are labeled 100 cP often have a mean dynamic viscosity of about 15–20% less than what that label would indicate. This fact alone is enough to explain the *apparent* discrepancy between our predicted results and those reported by Koschmieder and Prahl, making their adjusted results very close to our predictions. These facts in conjunction with the imperfections cited above can explain the theoretical overprediction of the experimentally determined critical Marangoni numbers.

We now comment on the predicted and observed patterns. The predicted pattern at the onset of convection is the same as that obtained by Koschmieder and Prahl for the aspect ratio of 2.16 but differs from the experimental ones for the other aspect ratios that are reported in Table 5. From Table 5 one can also see that the calculated bifurcation points or

critical Ma that correspond to the various values of m , are clustered for all aspect ratios greater than 2.16. In fact for the larger aspect ratios it is seen that the first two critical Ma are within about 1% of each other. Now it may be noted from the work of Tavantzis *et al.* (22) and Matkowsky and Reiss (23) that characteristics of the solutions along the first branch are strongly influenced not only by the eigenvector at the first bifurcation point but also by the eigenvectors that are associated with the subsequent nearby eigenvalues. In other words the solution along the branch that emanates from the lowest critical Marangoni number has characteristics that depend not only on the eigenvector or pattern that is associated with the lowest Ma (bifurcation point) but also on the eigenvectors that are associated with the subsequent nearby higher bifurcation points. As a result, small imperfections on problems with moderate aspect ratios, where bunching of solutions takes place, will easily cause us to experimentally

TABLE 5
Comparison of the Experimental Results of Koschmieder and Prahl with Calculations for Various m and with Conducting Side Wall Conditions

Case	m	Calculated Ma	Comments	Koschmieder and Prahl's results
1	0	109.94	$A = 2.16$, $Ra/Ma = 1.225$, $Bi = 0.85$, depth of air layer = 0.5 mm, depth of the fluid = 2.593 mm	$Ma = 87.5$, $m = 0$, $\Delta T = 7.16^{\circ}\text{C}$
	1	116.67		
	2	114.83		
	3	119.66		
2	0	104.50	$A = 2.655$, $Ra/Ma = 0.81$, $Bi = 0.696$, depth of air layer = 0.5 mm, depth of the fluid = 2.109 mm	$Ma = 81$, $m = 2$, $\Delta T = 8.14^{\circ}\text{C}$
	1	108.00		
	2	104.70		
	3	106.70		
3	0	98.80	$A = 3.295$, $Ra/Ma = 0.526$, $Bi = 0.56$, depth of air layer = 0.5 mm, depth of the fluid = 1.699 mm	$Ma = 76.5$, $m = 3$, $\Delta T = 9.55^{\circ}\text{C}$
	1	103.10		
	2	99.31		
	3	99.81		
4	0	97.90	$A = 4.145$, $Ra/Ma = 0.81$, $Bi = 0.7$, depth of air layer = 0.5 mm, depth of the fluid = 2.12 mm	$Ma = 74$, $m = 3$, $\Delta T = 7.4^{\circ}\text{C}$
	1	100.84		
	2	98.30		
	3	98.32		
5	0	94.07	$A = 2.82$, $Ra/Ma = 3.25$, $Bi = 1.39$, depth of air layer = 0.5 mm, depth of the fluid = 4.22 mm	$Ma = 75$, $m = 3$, $\Delta T = 3.77^{\circ}\text{C}$
	1	98.80		
	2	93.79		
	3	94.90		

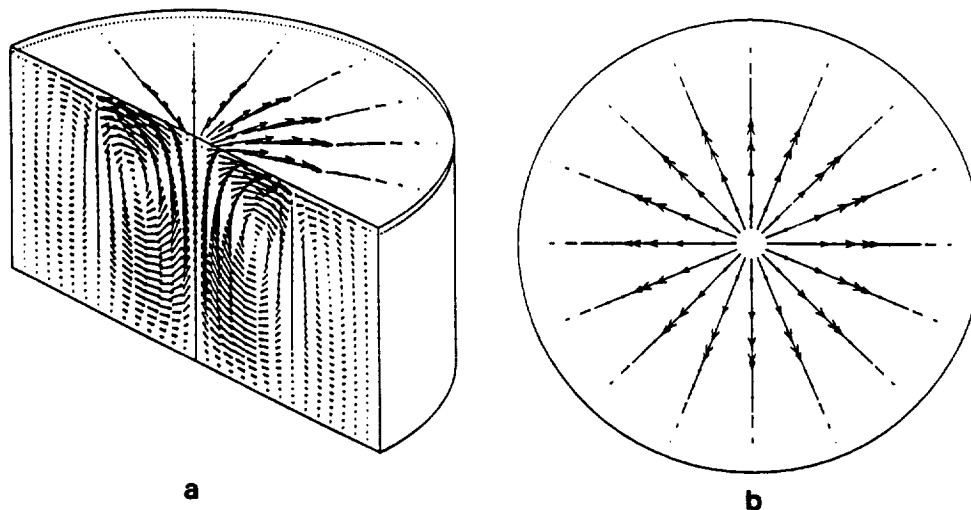


FIG. 4. Depiction of 3-D profiles and planforms of the velocity eigensolutions at $m = 0$ with $Ra = 305.85$, $Ma = 94.07$, and $A = 2.82$.

obtain patterns that are different from those predicted by the first bifurcation point obtained by linear theory which assumes perfect or ideal conditions. In other words, mild imperfections and clustering of bifurcation points cause us to believe that there is no substantial contradiction between the predicted patterns in our results and those of Koschmieder and Prahl (4). While this is so, it suffices to say that experiments are better predicted by calculations that consider both the nonideal or the "imperfect" nature of walls and the transient nonlinear interactions so as to allow us to go beyond the onset point of convective flow and also consider transcritical behavior. The utility of the present study is to provide a good starting point toward such nonlinear calculations.

Figures 4 through 7 represent the three-dimensional patterns and the corresponding planforms at a specific z level

for various values of m . It is clear that for $m = 0$ we have axisymmetry, while for $m = 1$ the flow is exactly antisymmetric every π radians. When $m = 2$ or 3 the antisymmetry occurs every $\pi/2$ and $\pi/3$ radians. The calculations are shown for case 5 in Table 5 and it may be seen that the experiments of Koschmieder and Prahl (4) indicate a $m = 3$ flow, while calculations predict $m = 2$ to be the most unstable. However, the modes $m = 0, 2,$ and 3 are within 1% of each other and given the difficulty in controlling temperature differences, it is conceivable that pattern switching could easily take place.

We point out that the second author has, in collaboration, with others recently conducted experiments in three different aspect ratios (2.53, 1.49, and 0.75). The modes that are predicted by our method for these aspect ratios are $m = 0,$ $m = 0,$ and $m = 1,$ respectively, and coincide precisely with

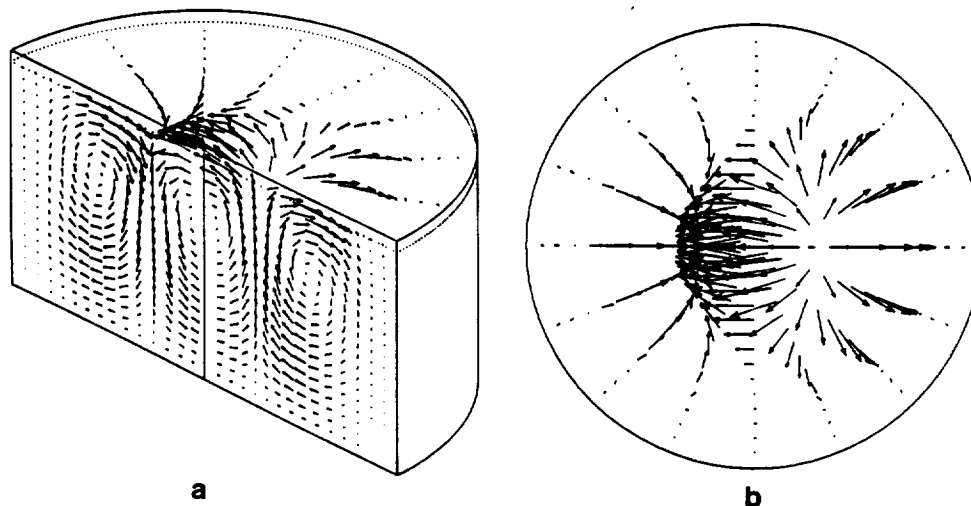


FIG. 5. Depiction of 3-D profiles and planforms of the velocity eigensolutions at $m = 1$ with $Ra = 319.35$, $Ma = 98.28$, and $A = 2.82$.

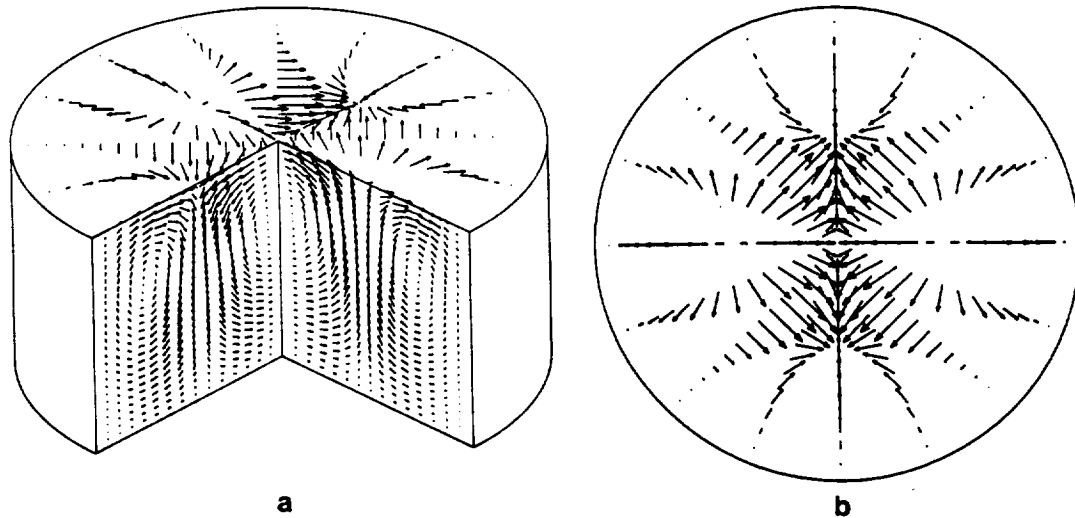


FIG. 6. Depiction of 3-D profiles and planforms of the velocity eigensolutions at $m = 2$ with $Ra = 304.85$, $Ma = 93.8$, and $A = 2.82$.

those observed in these experiments. Moreover the mode $m = 2$ is very close to the $m = 0$ mode for the aspect ratio 2.53, and the experiments also bear this out by generating pattern switching behavior.

Other Calculations

Finally, a set of results are presented in Table 6 for various fluid depths and Biot numbers, some of which may be verified experimentally. Using the thermophysical properties of silicone oil/air and various depths of liquid the critical Marangoni numbers are given for various values of m . Another parameter that is fixed is the Biot number and two values, viz. 1/7 and 1, were chosen. The value of Biot number of 1/7 corresponds to an air thickness equal to the liquid depth,

while the Biot number of unity corresponds to the use of helium as the upper gas of the same thickness as the liquid. The relative importance of Rayleigh to Marangoni effects are given by the ratio $(Ra/Ma = \rho \alpha g H^2 / \sigma_1)$. This group is independent of the temperature difference and may be adjusted mainly by changing the depth of liquid or the gravitational level. It represents the importance of buoyancy or gravitational effects compared to surface tension gradient effects.

It is observed from Table 6 that, regardless of the value of Ra/Ma , the critical Ma are closely bunched for aspect ratios greater than 1.5. If one wishes to study the effect of side walls and also simulate a low-gravity environment by performing ground-based experiments, it is necessary to have very small depths and consequently very small diame-

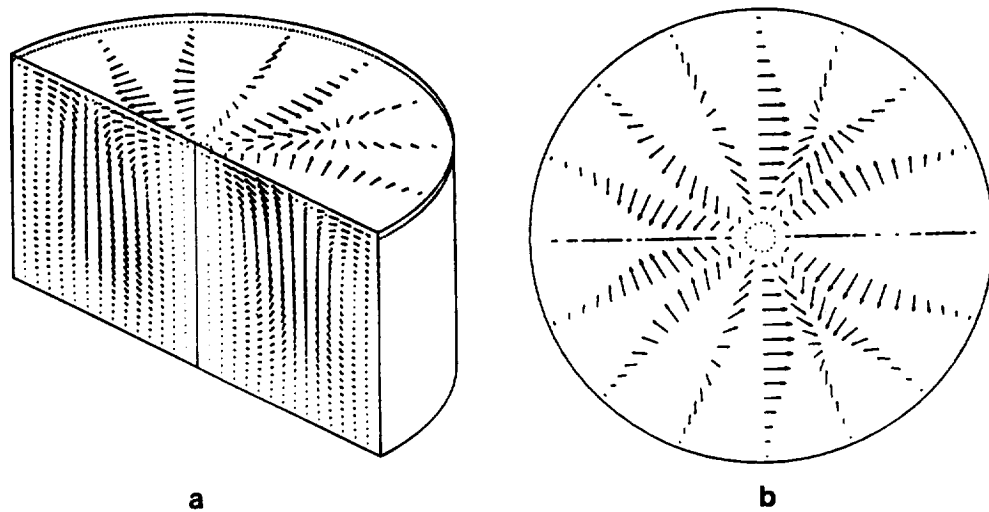


FIG. 7. Depiction of 3-D profiles and planforms of the velocity eigensolutions at $m = 3$ with $Ra = 308.43$, $Ma = 94.9$, and $A = 2.82$.

TABLE 6
Critical Marangoni Numbers for Various Ra/Ma, m , and Bi

Biot	Depth	Ra/Ma	m	Critical Marangoni numbers for						
				A = 0.5	A = 1.0	A = 1.5	A = 2.0	A = 2.5	A = 3.0	
1/7	1	0.1823	0	—	206.75	121.49	100.66	94.11	90.06	
			1	—	214.47	133.57	105.58	95.95	92.95	
			2	—	266.29	147.15	110.25	95.32	89.45	
			3	—	330.53	168.64	118.15	98.70	90.84	
	2	0.73	0	—	197.58	114.82	95.25	88.78	84.88	
			1	—	205.20	126.81	99.80	90.54	87.72	
			2	—	255.89	139.89	104.29	89.96	84.34	
			3	—	319.90	159.48	111.82	93.13	85.67	
	1	1	0.1823	0	—	247.10	153.38	132.12	125.61	120.50
				1	—	258.30	169.90	138.87	128.90	125.47
				2	—	308.66	180.84	141.44	125.85	119.79
				3	—	376.46	202.74	148.65	128.62	121.30
2		0.73	0	—	234.85	143.80	123.82	117.30	112.45	
			1	—	245.67	160.00	129.97	120.55	117.30	
			2	—	295.20	170.47	132.55	117.65	112.30	
			3	—	363.10	191.70	139.44	1120.33	113.22	
1/7	5	4.56	0	661.12	147.30	81.65	67.50	62.97	60.11	
			1	553.41	153.90	91.97	71.22	64.38	62.38	
			2	869.40	195.30	101.57	74.62	63.86	59.75	
			3	1104.44	253.67	117.87	80.10	66.27	60.70	

ters. Naturally this raises the issue of imperfections and moreover the small cell diameters make physical visualization of the flow difficult. On the other hand larger aspect ratios cause the clustering of eigenmodes and patterns and all of the issues raised earlier become relevant. It may also be seen from Table 6 that the general nature of our comments remain unchanged merely by changing the Biot number. Further it is observed from Table 6 that at aspect ratio 2.5 the most critical mode corresponds to $m = 0$ and at aspect ratio of 3 the most critical mode is $m = 2$. This means that a codimension 2 point occurs between aspect ratios 2.5 and 3. There is little doubt that such points are difficult to capture experimentally, once again because of the clustering of the bifurcation points or critical Ma. However, it is also observed from the calculation for a depth of 5 mm that another codimension 2 point (showing the switch between an $m = 1$ mode and an $m = 0$ mode) occurs between aspect ratios 0.5 and 1. Given these low aspect ratios it is conceivable that this multiple point can be captured in a careful experiment with reasonably deep layers.

From our calculations the following general statements may be made. First, narrow aspect ratio containers give rise to definite patterns at the onset of convection that are stable because the bifurcation points are not closely bunched. We expect that very large aspect ratio containers will simulate the infinitely wide case of classical theory, giving rise to hexagons as seen in earlier experiments. However the me-

dium aspect ratio containers (aspect ratios >3) will show spectral crowding and close branches. As it will be difficult to control the temperature differences accurately, it will be hard to get good agreement between theory and experiment at these intermediate aspect ratios. In other words it is better to conduct experiments either in very large geometries where end effects are negligible or in very narrow aspect ratio containers where spectral crowding is absent. While the medium aspect ratio containers could give theoretically predicted Marangoni numbers, the predicted patterns will be difficult to obtain experimentally because of the spectral crowding.

Second, experimental studies in narrow aspect ratio containers are best conducted in deep layers so that the radius of the containers may be large and side wall imperfections such as a mismatch in thermal conductivities and a "miniscus" may be minimized. Miniscus problems are likely to be encountered in narrow containers. In deep layers² Ra/Ma will be necessarily large and if we are to get predicted patterns in narrow aspect ratio containers, it will not be possible to bias the problem in favor of the Marangoni effect

² It is of course possible to choose a liquid with a very low density and thermal expansion coefficient; however, most experiments are conducted with silicone oils because of their nearly constant properties and clean interfaces. As a result Ra/Ma is typically large when the depths are greater than 2 mm.

and minimize the Rayleigh phenomenon. The effect of all of this is that in narrow aspect ratio containers convective instability experiments will invariably be buoyancy driven with a Marangoni perturbation and not the other way.

As a final note to readers of this journal we could take a look at this paper from a different perspective and use the calculations and companion experiments to predict the surface tension gradient ($\partial\sigma/\partial T$), provided that we have a good idea of the other thermophysical properties. In other words these bifurcation calculations are a good approximation to carefully controlled experiments and can be used for parameter identification.

SUMMARY

The critical conditions and patterns for the onset of three-dimensional convection in bounded circular containers were obtained. It was found that for a large range of aspect ratios the axisymmetric mode or $m = 0$ mode is the most unstable and that codimension 2 points occur for either large or somewhat small (< 1.0) aspect ratios. The comparison with existing experimental patterns is within reason but not exact and we have rationalized that this is possibly due to the effect of imperfections on geometries that encourage closely bunched eigenmodes. A reason for the apparent discrepancy between predicted and experimentally determined critical Ma is that the experimental results have assumed the correctness of the viscosity of the test fluid as stated by the manufacturer and we believe that the actual viscosity is substantially less. We believe that this is the major reason that might explain the difference in reported critical values of the experiment and those predicted by the theory. Calculations in deep layers and narrow containers show promise of future experimental verification.

APPENDIX

The solutions of Eqs. [1]–[5] were sought for the boundary conditions

$$\text{at } z = 0 \quad U = V = W = T = 0 \quad [\text{A1}]$$

$$\text{at } z = 1 \quad \frac{\partial U}{\partial z} + \frac{1}{A} \frac{\partial T}{\partial r} = \frac{\partial V}{\partial z} + \frac{1}{Ar} \frac{\partial T}{\partial \theta} = \frac{\partial T}{\partial z} + \text{Bi}T = 0 \quad [\text{A2}]$$

for perfectly insulating walls ($r = 1.0$)

$$U = V = W = \frac{1}{A} \frac{\partial T}{\partial r} = 0 \quad [\text{A3}]$$

and for perfectly conducting walls

$$U = V = W = T = 0. \quad [\text{A4}]$$

The basis functions for mode $m = 0$ are

$$X_j^0(r) = \frac{J_1(\alpha_j^0 r)}{J_1(\alpha_j^0)} - \frac{I_1(\alpha_j^0 r)}{I_1(\alpha_j^0)} \quad [\text{A5}]$$

$$Y_j^0(r) = 0 \quad [\text{A6}]$$

$$Z_j^0(r) = J_0(\delta_j^0 r), \quad [\text{A7}]$$

where I and J are Bessel functions of the first kind and α_j^0 and δ_j^0 are the roots of

$$J_2(\alpha_j^0)I_1(\alpha_j^0) + J_1(\alpha_j^0)I_2(\alpha_j^0) = 0 \quad [\text{A8}]$$

$$J_1(\delta_j^0) = 0 \quad [\text{A9}]$$

and

$$J_2(\alpha_j^0)I_1(\alpha_j^0) + J_1(\alpha_j^0)I_2(\alpha_j^0) = 0 \quad [\text{A10}]$$

$$J_0(\delta_j^0) = 0 \quad [\text{A11}]$$

for perfectly insulating and perfectly conducting side walls, respectively. For $m > 1$ the trial functions are

$$X_j^m(r) = \frac{J_m(\alpha_j^m r)}{J_m(\alpha_j^m)} - \frac{I_m(\alpha_j^m r)}{I_m(\alpha_j^m)} \quad [\text{A12}]$$

$$Y_j^m(r) = J_m(\beta_j^m r) \quad [\text{A13}]$$

$$Z_j^m(r) = J_m(\delta_j^m r), \quad [\text{A14}]$$

where α_j^m , β_j^m , and δ_j^m are the roots of

$$J_{m+1}(\alpha_j^m)I_m(\alpha_j^m) + J_m(\alpha_j^m)I_{m+1}(\alpha_j^m) = 0 \quad [\text{A15}]$$

$$J_m(\beta_j^m) = 0 \quad [\text{A16}]$$

$$J_{m-1}(\delta_j^m) - J_{m+1}(\delta_j^m) = 0 \quad [\text{A17}]$$

and

$$J_{m+1}(\alpha_j^m)I_m(\alpha_j^m) + J_m(\alpha_j^m)I_{m+1}(\alpha_j^m) = 0 \quad [\text{A18}]$$

$$J_m(\beta_j^m) = 0 \quad [\text{A19}]$$

$$J_m(\delta_j^m) = 0 \quad [\text{A20}]$$

for perfectly insulating and perfectly conducting side walls, respectively.

As noted in the main text of this paper Eqs. [13]–[15] were substituted into the governing equations. The pressure was then eliminated and equations of fourth order resulted. On using the Galerkin method many integrals result from making the residuals equal to zero. An example is

$$[\text{integral}]_{k_j} = \int_0^1 r \left[D_r^4 + \frac{2}{r} D_r^3 - \frac{(3+m^2)}{r^2} D_r^2 + \frac{(3+m^2)}{r^3} D_r - \frac{(3-3m^2)}{r^4} \right] X_j X_k dr. \quad [\text{A21}]$$

When $m = 0$, [A5] to [A7] were used and when $m = 2, 3$, etc., [A12] to [A17] were used. However, when $m = 1$ this and several other integrals gave rise to singularities at $r = 0$. There are at least two ways to get over this problem. One way is to look at the geometry of the problem as a limiting case of an annular compartment with a very small inner cylinder and thereby exclude $r = 0$ from the domain. Another way is to choose the $m = 2$ spectral functions in order to express the flow pattern at $m = 1$. This is legitimate as the eigenfunctions are complete. We chose to do the latter and note that Chen *et al.* (10) indicated that [A12] to [A14] with $m = 1$ were used in their calculations. As this leads to singular behavior, this may be one reason why there is a difference between our results and Chen *et al.* (10).

ACKNOWLEDGMENTS

Support from NSF Grant CTS 93 07819 and part support from NASA 1-1474 is gratefully acknowledged. The computations were performed on the Cray C-90 at the Pittsburgh Supercomputing Center.

REFERENCES

1. Bénard, H., *Rev. Gén. Sci. Pure Appl.* 11 (1900).
2. Pearson, J. R. A., *J. Fluid Mech.* 4, 489 (1958).
3. Koschmieder, E. L., "Bénard Cells and Taylor Vortices," Cambridge Univ. Press, Cambridge, UK, 1993.
4. Koschmieder, E. L., and Pohl, S. A., *J. Fluid Mech.* 251, 571 (1990).
5. Vrentas, J. S., Narayanan, R., and Agrawal, S. S., *Int. J. Heat Mass Transfer* 24(9), 1513 (1981).
6. Winters, K. H., Plesser, T., and Cliffe, K. A., *Physica D* 29, 387 (1988).
7. Dijkstra, H. A., *J. Fluid Mech.* 243, 73 (1992).
8. Duh, J. C., "IKI/AIAA Microgravity Science Symposium Proceedings, 1991."
9. Van der Vooren, A. I., and Dijkstra, H. A., *Comput. Fluids* 17(3), 467 (1989).
10. Chen, J.-C., Chen, J.-Y., and Hong, Z.-C., "Congress of the International Astronautical Federation, Montreal, Oct. 1991," Vol. 42, Paper IAF 91-393.
11. Nield, D. A., *J. Fluid Mech.* 19, 341 (1964).
12. Wagner, C., Friedrich, R., and Narayanan, R., *Phys. Fluids* 6(4), 1425 (1994).
13. Rosenblat, S., Davis, S. H., and Homsy, G., *J. Fluid Mech.* 120, 91 (1982).
14. Rosenblat, S., Davis, S. H., and Homsy, G., *J. Fluid Mech.* 120, 123 (1982).
15. McTaggart, C. L., *J. Fluid Mech.* 134, 301 (1983).
16. Dijkstra, H. A., *Micrograv. Sci. Technol.* VII 4, 307 (1995).
17. Zhao, A. X., Wagner, C., Narayanan, R., and Friedrich, R., *Proc. R. Soc. A* 451, 487 (1995).
18. Hardin G. R., Sani, R. L., Henry, D., and Roux, B., *Int. J. Num. Meth. Fluids* 10 (1990).
19. Vidal, A., and Acrivos, A., *Phys. Fluids* 9(3), 615 (1966).
20. Takashima, M., *J. Phys. Soc. Jpn.* 50(8), 2745 (1981).
21. Zhao, A. X., Moates, C., and Narayanan, R., *Phys. Fluids* 7(7), 1576 (1995).
22. Tavantzis, J., Reiss, E.L., and Matkowsky, B. J., *SIAM J. Appl. Math.* 34(2), 322 (1978).
23. Matkowsky, B. J., and Reiss, E. L., *SIAM J. Appl. Math.* 33, 230 (1977).



A 3D NUMERICAL MODEL FOR FLOW PROFILES IN A BRIDGMAN TUBE --THE EFFECTS OF CONSTANT AND PERIODIC OFF AXIS ORIENTATION IN A LOW GRAVITY ENVIRONMENT

A. X. Zhao¹, R. Narayanan¹ and A. L. Fripp²

¹Department of Chemical Engineering, University of Florida, Gainesville, FL 32611

²NASA Langley Research Center Hampton, VA 23665

ABSTRACT:

A 3D numerical calculation is performed on a model that depicts the flow profiles due to thermo-solutal convection in a cylindrical tube. The calculations were done with the purpose of delineating the qualitative features of the flow profiles for the cases when the container's axis is perfectly aligned with respect to the mean gravity vector and also when it changes periodically with respect to the gravity vector. It is found that the flow profiles are similar to those of the Rayleigh-Bénard problem in the case of perfect alignment while a swirling pattern appears when the tube's axis is not aligned with the gravity vector. This indicates that it might be preferable to have a slight tilt in the container axis during crystal growth as swirling flow will diminish axial mixing. The solutal convection is the dominant feature of the flow and is affected considerably by the gravity level.

© 1999 COSPAR. Published by Elsevier Science Ltd.

INTRODUCTION

This is a brief report describing the flow profiles that are induced in a low gravity environment in a Bridgman tube in which the fluid occupies a constant volume. The Bridgman tube as considered in this study is merely a circular cylinder that is subjected to radial thermal gradients and axial solutal gradients. Typically, the Bridgman tube is used in the vertical directional solidification of compound semi conductors such as Lead Tin Telluride. The growth of such materials is affected substantially by the convective flow profiles that accompany the process. This convection is due to thermal and solutal gradients that are generated because of the solidification process. Arnold *et. al.* (1991) did calculations to model a GaAs space experiment and concluded that three-dimensional flows occur under certain gravitational values and orientations. Their calculations were not concerned with solutal convection. Naumann and Baugher (1992) have made analytical estimates of radial segregation in Bridgman growth for low-level steady and periodic accelerations. In any actual growth process, the liquid zone is ever shrinking and this can be expected to change the flow profiles quite a bit. Nonetheless it would be interesting to have an idea of the flow profiles that are generated when the force conditions on the ampoule are compatible to a time dependent microgravity level and where certain assumptions such as a constant liquid zone is assumed. We present here a numerical model that shows the effects of off axis and a time dependent orientation on the flow profiles in a Bridgman tube. The effect of tilting the otherwise vertical container with respect to gravity is also

described. The calculations were done with the purpose of delineating the *qualitative* features of the flow profiles for the cases when the container's axis is perfectly aligned with respect to the mean gravity vector and also when its axis periodically changes with respect to the gravity vector. The gravitational levels that are assumed range from $10^{-5}g_e$ (or ten micro g) to $10^{-4}g_e$ where g_e is earth's gravity. A value of ten micro g is reasonable as it is a fair representation of the low frequency accelerations experienced on the cargo bay of the U.S. space shuttle or on the future international space station if the Bridgman tube. A level of 100 micro g is not very probable, however we also present calculations that include this extreme case. To the best of our knowledge this is the only study that shows the dominant effect of solutal convection over thermal convection at the higher gravity levels and also the only study where the ampoule axis orientation is varied with time.

Table 1 The Thermophysical Properties Used in the Calculations

Density	7.04 g/cm^3
Kinematic Viscosity	$0.0024 \text{ cm}^2/\text{s}$
Thermal Diffusivity	$0.03 \text{ cm}^2/\text{s}$
Solutal Diffusivity	$7 \cdot 10^{-5} \text{ cm}^2/\text{s}$
Thermal Expansion Coefficient	$1.18 \cdot 10^{-4} / \text{C}^\circ$
Solutal Expansion Coefficient	0.22 /Weight fraction
Segregation Coefficient	0.7

THE MODEL AND THE NUMERICAL SCHEME

The model that is used assumes that the Boussinesq equations hold. Further the calculations were done assuming that the fluid is Lead Tin Telluride reflecting our interest in compound semiconductors. The thermophysical properties of Lead Tin Telluride as used in the calculation are given in Table 1. Figure 1 describes the situation when a container is subject to thermal gradients with a solidifying interface at $z=H-H_{\text{solid}}$. The thermal and concentration boundary conditions imposed on the container are given in Figure 1. No-slip conditions are used at all boundaries including the solid-liquid interface upon which the coordinate system is fixed and which is assumed to move down in the z direction at a constant speed V_s equal to 1 cm/hr. The height of the tube of diameter equal to 1. cm. is given by H and assumed to be 5.0 cm., equally divided between the solid and liquid zones while the insulation zone is assumed to occupy the middle one third. These correspond roughly to the experimental ampoule used in a Lead Tin Telluride experiment that was conducted on USMP 3. The hottest temperature is assumed to be 1150 degrees Celsius while the coldest temperature is fixed to be 700 degrees, the interface being at 900 degrees. The orientation of the gravitational acceleration is expressed in terms of the angle between the gravity and the negative direction of the z -axis. The major assumption is that the liquid length is kept constant. As a result it is assumed that the end of the liquid was at a constant concentration, C_0 equal to 0.2 weight fraction. This is tantamount to a continuous feeding of such liquid at the solidification rate V_s . Before we go on it might be useful to point out that the thermal Rayleigh number is estimated to be about 65 for a gravity level $10^{-4}g_e$ while the solutal Rayleigh using the same length scale is about 147000

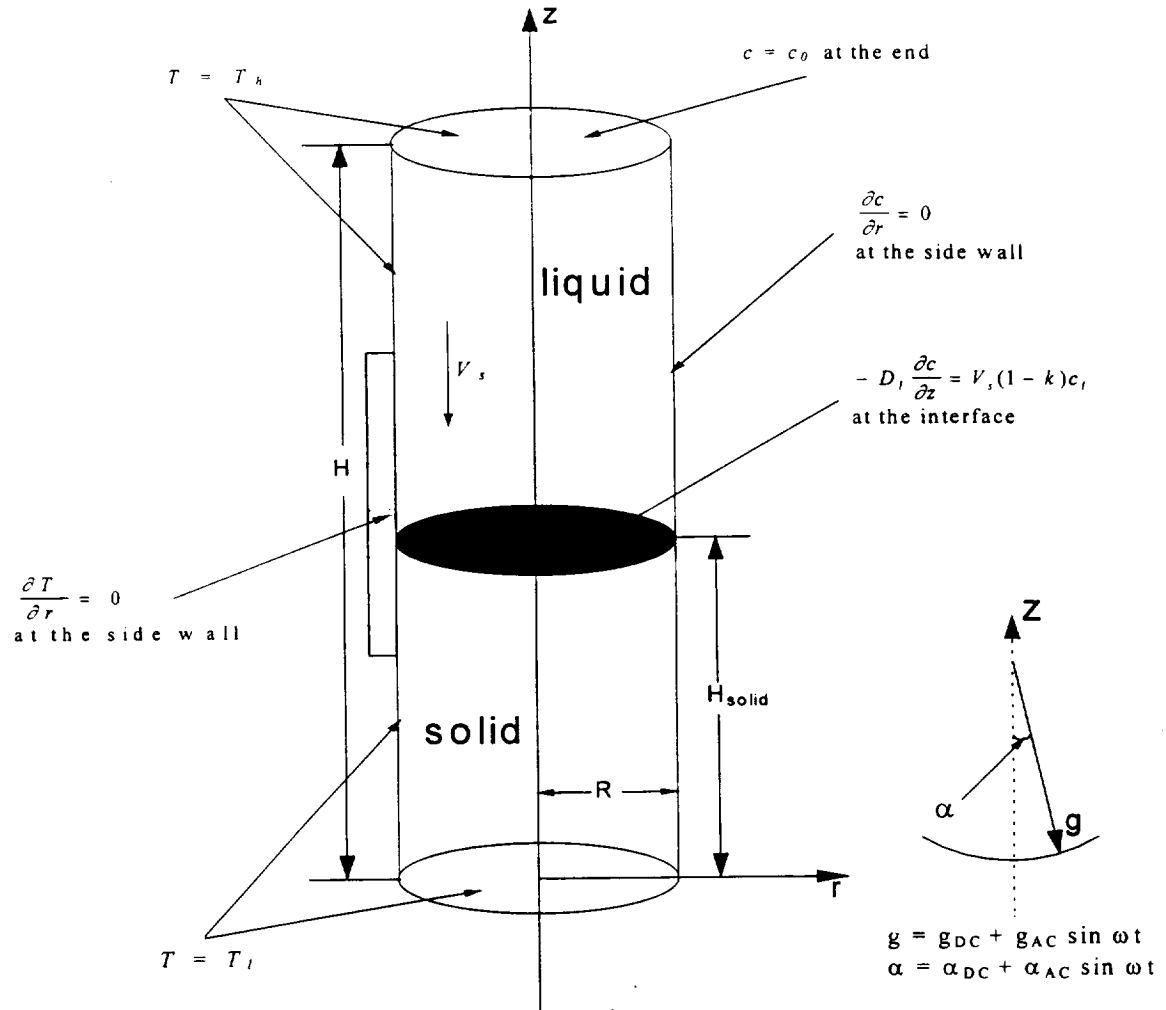


Fig. 1 The schematic of the geometry and thermal and concentration boundary conditions of the calculation.

RESULTS OF THE CALCULATIONS AND CONCLUSIONS

The finite volume method, SIMPLE (cf. Patankar, 1980) was chosen to solve the governing equations. Figure 2 shows the flow profiles at two different gravity levels. Figure 2a describes the pattern that is expected at a constant g level of $10^{-5}g_e$. What is to be observed is vertical stacking of an axisymmetric or torroidal pattern. This vertical stacking may be expected as the top of the ampoule is hotter than the bottom and the lower 'cell' is in the insulation zone. The configuration acts like a fluid that is 'heated from above' and the weak flow is primarily driven by radial gradients. The weakness in the lower cell is primarily due to the effect of the presence of the 'no slip' solid boundary.

The situation changes somewhat for the case of a g level of $10^{-4}g_e$ as seen in Figure 2b, for here the solutal convection begins to play a part. The solutal gradients are unstable in the sense that they promote flow even if the thermal expansion coefficient is negligible. As observed earlier the solutal Rayleigh number is about 147000 whereas the critical solutal Rayleigh number, in the absence of thermal gradients for this aspect ratio

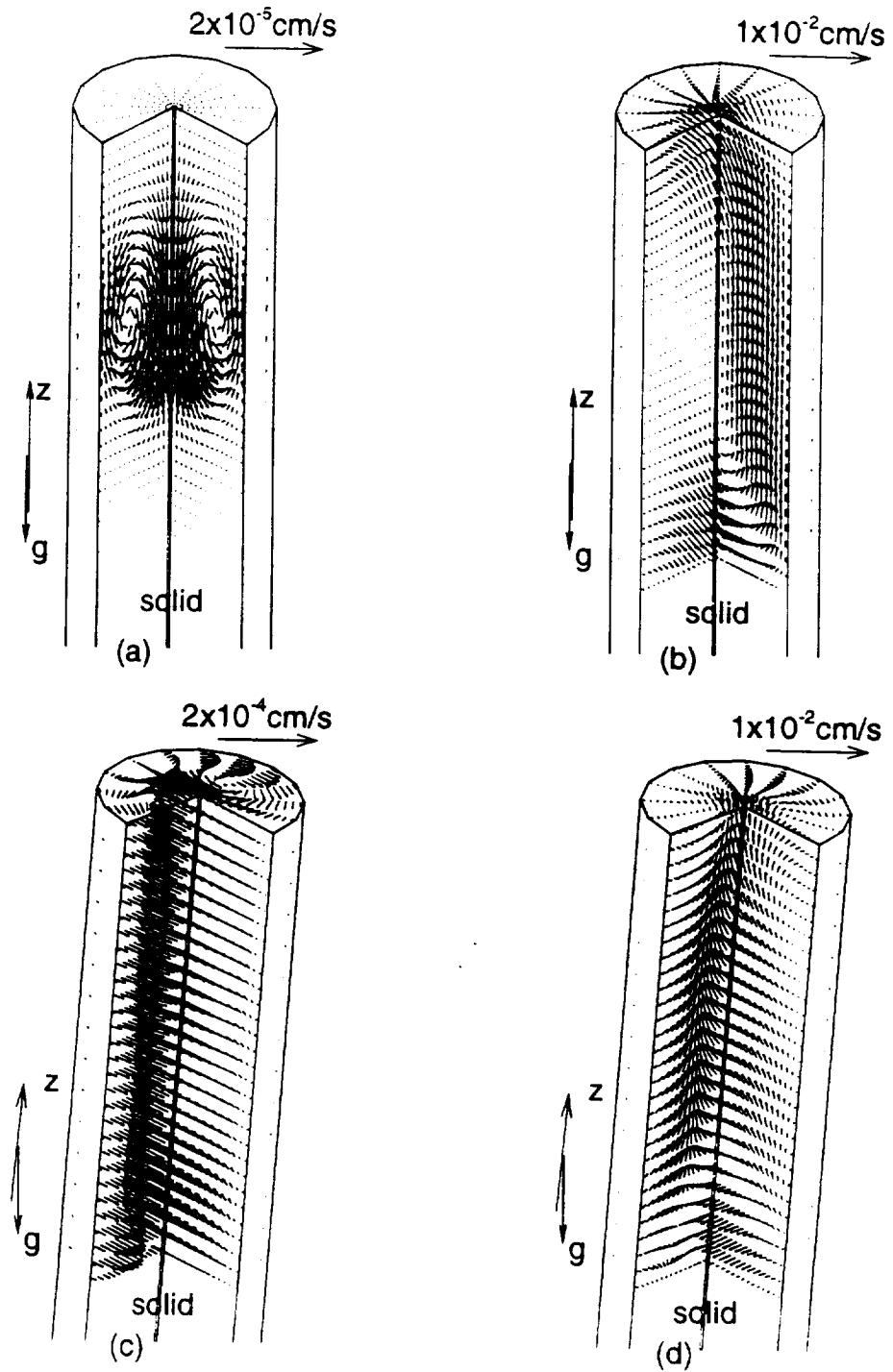


Fig.2. The 3D flow field in the liquid region with constant 'g' and fixed orientation.
 (a) $10^{-5} g_e$, $\alpha = 0^\circ$; (b) $10^{-4} g_e$, $\alpha = 0^\circ$; (c) $10^{-3} g_e$, $\alpha = 5^\circ$; (d) $10^{-4} g_e$, $\alpha = 5^\circ$.

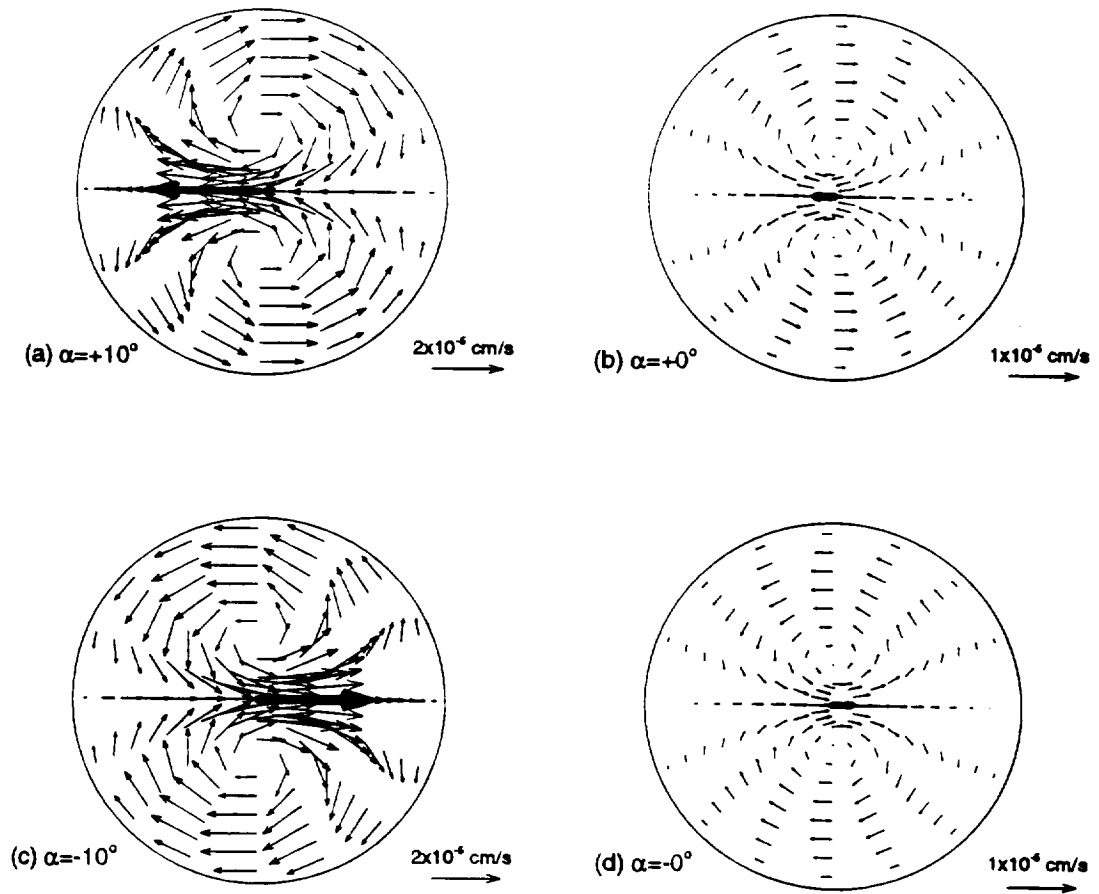


Fig.3. The 2D flow field near the interface under $10^{-5} g_e$. The orientation of the gravity vector is a function of time ($\alpha = 10^\circ \sin \omega t$, $\omega = 2\pi/3600$).

(radius/ height =0.2) turns out to be about 50000 from the calculations of Hardin *et. al.*. The unicellular patterns that are observed are a result of the solutally driven convection and are expected for this geometry according to the results of the Rayleigh-Bénard problem (cf. Hardin *et.al.*, 1990). Notice further that the vertical stacking arrangement disappeared for the larger 'g' level indicating the dominance of the solutal convection over the thermal convection. Figure 2c shows the flow profiles resulting from a time invariant change of the ampoule axis with respect to the mean gravity vector of $10^{-5}g$. What is immediately apparent is the swirling flow that helps contain the rejected solute near the solid liquid interface. The 'z' component of this type of flow is much smaller than the other two components except near the interface and the end of the liquid where all components are set to zero on account of no-slip. It is a concentration induced flow because the velocity components near the interface in Figure 2c are much larger than in Figure 2a. In a real crystal growth configuration such an off axis tilt would help prevent axial mixing and therefore be beneficial to the crystal. If the 'g'- value is increased by an order of magnitude the flow is mostly of a unicellular style except near the interface. This is shown in Figure 2d. Figure 3 depicts the periodic change of the cylinder axis with the gravity vector. The frequency was set to be one cycle per hour. This was an arbitrary choice even though aerodynamic drag causes a readjustment every 20 minutes or so in a typical space orbiter. All the same the results can be expected to be qualitatively similar to those reported here in the case when the frequency is increased three fold. The flow profiles at a constant 'z' plane near the solid liquid interface are given at every quarter cycle, once a periodic steady state is reached. Notice that the direction of the swirl changes every half cycle i.e., when the gravity vector crosses the cylinder axis leading to local mixing near the solid liquid interface.

The effect of gravity level and time periodic off axis alignment show collectively that the convection at low gravity in a bottom or top seeded Bridgman tube is primarily in the solutal driven mode as long as the gravity level is not very small. Moreover a slight tilt with respect to gravity causes the fluid flow to go into a swirling mode so that solute is contained near the solute-generating boundary.

ACKNOWLEDGMENT

We acknowledge NASA for supporting this work under Grant No. NAG-1-1474 and NAG 8 1243 as well as the Florida Space Grant Consortium. The computations were performed on the CRAY/C90 under the NASA National Aerodynamics Simulation (NAS) Program.

REFERENCES

- Arnold, W.A, Jacqmin, D.A., Gaug, R.L., and Chait, A. Three-Dimensional Flow Transport Modes in Directional Solidification During Space Processing, *J. Spacecraft*, 28, pp.238-243 (1991)
- Hardin, G.R., Sani, R.L., Henry, D. & Roux, B., Buoyancy-Driven Instability in a Vertical Cylinder: Binary Fluids with Soret Effect. Part I: General Theory and Stationary Stability Results, *Int. J. Num Meth. Fluids* 10,79 (1990)
- Naumann R.J., and Baugher, C., Analytical Estimates of Radial Segregation in Bridgman Growth from Low-level Steady and Periodic Accelerations, *J. Crystal Growth*, 121, pp.751-768 (1992)
- Patankar, S.V., Numerical Heat Transfer and Fluid Flow, *Taylor and Francis*, Washington, DC (1980)

Bilayer Rayleigh–Marangoni convection: transitions in flow structures at the interface

BY ALEX X. ZHAO¹, CLAUS WAGNER², RANGA NARAYANAN¹ AND
RAINER FRIEDRICH²

¹*Department of Chemical Engineering, University of Florida,
Gainesville, FL 32611, USA*

²*Lehrstuhl für Strömungsmechanik, T.U. München, Arcisstrasse 21,
D8000 München 40, Germany*

The fluid physics of buoyancy-driven (Rayleigh) and interfacial tension-driven (Marangoni) convection is examined for two superimposed layers of fluids. This convection occurs on account of temperature gradients that are imposed perpendicular to the fluid–fluid interface. Interfacial deflections, small as they may be, play an important part in identifying the mechanism that governs the flow, and calculations have been made that indicate whether hot or cold fluid flows towards or away from a crest or a trough. As a result, four possible flow structures or ‘modes’ at the interface have been identified. Two heating styles, heating from below and above, are compared and the behaviour of the fluid physics as a function of total fluid depths, depth ratios and gravity levels is explained. Changes in modes result because of changes in these parameters. We have given plausible physically based arguments that predict the sequential change in modes as these parameters are changed and have ‘verified’ our conjectures with calculations. Flow mechanisms in the case of a solidifying lower phase have also been studied, as this has an application to liquid-encapsulated crystal growth. Where convection is deemed detrimental to crystal homogeneity, we conclude that the liquid-encapsulated method of crystal growth is best conducted under Earth’s gravity.

1. Introduction

This paper is concerned with the study of convection in fluid bilayers. Interfacial-driven convection must necessarily involve at least two fluid layers and we could well imagine that the fluid physics of motion, driven by interfacial tension and density gradients, depends largely on the heating direction, fluid depths as well as property ratios. One motivation for this study stems from an interest in liquid-encapsulated crystal growth where a vertical cylinder with thermally insulated side walls encloses the melt. The crystal solid phase can be below the melt phase and this corresponds to the bottom seeding situation where the liquid melt is now heated from above. An encapsulant is often placed above the melt in order to provide a diffusion barrier to high volatile constituents in the melt. An example is the growth of gallium arsenide, wherein arsenic is the highly volatile component and boron oxide the encapsulant. A bilayer with a common interface is thereby created. As a temperature gradient is applied across the interface, there are basically two mechanisms which can generate

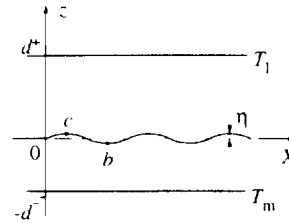


Figure 1. Schematic of the bilayer system. Dashed line is the flat interface in the quiescent state.

convection, i.e. buoyancy and interfacial tension gradients. These two mechanisms are called Rayleigh and Marangoni effects, respectively. In a model problem we could apply a temperature gradient that is either parallel or antiparallel to the gravitational field and the configuration represents an instability problem which is associated with a bifurcation from the quiescent state to the convective state. By applying a linear stability theory, we get the sufficient conditions for the onset of convection as well as the most dangerous wavelength of an imposed infinitesimal disturbance.

We can understand the physical mechanisms which are involved in interfacial tension gradient convection by considering a bilayer configuration, as shown in figure 1. Let $T_1 > T_m$ and further assume that gravitational effects are negligible. Now suppose we give a perturbation to an erstwhile flat interface so that the temperature at the point 'c' is higher than at 'b'. As most fluid bilayers have a negative interfacial tension gradient, the interfacial tension at 'c' will be lower than at 'b' and fluid is driven from 'c' to 'b'. Fluid from both phases must then rush towards 'c' and the final steady state will depend on the fluid property ratios and heights. If we have a liquid-gas system where the upper gas phase is assumed to be passive, then only liquid from below will move towards 'c' and it follows that unless the temperature gradient is reversed, the perturbations must decay. Gravity stabilizes or not according to the heating arrangement. It may be pointed out that the mechanism for flow can take place even if the interface is always restricted to be flat because temperature perturbations are still allowed. However, our interest will mainly focus on the general case where interfacial deformations are included.

2. Earlier work on bilayer convection

The first theoretical work in Marangoni convection was by Pearson (1958), wherein the liquid layer was assumed to be superimposed by a quiescent gas. One of the early studies in bilayers was by Sternling & Scriven (1959), who considered the pure Marangoni problem using mass transfer as an analogue to heat transfer, and Smith (1966), who examined the case of thermocapillary and gravity waves. Sternling & Scriven found that convection or instability can occur if the transfer takes place in either direction. This problem was later extended to include surface deflection and surface viscosity, but it was then assumed that the upper phase was passive.

This work was followed by Zeren & Reynolds (1972), who determined the critical temperature gradient for the onset of convection in a bilayer of water and benzene in order to compare theory with experiment. Now, in dimensionless form, the critical temperature gradient is represented by either the Marangoni or the Rayleigh number. As these groups are related to each other by a factor that contains physical properties, it is sufficient to calculate either the critical Rayleigh or critical Marangoni number

for the onset of convection. When the bilayer was 'heated from below', Zeren & Reynolds (1972) found that the onset of convection was either a buoyancy-driven flow generated from the upper phase or an interfacial tension gradient-driven flow that started at the interface. When they considered the case of a low liquid layer depth of the lower layer compared with the thickness of the upper layer, they found that the Marangoni convection in the bilayer served to delay the onset of motion and that the flow was primarily a buoyancy mechanism which was driven from the upper layer. This resulted in vertical stacking in the upper layer where the upper cell in the upper layer was associated with the buoyancy mechanism. On the other hand, when high depth ratios of the lower phase were considered, the onset of flow was due primarily to a Marangoni mechanism and not influenced much by the Rayleigh effect.

Following the work of Zeren & Reynolds (1972), Ferm & Wollkind (1982) performed detailed calculations for the silicone oil-air system with the hope of comparing their results with the experiments of Koschmieder (1967) and Palmer & Berg (1971). All calculations were performed for the case of the bilayer being 'heated from below'. In an effort to trace where the Marangoni regime was distinct from the Rayleigh regime, a series of calculations were performed and plotted as the critical temperature gradient against the depth of lower layer. They claimed that a drastic change in slope of this curve indicated the depth ratio of the lower layer when one mechanism took over the other.

Recent work on bilayer convection includes the interesting studies of Rasenat *et al.* (1989) and Wahal & Bose (1988). Rasenat *et al.* (1989) investigated the case of negligible surface deflections and uncovered oscillatory behaviour. They also considered a case of finite interfacial deflections but with negligible interfacial tension. While it may be argued that interfacial deflections are very small in comparison to the fluid depths, it is our view that the interfacial morphology helps to identify the controlling factors of competing convective mechanisms. This is what we aim to show in the subsequent sections.

It is noted that Zeren & Reynolds (1972) calculated the energy contributions from the buoyancy and surface mechanisms, as well as the critical Rayleigh and corresponding Marangoni numbers, in an effort to trace the leading characteristics of the flow. It is obvious that the energetics of the flow are calculated across the entire domain of the flow field and give some useful global information. However, it is also possible to consider the local behaviour of the flow at the interface using linear stability methods and by evaluating the eigenfunctions. We feel that this leads to vital information on the flow mechanism at the interface. In particular, we can, as we shall see, decide whether we have hot or cold fluid rushing towards or from a crest or a trough. We will observe that we can have four possible flow modes at the interface. This paper concerns operating parameters and, as we change the gravity level, the total depth or depth ratio, a sequential change of flow structures is obtained. The generality of this sequence depends on whether we have a liquid-gas system, a liquid-liquid system and whether the bilayer is 'heated from below or above'. The order of flow structures as we change these parameters also depends on whether the temperature coefficients of interfacial tension and density are negative or positive. From this we can decide whether the flow mode at the interface is promoted by Rayleigh or Marangoni effects.

3. Theoretical development

The model that we analyse is schematically shown in figure 1. The governing equations are derived in a manner identical to that of Ferm & Wollkind (1982) and so we dispense with the intermediate details in the cause of brevity. Without loss of generality, we introduce a two-dimensional coordinate system. In this system, the direction of the gravitational acceleration corresponds to the negative z -direction. The position of the deflecting interface is a function of x and the time t and is measured from the datum $z = 0$. The upper fluid is designated with $+$ and the lower fluid with $-$, so that d^+ represents the vertical depth of the upper fluid and d^- the depth of the lower fluid. The lower solid-liquid boundary has a constant temperature T_m and the upper solid surface has a temperature of T_1 , respectively. The static interface has a temperature of T_i . We will use the Boussinesq form of the continuity, Navier-Stokes and energy equations.

In order to get non-dimensionalized forms of the above equations, we introduce the scale factors for distance, velocity, time and pressure. These are d^- , κ/d^- , $(d^-)^2/\kappa$ and $\mu\kappa/(d^-)^2$, respectively. κ and μ are the thermal diffusivity and dynamic viscosity of the lower phase, respectively.

The dimensionless temperature Θ is defined as

$$\Theta = \frac{(T - T_i)}{(T_m - T_i)}. \quad (3.1)$$

In what follows, several important dimensionless groups will arise. These are the Rayleigh number R , Marangoni number M , Cripsation number C , the Bond number G and Prandtl number P . They are defined as follows:

$$R = \frac{g\alpha\beta d^4}{\kappa\nu}, \quad M = \frac{\sigma_1\beta d^2}{\kappa\mu}, \quad C = \frac{\mu\kappa}{\sigma_0 d}, \quad G = \frac{\Delta\rho g d^2}{\sigma_0}, \quad P = \frac{\nu}{\kappa}.$$

All the physical properties in these numbers are referred to the lower phase. Here α is the negative thermal expansion coefficient, β is the temperature gradient in the static state, ν is the kinematic viscosity, $\Delta\rho$ (i.e. $\rho^- - \rho^+$) is assumed to be positive, thereby excluding the Rayleigh Taylor instability, g is the gravitational constant, σ_0 and σ_1 are the interfacial tension and its temperature coefficient, respectively.

The governing equations are nonlinear and admit the conductive quiescent state as a trivial solution. We linearize the equations about the trivial base state, eliminating all of the dependent variables in favour of the vertical component of velocity and temperature. Linearization of a dependent variable \mathbf{A} gives

$$\mathbf{A} = \mathbf{A}_c + \epsilon \mathbf{A}' + O(\epsilon^2), \quad (3.2)$$

where \mathbf{A}_c is the quiescent state and ϵ is a deviation from this state. \mathbf{A}' is further decomposed as

$$\mathbf{A}' = \mathbf{A}_0(z) e^{qt} e^{i\omega x}. \quad (3.3)$$

This means that a Fourier transform in the x -direction and a Laplace transform in time has been used. The dependent variables are the transformed temperature Θ_0 , the transformed vertical component of velocity W_0 and the transformed interfacial deflection η_0 . We get the momentum and energy equations for the upper phase as

$$\frac{q}{P}(D^2 - \omega^2)W_0^+ = \frac{s}{r}(D^2 - \omega^2)^2W_0^+ - aR\omega^2\Theta_0^+, \quad (3.4)$$

$$n(D^2 - \omega^2)\theta_0^+ = q\theta_0^+ - \frac{W_0^+}{m}. \tag{3.5}$$

Here, D represents the total derivative with respect to z . r, s, a, n and m are the density, kinematic viscosity, thermal expansion coefficient, thermal diffusivity and thermal conductivity ratios, respectively. These ratios are all referred to the lower phase properties as characteristic variables. The corresponding forms for the lower fluid are the same as the above equations with the '+' superscript replaced by the '-' superscript, and also with r, s, a, n and m replaced by unity. It is clear, by eliminating either dependent variable in favour of the other, that each phase is governed by a sixth-order ODE in either the temperature or vertical component of velocity. The boundary conditions are also transformed. For the sake of brevity we only give the interfacial conditions here. The kinematic, no slip and momentum equations at the interface are

$$W_0^+ = q\eta_0 = W_0^-, \tag{3.6}$$

$$[DW_0]_{\pm}^{\pm} = 0, \tag{3.7}$$

$$\left[\frac{q}{P}K[r]DW_0 - K[s](D^2 - \omega^2)DW_0 + 2K[s]\omega^2DW_0 \right]_{-}^{+} = (RC + G + \omega^2)\frac{\omega^2}{C}\eta_0, \tag{3.8}$$

$$[-K[s](D^2 + \omega^2)W_0]_{-}^{+} = M\omega^2(\eta_0 - \theta_0^-). \tag{3.9}$$

The continuity of temperature and heat flux at the interface are

$$[\theta_0 - K[1/m]\eta_0]_{-}^{+} = 0, \tag{3.10}$$

$$[K[m]D\theta_0]_{-}^{+} = 0. \tag{3.11}$$

$K[m]$ represents an operator that takes the value of m in the upper phase and unity in the lower phase.

The above system represents an eigenvalue problem and has 10 dimensionless groups as parameters. It is sensible to concentrate on a particular system, fix the values of all the parameters and determine the critical condition of onset. As the Rayleigh number is related to the Marangoni number by a factor made up of physical properties, we can get the critical temperature gradient and critical wavelength of the disturbance for the chosen system.

The sign of the quantity $DW_0(0)/\eta_0$, called a flow indicator (cf. Smith 1966), tells us whether we have upflow or downflow at a crest. If it is positive, we have downflow at a crest. The quantity $(\theta - \theta_c)_I/\eta$, which is of $O(\varepsilon^2)$ and equal to θ_0/η_0 , is a temperature perturbation indicator and tells us that we have a hot spot at the crest if it is positive. Here $(\theta - \theta_c)_I$ is the dimensionless temperature perturbation at the interface. It is clear that there are four possible 'flow modes' or 'scenarios' and these words will be used interchangeably. These are depicted in figure 2 and assigned Roman numerals. The discussion of the numerical results will centre on these flow scenarios and the sequence of flow mode changes as we change the gravity level, the total depth d_t and the depth ratio $\ell (\equiv d^+/d^-)$. The eigenfunctions $W_0^+(z)$ and $W_0^-(z)$ are also calculated and we can observe if there are any zeros in the z -direction. This will indicate if there is a vertical stacking of flow cells in either phase. The discussion of the physics assumes that $q = 0$ or the exchange of stability. By applying a spectral- τ method, it was shown that $\text{Im}(q) = 0$ when $\text{Re}(q) = 0$ in the cases studied.

The reliability of the numerical procedure was tested by recovering the results of

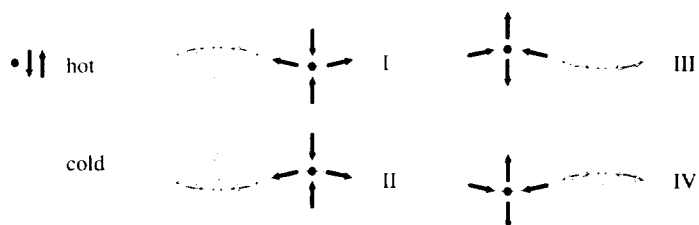


Figure 2. Four flow modes at the fluid-fluid interface. When the interface is flat, there is no difference between mode I and II, or mode III and IV.

Table 1. *Physical properties of fluids*

parameter (units)	Dow Corning oil		air above water or D.C. oil	water		benzene above water	gallium under D.C. oil
	under air	above gallium		under benzene (16 °C)	under air (0+ °C)		
density (g cm ³)	0.968	0.968	0.0012	0.998	0.999	0.884	6.09
negative thermal expansion coefficient (×10 ⁻⁴ °C)	9.6	9.6	34.0	2.06	-0.68	14.5	1.0
thermal conductivity (×10 ⁴ erg cm ⁻¹ s ⁻¹ °C ⁻¹)	1.55	1.55	0.26	5.97	5.97	1.64	334.0
thermal diffusivity (×10 ⁻³ cm ² s ⁻¹)	1.1	1.1	160	1.43	1.43	1.04	146.0
kinematic viscosity (stoke)	1.0	0.05	0.152	0.01	0.01	0.0067	0.003 54
interfacial tension (dyne cm ⁻¹)	20.9	—	—	32.8	74.9	—	718.0
negative interfacial tension gradient (×10 ⁻² dyne cm ⁻¹ °C)	5.8	—	—	5.66	14.0	—	38.89

Zeren & Reynolds (1972) and Ferm & Wollkind (1982). Table 1 contains the fluid properties used in our calculations. The results for the silicone oil-air system agree with those of Ferm & Wollkind (1982) (within the round-off error). The comparison for the water-benzene bilayer shows good agreement with the values of Zeren & Reynolds (1972). We note that Renardy & Joseph (1985) and Wahal & Bose (1988) have independently verified these latter results.

4. Discussion of the numerical results

As we have used a linearized model, the calculations can only give information about the flow state at the onset of convection. The discussion is divided into several parts, each referring to the physical situation on hand. These are: (*a*) a liquid–gas case, as exemplified by the silicone oil–air system; (*b*) a liquid–liquid case, as depicted by the water–benzene system; (*c*) a case of two liquids in the presence of solidification, which is depicted by the gallium–silicone oil system with a solidifying gallium phase below; and (*d*) the situation that arises when the temperature coefficient of density is positive, as exemplified in the water–air system with the temperature range of water between 0 and 4°C. As noted by Chandra & Holland (1983), there are some commercially important liquid semiconductors, such as mercury cadmium telluride, with positive temperature coefficients of density. It is clear from the choice of systems, where the upper layer is less dense than the lower layer, that the Rayleigh–Taylor instability will be excluded from this study. Moreover, as neither phase is in motion in the base state, the Kelvin–Helmholtz instability is also excluded.

For a chosen system, the only control parameters in experiments are the total depths, depth ratio and gravity level. The critical temperature difference and critical wavelength at the onset are results that come from the linearized stability calculation. Before we discuss the results any further, we will clarify the roles of gravity, total depth and the parameter ℓ . The lowering of gravity has the role of increasing the relative importance of Marangoni to Rayleigh effects and also reduces the Bond number or the effect of gravity waves. In this paper, different gravity levels will be chosen and a lowering of gravity will therefore reduce both gravity waves as well as the Rayleigh effect. Unlike Smith (1966), we will not study the case where only capillary and gravity waves are considered and where buoyancy is ignored. If the total depth is reduced for a given system, we have the effect once again of increasing the Marangoni effect relative to the Rayleigh effect in both phases. However, for a fixed total depth, decreasing ℓ has the role of increasing the Rayleigh effect in the lower phase at the expense of the Rayleigh effect in the upper phase. Besides, it also has the effect of increasing viscous resistance in the upper phase and this will play a role in the flow structure that the fluid bilayer system settles into. In what follows, we shall refer to figure 2, which shows four possible flow ‘modes’ or ‘scenarios’ at the interface at the onset of convection.

The actual ‘mode’ that a system settles into depends upon the thermophysical properties, gravity, total depth and depth ratio, but we will be less concerned about the mode that is realized and more concerned with the sequence of transitions from one mode to another as control parameters change and, therefore, will make general statements regarding this transition sequence for a variety of configurations. These statements will then be ‘verified’ by appealing to specific calculations on particular fluid–fluid systems and do not entail a mathematical proof.

It is instructive to note the relation between these modes. When the onset state of motion of the fluid bilayer goes from mode I to mode II, it simply means that a crest must gradually transform into a trough and the flow directions do not change at any particular lateral position along the interface. In going from mode II to mode III, two things happen: first, the crests and the troughs become progressively smaller and, second, the interface approaches the base state temperature. This change continues until the positions which were formerly crests now become troughs and vice versa. Meanwhile, the temperature perturbations also reverse in sign (cf. figure 2). Mode IV is seen only in one of the cases that we discuss, and changes to mode I under some

conditions. The transition between I and IV is similar to that between II and III. It is clear that the mode transitions must be smooth in the sense that the only way in which any two modes can coexist is in the asymptotic case where the interface is flat. Otherwise sudden mode transitions would imply the existence of codimension 2 points. It is easily seen that such codimension 2 points are precluded as the critical Marangoni number is simple, unique and obtained as the ratio of two determinants resulting from the imposition of the boundary conditions, while the corresponding eigenfunction is unique and this issue is made clear by Nadarajah & Narayanan (1987). In other words, we cannot ever get two or more coexisting flow modes at the critical Marangoni number for the laterally unbounded case.

There are some specific characteristics of the Marangoni and Rayleigh effects which are worth stating. First, if the Marangoni effect is operative alone then hot fluid at the interface must move towards the cold spot and the flow mode may be either I or II. Now, whether the hot region at the interface is a trough, as in mode I, or a crest, as in mode II, depends on the magnitude of the forces and the mechanical and viscous resistances in both phases. This is so as the interface at the hot spot will then bump towards the region that exerts the greater resistance to flow in that region. Second, if the Rayleigh effect is operative alone then matters become a little complicated. In the case of a liquid-liquid bilayer, the upper fluid offers resistance on account of its viscosity and density and yet it conducts heat. We can expect to see any of the modes depending on the forces at play and the magnitude of the resistance. As we continue to consider the pure Rayleigh effect, but now restrict the study to the 'heated from above' problem, it initially appears that no steady flow will occur unless we have the odd case of a positive thermal expansion coefficient. However, this premise can be shown to be false. We refer the reader to Gershuni & Zhukovitskii (1980). These authors discuss a case where the upper fluid is less conductive than the lower fluid and has also a much smaller thermal expansivity. In that peculiar case, we can see that a mechanical perturbation to the upper fluid sends a hot fluid element towards the interface, where it easily transmits heat to the more conductive lower region. This in turn excites buoyancy-driven motion in the lower phase and, as a result, momentum from the lower phase is transmitted to the viscous upper layer and the process continues. Because Gershuni & Zhukovitskii (1980) studied the case of water and mercury, we verified their results as a test of our numerical method, but otherwise did not consider this particular system further. In the unusual case where the lower fluid has a positive thermal expansion coefficient, we obtain mode IV for a liquid-gas system because it is easier to push light cold fluid upwards and towards the interface. We will now discuss these problems in the following sections and provide numerical evidence for various system calculations. In what follows, both buoyancy and interfacial tension gradients, in general, come into play unless noted otherwise.

(a) *Liquid-gas system*

It is clear in the liquid-gas case that only modes I and II are possible candidates, as the upper fluid is virtually passive, offers little fluid mechanical resistance and hot fluid from below must flow upwards for the reason that this is the situation favoured by both buoyancy and interfacial tension gradient forces. Calculations that treat the upper gas as passive were compared with those that treat it as active and we obtained results that were within 1% of each other insofar as the values of the critical temperature difference were concerned.

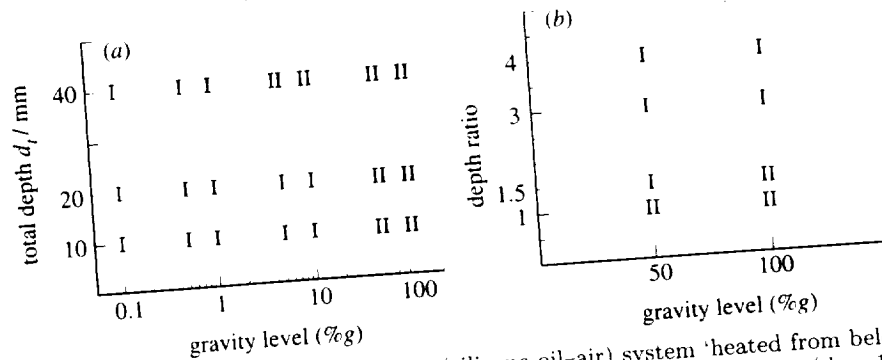


Figure 3. Mode switching for the liquid-gas (silicone oil-air) system 'heated from below': (a) the effect of gravity level and total depth ($\ell = 1$); (b) the effect of depth ratio ($d_t = 10$ mm).

If this system were 'heated from above' at the upper plate, then it would be very stable as calculations tell us that the critical negative temperature gradient is extremely large. This is contradictory to the experimental results of Block (1956) and we believe that the flow he had must have resulted from non-uniform heating or meniscus effects. For the case of 'heated from below', if the Marangoni mechanism alone is operative with negligible gravitational effects, then the flow will align itself into mode I as the resistance to flow is greater in the lower phase leading to a trough at the hot spot. If buoyancy alone were operative then either mode is possible depending on the mechanical and viscous resistance to flow offered by the lower phase. For example, if ℓ were large then mode I would be preferred, compared to mode II, since the hot spot would once again become a trough according to the criterion established earlier. On the other hand, if ℓ were small and the resistance decreased relative to the buoyancy then the system would align itself to mode II, giving rise to a situation where hot plumes rise towards a crest in order to balance the cold heavy fluid flowing down from a trough.

The modal transitions (in the combined Rayleigh-Marangoni case) must therefore proceed from II to I in figure 2 as we reduce gravity and, depending on the system, the reduction in gravity level may have to be significant. Figure 3a shows the flow modes as a function of gravity and depth levels for the silicone oil-air system and we observe that our arguments are validated by the numerical calculations. A calculation of the critical temperature gradients show a monotonic behaviour in the vicinity of the flow switch. In this regard, we agree with the conclusions obtained by Sarma (1987), who considered the upper phase to be truly passive.

From our earlier comments, we can see that a reduction in the total depth causes a relative increase of Marangoni to Rayleigh effects. We therefore see a transition from mode II to mode I as the total depth is decreased. For a fixed total depth and gravity level, an increase in ℓ should cause a decrease in the lower phase Rayleigh effect in comparison to the Rayleigh effect in the upper phase. But the upper phase is a gas and is largely passive and therefore an increase in ℓ can only cause a decrease in the overall Rayleigh effect, and by default it will encourage the Marangoni effect, thereby going from modes II to I, as seen in figure 3b.

A comment on Ferm & Wollkind's (1982) paper is in order. They performed a calculation in the silicone oil-air system to find the depth for the transition from Marangoni to Rayleigh dominant regimes. Using a value of $\ell = 0.109$ they obtained a value of $d^- = 6.5$ mm, whereas we obtain a value of 2.5 mm. It is to be noted that our notion of mechanism change is given by the flow scenarios as manifested

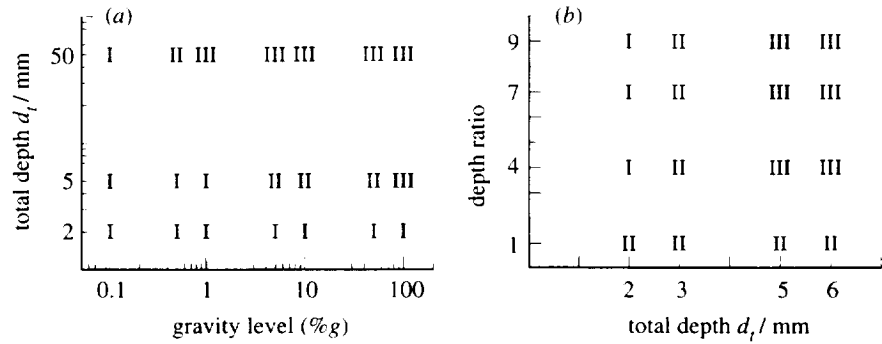


Figure 4. Mode switching for the liquid-liquid (water-benzene) system 'heated from below': (a) the effect of gravity level and total depth ($\ell = 4$); (b) the effect of depth ratio (1g).

in figure 2, and in the liquid-gas system we can only obtain the first two modes. Ferm & Wollkind (1982) indicated that the mechanism changed from Marangoni- to Rayleigh-dominant when there was a change in the slope of the graph between critical temperature gradient and lower phase depth. We feel that our classification is more definitive as it identifies various scenarios at the interface between both fluids.

(b) Liquid-liquid systems

Liquid-liquid systems are interesting as they may be examined with two different heating directions and we choose the water-benzene system to explain the physics because it provides a good test case to verify the detailed results of Zeren & Reynolds (1982).

The modal sequence as we increase gravity, and also 'heat from below', goes from mode I to mode II and then to mode III. The reason why we can expect to see mode III as gravity is increased from mode II is because the Marangoni effect becomes less important and less work is required to push up the short cold columns seen in III as opposed to the tall cold columns seen in IV. In fact, mode IV occurs for the peculiar situation where the thermal expansion coefficient is positive, and this we will discuss later. The particular system that we have investigated has a large value of a , the thermal expansion coefficient ratio[†], and therefore it is generally biased towards greater buoyancy in the upper phase in comparison to the lower phase, unless of course ℓ becomes so small so as to discourage buoyancy in the upper phase in favour of the lower phase. It is for this reason that, as gravity is increased from mode II, the fluid goes into mode III for all of the ℓ values that we have used. Further, it is at the point of mode switching that the Marangoni effect ceases to be of importance and this is seen by the fact that the fluid at the interface does not move from hot regions to cold regions. However, once the fluid is in mode III, the Marangoni effect delays the instability by raising the critical temperature difference. When the mode changes from mode II, upon decreasing gravity, then mode I, which is favoured by the Marangoni effect, is realized. It should be noted that the mode can remain in mode II and never change into mode I on the reduction of the gravity level. This peculiarity once again has to do with the value of ℓ and upon the viscosity ratio

[†] All of our calculations and statements in the case of liquid-liquid systems are restricted to the situation where the ratio of the upper phase thermal expansion coefficient to the lower one is much greater than unity. The reverse case is not discussed in the cause of brevity but the physically based arguments follow in a similar manner.

s. If the upper fluid is very viscous and ℓ is small then more resistance to flow is exerted by the upper phase, preventing the interfacial tension from flattening out a crest and thereby disallowing a mode II structure to develop into a mode I type. It turns out that this observation was mathematically proven by Smith (1966) for the problem that considered only gravity and capillary waves without buoyancy effects. We have also checked and verified Smith's assertion by considering a water-benzene bilayer with a value of $\ell = 0.5$ for very low gravity levels and obtained a mode II flow structure.

The roles of total depth and ℓ are somewhat complicated for the liquid-liquid problem that is 'heated from below'. As the effect of reducing the total depth is to favour the Marangoni over the Rayleigh effect, this simply means that the mode switching for this heating direction goes from mode III to mode II and then to mode I as total depth is reduced. Figure 4*a* bears this out. Of course, for very low ℓ , mode II is obtained on account of the viscous-mechanical resistance to flow in the upper phase and figure 4*b* bears this out.

Now, if total depth and gravity are kept constant and ℓ alone is increased, physical reasoning demands that the buoyancy effect in the upper layer increases relative to the lower layer. Let us suppose that the fluid properties and conditions are such that the fluid settles into mode II. If the total depth is small[†] and we continue to increase ℓ , we expect the flow to switch from mode II to mode I, because the interface gets closer to the hot lower surface in what is already a thin layer and the Marangoni effect plays a dominant role when the interface gets close to the lower hot surface, thereby giving rise to a hot trough. Meanwhile, in this thin layer, the large value of ℓ causes the Rayleigh effect in the upper layer to become more significant than in the lower layer. Buoyancy in the upper layer tends to cause hot plumes to rise in that layer, in opposition to the Marangoni-influenced flow at the interface. As a result, we see a vertical stacking of flow cells in the upper phase as ℓ is increased. The upper cell in the upper phase is a result of the buoyancy in that phase and the lower cell in the upper phase is a result of the Marangoni motion that results on account of the proximity of the interface to the lower heated surface. The cell stacking persists even as the mode switches from II to I. The effect of ℓ for a small total depth is seen in the left region of figure 4*b*, while figure 5 depicts the velocity and temperature eigenfunctions when vertical stacking takes place.

Contrast the situation discussed above with the case where the total depth is large: we then expect the fluid to switch from mode II to mode III as ℓ is increased and the explanation for this is as follows. The large total depth increases buoyancy in both phases; the upper phase being even more buoyant than the lower on account of two reasons. First, the increasing value of ℓ continues to enhance the buoyancy in the upper phase in relation to the lower and second, but less important, the value of a is much greater than unity (in the systems that we chose to compute). As the upper layer is now very buoyant, it would require less work for the fluid to go into mode III, where a shorter column of fluid is pushed up against gravity in both phases, in contrast to the situation of mode II. Remember that a shorter column of liquid is pushed up against gravity in mode I as well, but the system would prefer mode III as the upper phase portrays more buoyancy in this mode as

[†] The notion of large total depth or small total depth is entirely system dependent and only calculations or experiments can determine how large the total depth should be for us to see what we predict. However, we can still make statements of a qualitative manner and verify them by calculations.

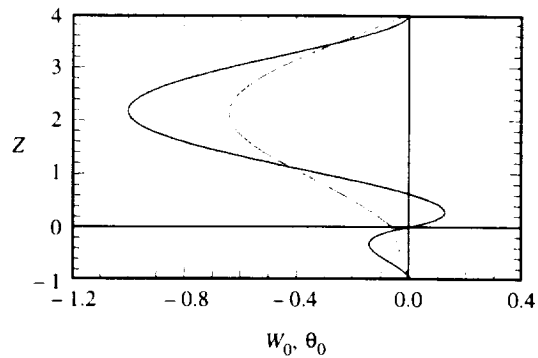


Figure 5. The perturbed axial component of velocity and temperature as a function of z -coordinate in a water–benzene system ‘heated from below’ ($1g$, $d_t = 2$ mm, $\ell = 4$): —, velocity; - - -, temperature.

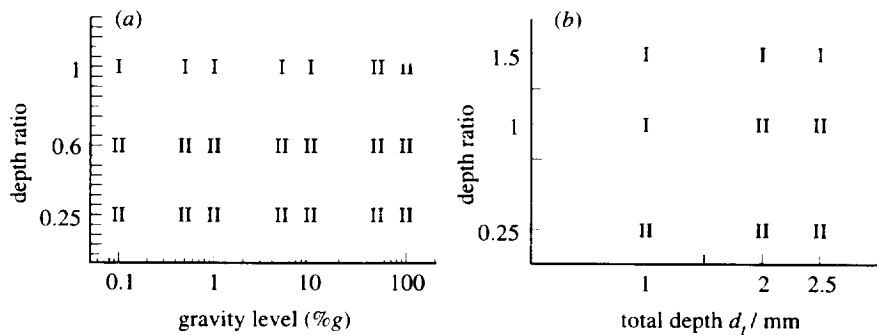


Figure 6. Mode switching for the liquid–liquid (water–benzene) system ‘heated from above’: (a) the effect of gravity level and total depth ($d_t = 2$ mm); (b) the effect of depth ratio ($1g$).

compared to mode I. The numerical calculations confirm the physical arguments, as seen in the right-hand region of figure 4*b*. In these cases, where a large total depth is considered, an increasing value of ℓ does cause the interface to get closer to the hot lower rigid surface, however it is not close enough to encourage an overriding effect of Marangoni-influenced motion, and that is why the system settles into mode III with cold troughs. At the intermediate values of total depth, mode II remains as expected for all values of ℓ .

When the water–benzene bilayer is ‘heated from above’, we predict a sequence from mode I to mode II as we increase gravity; the explanation for this mode switch is as follows. ‘Heating from above’ causes convection that is started by a Marangoni influence and therefore the flow must necessarily be in either mode I or mode II. Meanwhile, gravity serves the purpose of stabilization and therefore delays the instability. Now the value of a , the thermal expansion coefficient ratio, is much greater than unity in the system studied and an increase in gravity causes an increase in the resistance to flow in the upper phase because of the stabilization effect. This in turn causes the switch into mode II, creating hot crests at the interface.

Likewise, for the ‘heated from above’ case, the mode switching goes from mode II to mode I as we decrease total depth for the reason that a decrease in total depth is tantamount to a decrease in the stabilizing Rayleigh effect in each phase, thereby enhancing the Marangoni effect. If we again consider gravity and total depth to remain constant but vary ℓ for the ‘heated from above’ case, we will go from mode II

to mode I as ℓ is increased. This mode switch will take place when the total depth is small, because an increase in ℓ has the effect of increasing the viscous resistance in the lower phase, even though it makes the upper phase more stabilizing than the bottom phase. When the total depth is large, the effect is mainly to make the upper phase stabilizing, thereby increasing the resistance there and so mode II remains intact for all ℓ . Note, as a result of our reasoning, the ‘heated from above’ configuration cannot cause vertical stacking. Vertical stacking can occur only when both Marangoni and Rayleigh effects destabilize in a particular phase and yet when both act in opposition to each other in a ‘flow direction’ sense. This does not occur in the ‘heated from above’ configuration with a negative thermal expansion coefficient. Our thinking in the above is underscored by the numerical calculations that are presented in figures 6*a, b*.

A comment on Smith’s (1966) paper is in order. His study was concerned with Marangoni convection in the presence of gravity waves but without a buoyancy mechanism. No mention was made of hot or cold spots and only modes where fluid from the lower phase moved upwards or downwards from a crest were considered. Yet a pair of sufficient conditions were obtained to indicate whether flow moved upwards or downwards into a crest. This was obtained by use of a flow indicator as in this study. All of our observations validated Smith’s (1966) derived result.

(*c*) *Solidifying phase below a liquid–liquid bilayer*

The third case is a modification of the ‘liquid–liquid’ problem that is ‘heated from above’. It involves a solidifying phase below the lower layer of liquid. The condition at the boundary of the lower liquid and the adjacent solidifying phase is replaced by

$$D\theta_0^- = \omega\theta_0^- \coth(\omega A). \quad (4.1)$$

It is implicitly assumed that the rate of solidification is slow enough to be negligible and so that there is no net flow in the base state. The perturbed deflection of the solid–liquid interface is given by

$$\zeta_0 = \theta_0^- \quad (4.2)$$

In the above, A is the dimensionless thickness of the lower solidifying phase, scaled with respect to the lower liquid thickness. We note that our calculations exclude the important situation where constitutional supercooling, as considered by Mullins & Sekerka (1964), is involved. The main result from our calculation is that the solid thickness of the lower phase does not affect the flow structure at $1g$ but does affect the flow at low gravity levels. In other words, the coupling is only one way at high gravity. We surmise that even though the solid thickness destabilizes the flow, it is insignificant compared to the overwhelming stabilization of gravity. This result is depicted in figure 7. It is apparent from this figure that solidification at lower levels of gravity may not prove beneficial at all under this heating arrangement as the critical temperature gradient is lowered in the low gravity state and convection is thereby enhanced. As a result, it appears that liquid-encapsulated crystal growth is better conducted under Earth’s gravity conditions as the configuration would be more stable.

We can also determine whether the solid–liquid interface deflection is in phase or out of phase with the upper interface by examining the ratio $\zeta_{(0)}/\eta_{(0)}$. What is even more interesting is that when mode switching takes place as we increase gravity, we find that the deflection at the solid–liquid interface lower phase does not change sign.

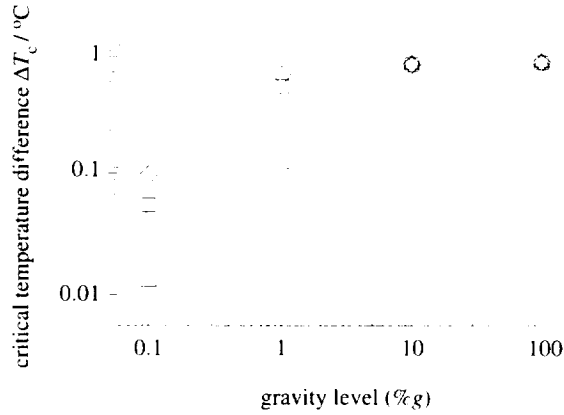


Figure 7. The effect of the solid thickness (i.e. A) on the onset temperature of a gallium-silicone oil system ($d_s = 5$ mm, $\ell = 0.25$) 'heated from above' for different gravity levels: Δ , $\Gamma = 10$; \square , $\Gamma = 1$; \diamond , $\Gamma = 0.01$.

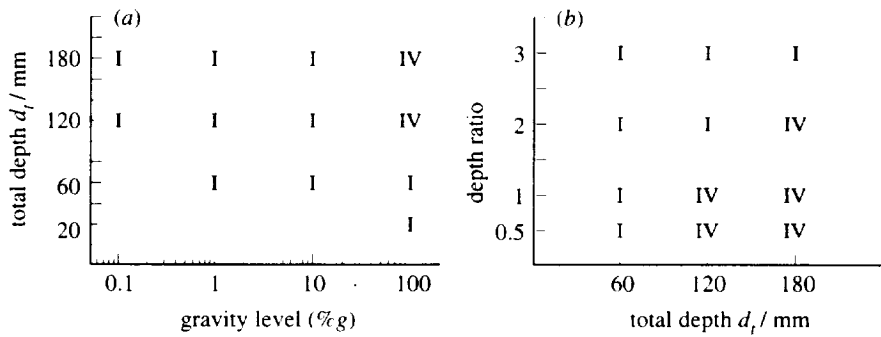


Figure 8. Mode switching for the liquid-gas (water-air) system 'heated from above'. The liquid in this system has a positive thermal expansion coefficient (water is between 0 and 4 °C): (a) the effect of gravity level and total depth ($\ell = 1$); (b) the effect of depth ratio (1g).

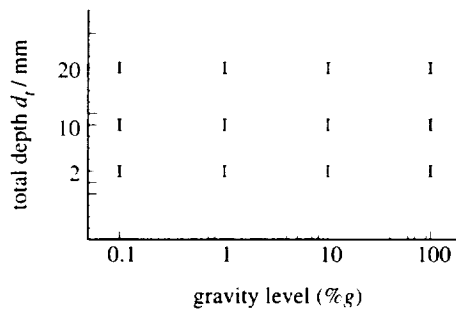


Figure 9. The effect of gravity level and total depth on mode switching for the liquid-gas (water-air) system 'heated from below' ($\ell = 1$). The liquid in this system has a positive thermal expansion coefficient (water is between 0 and 4 °C).

(d) The case of a system with a positive thermal expansion coefficient

Finally, we consider the case of a system where the thermal expansion coefficient of the lower phase is positive. This is exemplified by the results using the water-air system, as shown in figures 8a, b. Here the heating can take place from above or below. If the heating is from above, the origin of the convection can only be due

Table 2. Summary of mode switching

	negative thermal expansion coefficient in liquid		
	liquid–gas system 'heated from below'	liquid–liquid system 'heated from below'	liquid–liquid system 'heated from above'
	increasing gravity level	I → II	I → II → III
increasing total depth	I → II	I → II → III	I → II
increasing depth ratio ℓ	II → I	small total depth II → I	large total depth II → III

	positive thermal expansion coefficient in liquid	
	liquid–gas system 'heated from above'	liquid–gas system 'heated from below'
	increasing gravity level	I → IV
increasing total depth	I → IV	I
increasing depth ratio ℓ	IV → I	I

to buoyancy as the upper layer is virtually passive. The flow, as expected, stays in mode IV for large gravity levels. While the convection is necessarily of buoyancy in origin, it is also true that the Marangoni effect plays a part in countering the flow, thereby delaying the instability. Since the strength of this interfacial mode of convection is dependent on the magnitude of the interfacial tension gradient, we can observe that at low gravity the Marangoni effect is dominant and, as gravity or total depths are reduced, the mode switches to I. Here Marangoni convection causes fluid to move from hot to cold regions at the interface and a shorter column of hot heavier water is balanced by a taller column of cold lighter water. As gravity decreases, the system becomes more stable (despite the change in the flow mode from IV to I) as evidenced by an increase in the critical temperature gradient, just as we would expect. If the water–air system were 'heated from below' so as to allow the temperature range across the water to be between 4 and 0 °C, then it is likewise argued that we would get mode I at all gravity levels, as shown in figure 9. Here the buoyancy stabilizes and the onset flow comes from the interfacial tension gradient. Much like the 'heated from below' configuration in the liquid–gas case for negative

thermal expansion coefficient and pure Marangoni flow, mode I will be the structure chosen by the system.

Table 2 gives a summary of the mode switching explained in the study. Once again, our results depend upon the thermophysical properties of the individual systems chosen in this study. However, the physically based arguments can be similarly made for other systems. We believe that it is valuable to make such arguments in order to identify the mechanisms that dominate the flow structure at an interface.

This work started from discussion during a visit sponsored by the A. v. Humboldt Foundation. C. Wagner was supported by NASA (Langley) grant NAG 1-1474. The work was completed under an NSF grant CTS 9307819. Computations were performed at the Pittsburgh Supercomputing Center.

References

- Block, M. J. 1956 Surface tension as the cause of Bénard cells and surface deformation in a liquid film. *Nature* **176**, 650–651.
- Chandra, D. & Holland, L. R. 1983 Density of $\text{Hg}_{1-x}\text{Cd}_x\text{Te}$. *J. Vac. Sci. Technol. A* **1**, 1620–1624.
- Ferm, E. N. & Wolkind, D. J. 1982 Onset of Rayleigh–Bénard–Marangoni instability: comparison between theory and experiment. *J. Non-equilib. Therm.* **7**, 169–189.
- Gershuni, G. Z. & Zhukhovitskii, E. M. 1980 Instability of a system of horizontal layers of immiscible fluids heated from above. Translated from *Izv. Akad. Nauk SSSR: Mekh. Zh.* **6**, 28–34.
- Gousebet, G., Maquet, J., Roze, C. & Darrigo, R. 1990 Surface tension and coupled buoyancy driven instability in a horizontal fluid layer—overstability and exchange of stability. *Physics Fluids A* **2**, 903–911.
- Joseph, D. D. 1976 *Stability of fluid motions*, vol. I. New York: Springer.
- Koschmieder, E. L. 1967 On convection under an air surface. *J. Fluid Mech.* **30**, 9–15.
- Mullins, W. W. & Sekerka, R. F. 1964 Stability of a planar interface during solidification of a dilute binary alloy. *J. appl. Phys.* **35**, 444–451.
- Nadarajah, A. & Narayanan, R. 1987 On the completeness of the Rayleigh–Marangoni and Graetz eigenspaces and the simplicity of the eigenvalues. *Q. appl. Math.* **XLV**, 81–92.
- Palmer, H. J. & Berg, J. C. 1971 Convective instability in liquid pools heated from below. *J. Fluid Mech.* **47**, 779–787.
- Pearson, J. R. A. 1958 On convection cells induced by surface tension. *J. Fluid Mech.* **4**, 489–500.
- Rasenat, S., Busse, F. H. & Rehberg I. 1989 A theoretical and experimental study of double-layer convection. *J. Fluid Mech.* **199**, 519–540.
- Renardy, Y. & Joseph, D. D. 1985 Oscillatory instability in a Bénard problem of two fluids. *Physics Fluids* **28**, 788–793.
- Sarma, G. S. R. 1987 Interaction of surface tension and buoyancy mechanisms in horizontal liquid layers. *J. Thermophys. Heat Transfer* **1**, 129–135.
- Scriven, L. E. & Sternling, C. V. 1964 On cellular convection driven by surface-tension gradients: effects of mean surface tension and surface viscosity. *J. Fluid Mech.* **19**, 321–340.
- Smith, K. A. 1966 On convective instability induced by surface tension gradients. *J. Fluid Mech.* **24**, 401–414.
- Sternling, C. V. & Scriven, L. E. 1959 Interfacial turbulence: hydrodynamic instability and the Marangoni effect. *A.I.Ch.E. Jl* **5**, 514–516.
- Wahal, S. & Bose, A. 1988 Rayleigh–Bénard and interfacial instabilities in two immiscible liquid layers. *Physics Fluids* **31**, 3502–3510.
- Zeren, R. W. & Reynolds, W. C. 1972 Thermal instabilities in two fluid horizontal layers. *J. Fluid Mech.* **53**, 305–327.

Received 28 April 1994; revised 21 February 1995; accepted 28 February 1995

Marangoni convection in multiple bounded fluid layers and its application to materials processing

BY D. JOHNSON¹ AND R. NARAYANAN²

¹*Microgravity Research Centre, Université Libre de Bruxelles,
1050 Brussels, Belgium*

²*Department of Chemical Engineering, University of Florida,
Gainesville, FL 32611, USA*

A brief review of multilayer convective phenomena that is associated with materials processing is presented. Several instability phenomena that can occur in a bilayer of two fluids heated from either above or below and the effect of laterally and vertically confined geometries are explained. In particular it is shown that such confinement can lead to the occurrence of codimension-two points and pure thermal coupling that is initiated by convection in an upper gas phase during liquid–gas bilayer convection. Experimental evidence that shows the effect of geometrical restrictions is given.

Keywords: Rayleigh; Marangoni; interfacial tension driven convection; buoyancy driven convection; multiple fluid level convection

1. Introduction and physics

Much of the work reported in this paper has been motivated by the need to understand a technique for growing certain crystalline materials, known as the liquid-encapsulated vertical Bridgman (LEVB) crystal growth method. Liquid-encapsulated crystal growth is a process for producing III-V semiconductor crystals from bulk liquid melts. The demand for crystals of increasingly higher purity and lower defects requires us to understand this process in much greater detail. Some examples of crystals grown using this technique are gallium arsenide (GaAs) and indium phosphide (InP). Taking GaAs as an example, when GaAs is melted, it has a tendency to decompose, releasing arsenic gas and destroying the desired stoichiometric ratio. To prevent this decomposition, a liquid encapsulant of boric oxide (B_2O_3) is placed on top of the gallium arsenide. In addition, an inert gas may be placed on top of the B_2O_3 . These three layers are placed in a crucible, which is lowered through a temperature gradient created by a furnace. The lower end of the crucible is cooled, thereby solidifying the gallium arsenide. This configuration is shown schematically in figure 1. The heating configuration generates vertical as well as radial temperature gradients and, consequently, interfacial-tension-gradient-driven convection, also known as Marangoni convection, and buoyancy-driven convection, also called Rayleigh convection, can occur at the liquid–gas and liquid–liquid interfaces as well as in the bulk fluid regions.

While the LEVB technique is the motivation for this study, only by considering simple systems can we have a clearer understanding of the physics of the convective process. Radial gradients of temperature, creeping of the encapsulant along the vertical sidewalls and solutal gradients all have a complicated effect on the convection.

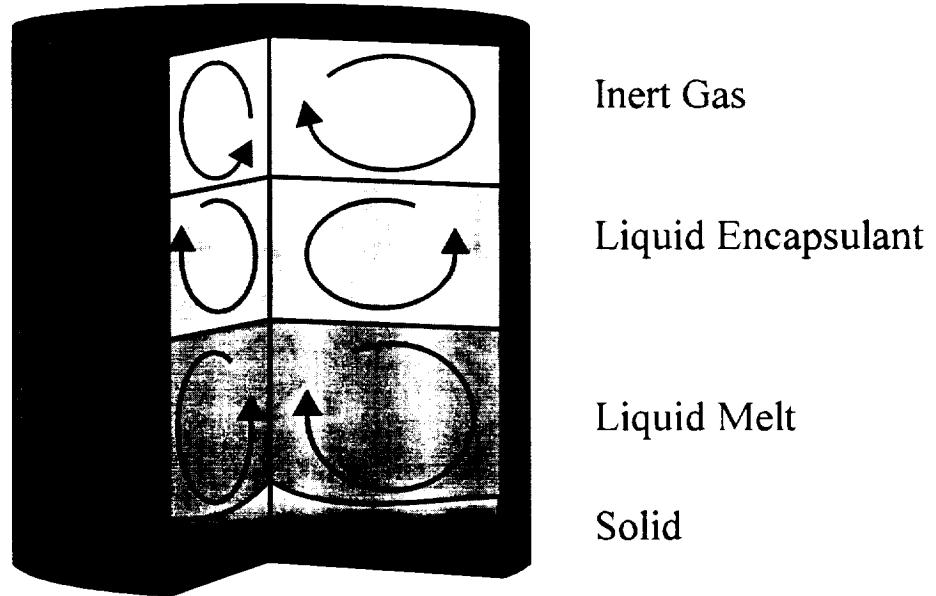


Figure 1. Schematic of a liquid encapsulated crystal grower: a system of three convecting fluid layers. Convection in the GaAs liquid influences the quality of the GaAs solid.

Indeed the onset of convection in an actual LEVB system occurs simultaneously with the application of any temperature gradient. However, a clear understanding of convection in LEVB and many other materials processing methods requires us to consider problems where classical fluid mechanical procedures may be employed, thereby simplifying the mathematics while simultaneously revealing the essential physical features.

One such problem is the Rayleigh–Marangoni problem. Here a gas or another liquid superimposes a liquid layer and a vertical temperature gradient is applied. Suppose that the density and interfacial tension of the liquid decreases with increasing temperature. As the liquid is heated from below, it is top heavy. A small disturbance can upset this arrangement if the overall temperature difference is large enough and flow can ensue in the form of buoyancy or Rayleigh convection. However, flow can occur even in the absence of gravity. For example, in the quiescent state the liquid–gas interface is flat and a small disturbance to it causes a transverse temperature gradient at the interface causing fluid to flow from warm regions of low interfacial tension to cold regions of high interfacial tension. Hot fluid from below rises to the interface and cold fluid from the interface moves down to maintain continuity of fluid flow and the convection continues as Marangoni convection. For small values of the vertical temperature gradient, the fluids remain quiescent and transport heat by pure conduction. However, when the temperature gradient reaches a critical value, even the smallest disturbances imposed on the system amplify with time and the system reaches a steady or time-periodic steady state. In other words a critical temperature gradient is required for convection to occur. More details on the nature of this type of convection are available in the reviews of Koschmieder (1993) and Davis (1987). We will explain the physics of single and multilayer convection in laterally bounded geometries where the layers are heated from above making them gravitationally stable and where the layers are heated from below making them gravitationally unstable. The explanation of physics in multilayers will be followed by a report on two sets of

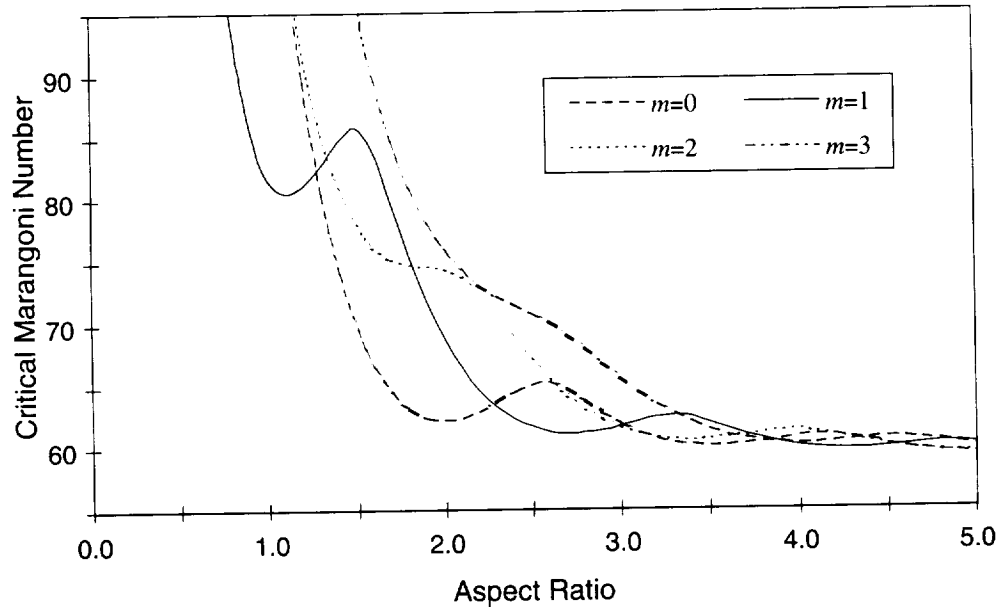


Figure 2. Plot of the critical Marangoni number versus the aspect ratio of a cylinder. The mode, m , with the smallest Marangoni number at a given aspect ratio is the mode or flow pattern at the onset of convection.

experiments. Noticeably absent from this paper will be the effects of solutal convection, some aspects of which have been covered by several other authors (McFadden *et al.* 1984; Turner 1985). It should be noted that this paper is a brief report of the work done by us and a few other researchers. Greater detail is available in the thesis by Johnson (1997) as well as papers by Johnson & Narayanan (1996, 1997, 1998). Fuller explanations of the effects of convection on crystal growth are given by Hurle (1994), Müller (1988) and Schwabe (1981).

The extent of convection is often characterized by a dimensionless temperature difference represented by the Marangoni or Rayleigh numbers. The Marangoni number is proportional to the depth of the liquid, the temperature difference and the variation of the surface tension with respect to the temperature and inversely proportional to the dynamic viscosity and thermal diffusivity. The Rayleigh number is proportional to the cube of the liquid depth, gravity, the temperature difference and the thermal expansion coefficient and inversely proportional to the kinematic viscosity and the thermal diffusivity. In a physical system, fixing the temperature difference necessarily fixes both the Rayleigh and Marangoni numbers.

We begin by confining our discussion to a single layer of fluid, heated from below, with a free surface. In this configuration both buoyancy and interfacial-tension forces become important. For larger depths, buoyancy is more important than interfacial-tension effects, and when the fluid depth is small, interfacial-tension forces dominate convection.

(a) Physical effects of a bounded geometry

Consider a single layer of fluid bounded below by a rigid conducting plate and whose upper surface is bounded by a passive gas. By a passive gas we mean a gas which has no viscosity and only conducts heat away. The lower plate here is at a higher temperature than the passive gas. In a fluid of infinite horizontal extent,

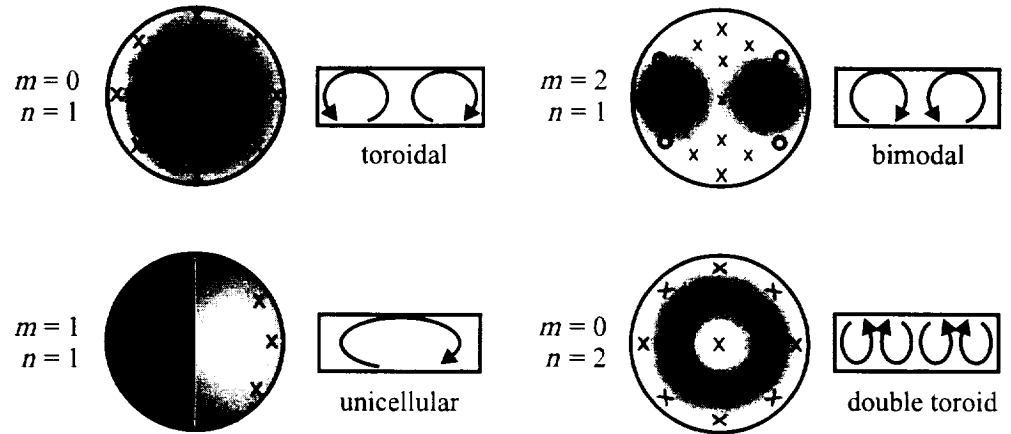


Figure 3. Schematic of four different flow patterns: \circ , fluid flowing up; \times , fluid flowing down.

there is no limit on the number of convection cells. However, in a bounded finite-sized container only a finite number of convection cells may exist. Physically this means that at the onset of convection in a bounded cylinder, only one flow pattern will usually exist. As the aspect ratio (radius/height) of the container increases, more convection cells will appear. Figure 2 is a representative calculation of the critical Marangoni number for various aspect ratios and for different azimuthal modes m . The Biot number, which is a dimensionless surface heat-transfer coefficient is equal to 0.3.

In a bounded cylinder, each flow pattern is associated with an azimuthal mode, m , and radial mode, n . For example, at an aspect ratio of 1.0 in figure 2, there is an $m = 1$, $n = 1$ flow pattern (see figure 3). For an aspect ratio of 1.5, there exists an $m = 0$, $n = 1$ flow pattern. The azimuthal mode is the number of times the azimuthal component of velocity goes to zero, and the radial mode is the number of times the radial component of velocity goes to zero starting from the centre for a given vertical cross-section.

At particular aspect ratios, where the fluid switches from one flow pattern to the next, there coexist two different flow patterns. These aspect ratios are known as codimension-two points. For certain codimension-two points, the flow patterns will interact nonlinearly to yield oscillatory behaviour (Rosenblat *et al.* 1982; Johnson & Narayanan 1996). This phenomenon will be shown later in § 2.

(b) Physical effects of multiple fluid layers

Imagine a less dense immiscible layer of fluid above the lower layer of fluid. Here the lower layer is bounded below by a rigid conducting plate and another rigid conducting plate bounds the upper layer. Once again let the temperature of the lower plate be greater than the upper plate. The interface between the two fluids may deform and is capable of transporting heat and momentum from one layer to the other. We will now consider the various types of convection that can occur in a bilayer of two fluids.

In order to distinguish the various convection mechanisms, we introduce phrases such as 'convection initiating in one layer or another'. Strictly speaking, convection occurs in both fluids simultaneously, although one layer may be more unstable than the other, driving flow in the other layer.

Turning now to various convective mechanisms, consider figure 4. Suppose that convection initiates in the lower layer. The upper layer responds by being dragged,

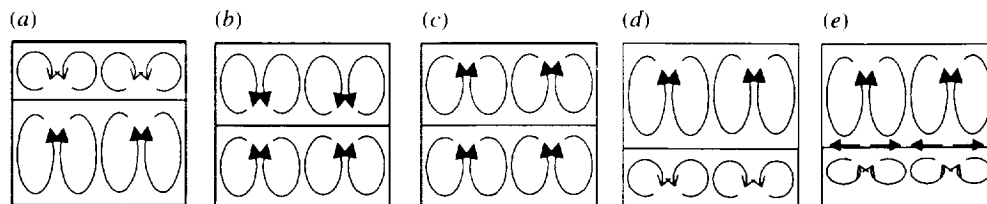


Figure 4. Schematic of the different types of convection-coupling: (a) lower dragging mode; (b) viscous coupling; (c) thermal coupling; (d) upper dragging mode; (e) pure thermal coupling. Moving from (a) to (e), the buoyancy force in the upper layer increases. Gas-liquid thermal coupling, with surface-driven flow, is caused by the upper fluid buoyantly convecting and simultaneously inducing interfacial-tension- or buoyancy-driven convection in the lower layer near the interface.

generating counter rolls at the interface. Hot fluid flows up in the lower layer and down in the upper layer. The upper layer is not buoyant enough and moves by a combination of viscous drag and the Marangoni effect. This is seen in figure 4a. The sign of the velocity switches and the maximum absolute value of the lower-layer velocity is much greater than the maximum absolute value of the velocity of the upper layer.

When the buoyancy in the upper layer increases and the upper layer begins to convect, one of two things can happen. The first possibility is that the two fluids are *viscously coupled*. Physically this can be shown in figure 4b as counter-rotating rolls in the two fluids. This can also be denoted by the vertical component of velocity switching sign at or near the interface, while the temperature perturbations indeed switch sign at the interface itself. If the temperature perturbation switches sign near the interface in either layer near the interface we would say that the bilayer is nearly viscously coupled. In particular if the switch takes place in the upper fluid near the interface, then the lower layer is slightly more buoyant. If the temperature perturbation switches sign in the lower layer, then the upper layer is more buoyant. The Marangoni phenomenon, for fluids, whose interfacial tension decreases with an increase in temperature, plays an ambiguous role here. The hot fluid flowing up in the lower layer causes the fluid at the interface to move in the same direction. However, the colder fluid moving down in the upper layer contradicts this. The exact effect the Marangoni phenomenon has on the two fluids depends on where the thermal perturbations change sign. For the situation where the thermal perturbations switch sign at the interface there is no Marangoni effect.

The second possibility is *thermal coupling* where the rolls are corotating (figure 4c). Here hot rising fluid from the lower layer causes hot fluid in the upper layer to flow up. The maximums of the vertical component of velocity and the temperature perturbations have the same sign in each fluid layer. Strictly speaking, the transverse components of velocity should be zero at the interface. However, thermal coupling is sometimes referred to the case when a small roll develops in one of the layers so as to satisfy the no-slip condition at the interface. In this situation, when the interfacial tension decreases with an increase in temperature, the Marangoni effect encourages flow in the lower fluid layer, and discourages the flow in the upper fluid.

Another interesting phenomenon is present at certain fluid depths where both thermal and viscous coupling can occur. At these depths, a competition arises between the two types of convection. As both convection configurations cannot occur simultaneously, the fluids begin to oscillate between these two states. This phenomenon was

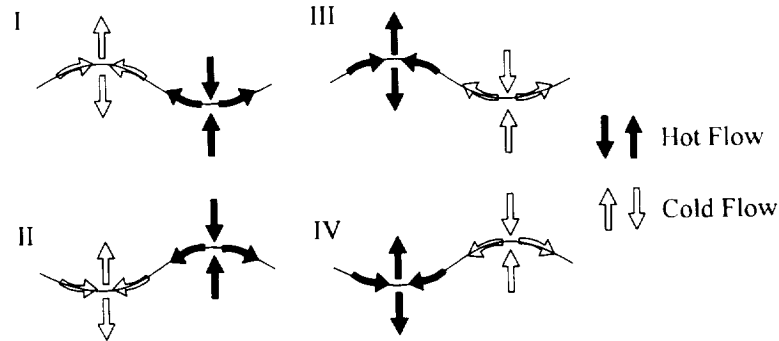


Figure 5. The four possible interfacial structures at a fluid-fluid interface. Each structure can give information about the driving force of the convection.

first reported by Gershuni & Zhukhovitskii (1982), and has recently been confirmed by Andereck *et al.* (1996).

As the buoyancy continues to increase in the upper layer, convection initiates in only the upper layer and the lower layer is viscously dragged (figure 4d). This situation only occurs when the upper fluid is a liquid, as gases are very tenuous and will not exert much shear. The vertical component of velocity in this case switches sign and the magnitude of convection in the upper fluid is much greater than the magnitude of convection in the lower fluid.

The last figure (figure 4e) is an example of what may be called *pure thermal coupling*. This typically occurs in a liquid-gas system where buoyancy convection is predominant in the gas layer. The convecting gas then simultaneously creates a non-uniform temperature profile across the liquid-gas interface and generates either Marangoni or buoyancy-driven convection in the lower layer (Johnson *et al.* 1998). Notice that the convection in the lower layer is now generated purely by horizontal temperature gradients at the interface and not by viscous dragging. To maintain the no-slip condition at the interface a small counter-roll may develop in the gas-phase. This roll is not shown in figure 4e.

(c) Physics of interfacial structures

Another indicator of what is occurring in bilayer convection can be inferred from the fluid-fluid interface instead of the bulk convection. In a paper by Zhao *et al.* (1995), four different interfacial structures were identified for any given convecting bilayer with a deflecting interface. Each of these structures depends upon whether fluid was flowing into or away from the trough or the crest, and whether the fluid was hotter or cooler at the trough or the crest of the interface. Hot fluid flowing into a trough defines the first interfacial structure. The second interfacial structure has hot fluid flowing into a crest. The third structure has hot fluid flowing away from a crest and the fourth structure has hot fluid flowing away from a trough. Each of these four scenarios is given in figure 5.

One of the important factors to consider in interfacial structures is the direction of the flow along the interface. As interfacial tension is usually inversely proportional to temperature, at cooler regions of the interface, the interfacial tension will be higher and will pull on the interface. Where the interface is hotter, the interfacial tension will be lower causing the fluid to move away from warmer regions. Another important factor is the direction of the flow into or away from a crest or a trough. One reason the interface deflects is due to bulk convection, caused by buoyancy effects, pushing

against the interface. Consider two fluids whose dynamic viscosities are equal. If buoyancy-driven convection is occurring mostly in the lower layer, then the fluid will flow up from the lower layer into a crest. If the fluid flows down from the top layer into a trough, then one would argue that buoyancy-driven convection occurs mostly in the upper fluid.

In each of the four cases, the interfacial structure can be used to indicate the driving force of the convection. In the first interfacial structure, the dominating driving force is interfacial-tension-gradient-driven convection. This is seen as the cold fluid, with the higher interfacial tension pulling the fluid up into the crest. The first interfacial structure can also occur by buoyancy-driven convection in the upper layer, when the density of the upper layer increases with an increase in temperature. In the second interfacial structure, buoyancy drives convection in the lower phase. The hot rising fluid pushes the interface upwards. As the fluid moves along the interface, it cools and eventually sinks back down. The third interfacial structure is dominated by buoyancy-driven convection in the upper phase or by interfacial-tension-driven convection where the interfacial tension increases with respect to temperature. The fourth interfacial structure only occurs when the lower fluid has a positive thermal-expansion coefficient. In other words, the density increases with an increase in the temperature, causing the cooler lower fluid to flow up into a crest.

Knowledge of interfacial structures will be beneficial in the understanding of certain materials processing problems such as drying of films, coatings and deposition.

(d) *Physics of heating from above*

In the previous subsections we talked about some of the phenomena that occur in single- and multiple-fluid layers heated from below. However, in an attempt to avoid convection in crystal growth, the crucible is often cooled from below and heated from above. This heating configuration changes the physics of the problem, which is the topic of this subsection.

When a layer of fluid is being heated from above, it creates a stable density stratification. Therefore not only does the buoyancy force not cause convection, it acts to inhibit other instabilities. Marangoni convection, though, may still occur in fluids being heated from above.

First we will consider a single layer of fluid superposed by a passive gas. If the upper gas is truly passive, then pure Marangoni convection will not occur. For example, suppose some random perturbation causes some part of the surface to become warmer than the rest of the surface. The interfacial tension will decrease in this region and the tension will pull fluid away from this hot spot. By continuity, fluid lying below the hot spot will rise up to replace the displaced fluid. As the lower fluid is cooler than the surface this region now cools off and the interfacial tension increases, thereby restabilizing the region. However, in real systems, the upper fluid is never truly passive. Given the same scenario, fluid movement along the interface will also drag warmer fluid from above. This warmer upper fluid will further increase the temperature in this region, and, depending upon the ratio of thermal-physical properties, reinforces the instability.

By this argument, it appears that an active upper fluid is necessary to have Marangoni convection when the system is being heated from above. However, this is not the case if the buoyancy effects are included. In Rednikov *et al.* (1998), it was demonstrated, theoretically, that oscillatory onset of convection may occur for a single layer of fluid with a purely passive upper gas. The explanation is as follows.

If a small volume of fluid is displaced within the bulk of the fluid, the density stratification acts as a restoring force, causing a dampened oscillation within the fluid. These are often referred to as internal waves. The Marangoni force acts similarly, as discussed above, also giving dampened oscillations. Apparently when these two forces act together they can overshoot one another leading to sustained oscillatory convection. Indeed, as was demonstrated in their paper, this only occurs in certain fluids, at certain depths, where the buoyancy and interfacial-tension forces are approximately equal.

A completely different type of instability is also possible in two layers of fluids being heated from above. Gershuni & Zhukhovitskii (1981) first demonstrated this phenomenon by analysing two immiscible fluids where the interface between the fluids was assumed flat and the Marangoni phenomenon was neglected. They found the onset of steady convection when the thermal conductivity and thermal expansivity of the lower fluid was much greater than that of the upper fluid.

The mechanism of this instability is as follows. Suppose an element of fluid in the upper layer, near the interface, is displaced towards the lower layer. Because the thermal expansion of the upper fluid is so small, this element remains in a relatively neutrally buoyant state. Also, as the thermal conductivity of the upper fluid is small, it cools very slowly. When the two fluids are heated from above, the displaced fluid will be warmer than its surroundings. This element of fluid then heats part of the lower fluid near the interface. The lower fluid, with its relatively large thermal conductivity and thermal expansivity, quickly heats up and expands horizontally. This expansion then causes convection in the lower fluid layer and propagates by viscously coupling with the upper fluid layer. The Marangoni phenomenon, if it were considered, would act to enhance this instability.

Another case of interest is convection induced by the Rayleigh–Taylor instability. This phenomenon can occur in two immiscible fluid layers being heated either from above or below, when the densities of the two fluids are approximately the same and the thermal expansivity of the lower fluid is much greater than the thermal expansivity of the upper fluid. Upon heating, the density of the lower fluid will decrease and become less than the density of the upper fluid. Consequently, the heavier upper fluid will begin to sink causing large deformations in the liquid–liquid interface, generating the Rayleigh–Taylor instability (Chandrasekhar 1961). This problem has been investigated extensively in Renardy & Renardy (1985) and Renardy (1996), but is of application to materials processing only if the densities of both layers are similar.

2. Some experimental observations

The experiments were used to investigate both the oscillatory behaviour near codimension-two points and the pure thermal coupling of air with silicone oil (see figure 4e). Details on the experimental procedure are available in Johnson (1997) and Johnson & Narayanan (1996, 1998).

(a) *Experimental apparatus and procedure*

The experiments consisted of two compartments: one for the lower fluid and one for the air. Lucite inserts were used to give a variety of different fluid depths and aspect ratios. A copper plate was placed below the liquid insert and the air insert was bounded above by a high-thermal-conductivity infrared transparent zinc selenide (ZnSe) window. Heating of the copper plate was done by an enclosed stirred water

bath that was in turn heated by a hot plate. The top of the ZnSe window was kept at a constant temperature by accurately controlling the temperature of the overlying air. The overall temperature control was kept within $\pm 0.05^\circ\text{C}$.

The flow patterns that developed at the silicone oil–air interface layer were visualized with an infrared camera. Although other flow visualization techniques could have been used, such as shadowgraphy or particle tracing, the IR camera was chosen to prove the viability of its use with opaque materials, such as gallium and gallium arsenide. The IR imaging technique is also useful in observing weak thermocapillary flow near the surface, whereas shadowgraphy requires some strength in the domain flow.

To guarantee that the flow pattern seen was indeed the flow pattern at the onset of convection, the temperature difference applied across the bilayer system was carefully increased. At first a temperature difference was applied that was less than the critical temperature difference necessary for the onset of convection. This, and all temperature differences, were kept constant for several characteristic time constants; *ca.* 3–4 h. If no flow pattern was seen, the temperature difference was then increased by as little as 0.05°C . This was repeated until the temperature profile at the interface changed to some distinct pattern, indicating that the fluid had begun to flow. At this point, the flow pattern was recorded and the temperature difference noted.

(b) *Experimental observation of codimension-two points*

As was noted in § 1, there exist certain liquid aspect ratios where two different flow patterns coexist. For example, in figure 2 at an aspect ratio of 2.3, there exists a codimension-two point between the azimuthal modes $m = 0$ and $m = 1$. The questions we want to answer are: What happens at these aspect ratios? Does one flow dominate over the other? Do the different flow patterns coexist as a superposition of both states, or do they oscillate and interact between these two states?

Rosenblat *et al.* (1982) have performed a weakly nonlinear analysis to investigate these questions. They found that all three of these possibilities may occur, depending on the Prandtl number, the particular codimension-two point being investigated, and on which side of the codimension-two point the aspect ratio lies. To simplify their calculations, a vertical and tangential vorticity-free side-wall was assumed. Later a more realistic no-slip condition was applied (Zaman & Narayanan 1996; Dauby *et al.* 1997), where it was noted that the order of azimuthal modes, as the aspect ratio was increased, was different than the vorticity-free condition. These latter calculations were done assuming a linearized instability analysis. Therefore, a direct comparison of the nonlinear analysis with the experiment is not currently possible. Nonetheless, some of the qualitative features should still hold true.

A series of experiments were performed to first find the codimension-two points and then determine the flow patterns at or near the codimension-two point (Johnson & Narayanan 1996). A 5.0 mm-high 2.5 aspect-ratio liquid insert was used in conjunction with a 11.2 mm air height. Table 1 shows the calculated critical Marangoni numbers for four different azimuthal modes for a 2.5 aspect ratio. The table predicts that an $m = 0$ flow pattern should be seen at the onset of convection. However, the critical Marangoni numbers for $m = 1$ and $m = 2$ are also very close to the onset point. Physically, this means that for temperature differences slightly above the critical temperature difference, these modes may affect the flow pattern.

At the onset of convection, a very faint $m = 0$ double-toroidal-flow pattern could be seen. When the temperature difference was increased by just 0.05°C , the flow

Table 1. Critical Marangoni number for the first four azimuthal modes for a 2.5 aspect ratio.

modes	Marangoni number
0	69.37
1	70.84
2	70.41
3	72.98

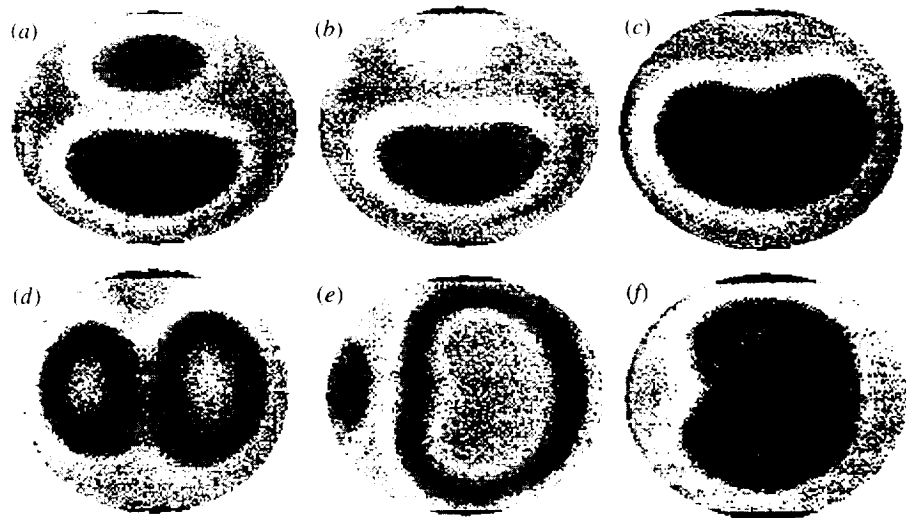


Figure 6. Infrared images showing the mode-switching behaviour in the paper by Johnson & Narayanan (1996). The experiment used 91 cS silicone oil and a 5.0 mm, 2.5 aspect-ratio insert.

pattern changed from the double toroid to a dynamic switching between two and one flow cells (see figure 6).

At first, two symmetric cells appeared (figure 6a). Then, one of the cells would grow and push the other cell out of the picture, forming a superposition of the $m = 0$ and $m = 1$ flow pattern (figure 6b). Next one cell would grow (figure 6c), then split into two cells, rotated by 90° (figure 6d). This process would then repeat itself (figure 6e) arriving back to the original $m = 2$ flow pattern (figure 6f). As long as the temperature difference was held constant, this dynamic process would continue repeating itself approximately every 20 min.

It is noteworthy that oscillatory convection is of particular importance in crystal growth. It has been shown (Hurlé 1994) that fluctuating temperatures in the liquid melt have a deleterious effect on the crystal quality, leading to a higher dislocation density.

(c) Experimental observations of thermal coupling

The thermal coupling of air with the lower fluid was originally discovered by a series of experiments using the same experimental apparatus (Johnson & Narayanan 1998). As was explained in §1, air can thermally couple with the lower fluid caus-

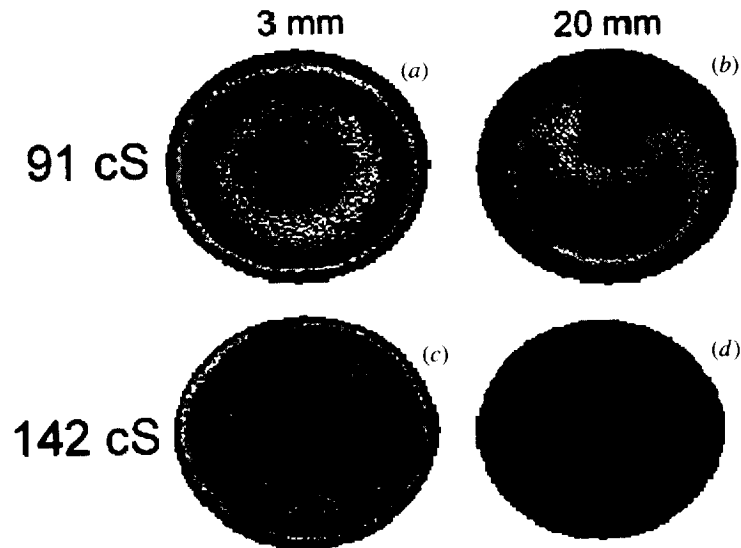


Figure 7. Infrared images of the flow pattern for different air heights and different viscosities of silicone oil. (a) and (b) used a 91 cS silicone oil. (c) and (d) used a 142 cS silicone oil. (a) and (c) had a 3 mm air height, (b) and (d) had a 20 mm air height.

ing interfacial-tension-driven flow in the lower fluid. To explore this, a set of four experiments was performed.

In all of the experiments, a liquid aspect ratio of 2.0 was studied. Two different air heights (3 and 20 mm) and two different viscosities were used. When the air height of 3 mm was used, the flow patterns did not change with viscosity but the temperature difference across the liquid did increase proportionally, indicating that convection was controlled by the liquid phase. The liquid convection pattern also agreed with calculations and the experimental result is seen pictorially in figures 7*a, c*.

When a deeper air height was used, the temperature difference across the liquid at the onset of convection did not change substantially between the experiments that employed different fluid viscosities. This indicated that convection was controlled by the dynamics in the air layer. It may be argued that air convection, when dominant, acts like buoyancy-driven convection between two rigid conducting plates as the lower liquid is much more viscous and more conductive than the air above it. A comparison was therefore made between the measured temperature drops across the air for the deeper air heights and the numerical calculations of Hardin *et al.* (1990). The experimental and theoretical results compared remarkably well and the flow pattern predicted theoretically also compared favourably with the experimental results. This confirmed our hypothesis that deep air heights interact with the lower liquid and drive thermally coupled flow through the interface.

This phenomenon of thermal coupling may not be as important in LEVB because the crucible is often heated from above. However, this may be much more applicable to other important processes, such as evaporation and drying of films.

3. Future work

The research of convection in multiple fluid layers has revealed and continues to reveal many interesting phenomena. However, further work is needed to elucidate

some of the details more fully in a realistic system. One of the more interesting areas involves analysing some of the basic instability phenomena in bounded containers. To do this, two-fluid-layer numerical models that take into account realistic no-slip conditions will be necessary. With a proper model some of the effects, such as the Rayleigh–Taylor instability, the Gershuni–Zhukhovitskii instability and oscillations between thermal and viscous coupling, can be studied for containers with small aspect ratios.

To date, few experiments have been performed in small aspect-ratio containers. As was demonstrated in the codimension-two point experiments, new and interesting dynamics are present in small aspect-ratio containers, which are not present in large aspect-ratio containers. It would be interesting to show the interaction of codimension-two points with such instabilities as the oscillations between thermal and viscous coupling. Additionally, several of the phenomena discovered with theoretical models have yet to be shown in experiments. Two examples are the Gershuni–Zhukhovitskii instability and the oscillations shown by Rednikov *et al.* (1998).

By investigating some of the basic physics of multilayer convection, we obtain a better understanding and appreciation for the liquid-encapsulated crystal-growth process and other fluid materials processing problems where temperature gradients are employed. Further research into this field should lead to improvements in such an important industrial process.

We are grateful to NSF for their support via grants CTS 9307819 and CTS 95-00393 and to NASA via grants NGT 3-52320 and NAG 1-1474. The authors thank Pierre Dauby for figure 2.

References

- Andereck, C. D., Colovas, P. W. & Degen, M. M. 1996 Multilayer convection. *Proc. of the AMS-IMS-SIAM Joint Research Conf. on Multifluid Flows*. Philadelphia, PA: SIAM.
- Chandrasekhar, S. 1961 *Hydrodynamic and hydromagnetic stability*. Oxford University Press
- Dauby, P. C., Lebon, G. & Bouhy, E. 1997 Linear Bénard–Marangoni instability in rigid circular containers. *Phys. Rev. E* **56**, 520.
- Davis, S. H. 1987 Thermocapillary instabilities. *A. Rev. Fluid Mech.* **19**, 403.
- Gershuni, G. Z. & Zhukhovitskii, E. M. 1981 Instability of a system of horizontal layers of immiscible fluids heated from above. *Izv. Akad. Nauk. SSSR, Mekh. Gaza* **6**, 28.
- Gershuni, G. Z. & Zhukhovitskii, E. M. 1982 Monotonic and oscillatory instabilities of a two-layer system of immiscible liquids heated from below. *Sov. Phys. Dokl.* **27**, 531.
- Hardin, G. R., Sani, R. L., Henry, D. & Roux, B. 1990 Buoyancy-driven instability in a vertical cylinder: binary fluids with Soret effect. I. General theory and stationary stability results. *Int. J. Numer. Meth. Fluids* **10**, 79.
- Hurle, D. T. J. (ed.) 1994 *Handbook of crystal growth*. Amsterdam: North-Holland.
- Johnson, D. 1997 Geometric effects on convection in cylindrical containers. Ph.D. thesis, University of Florida.
- Johnson, D. & Narayanan, R. 1996 Experimental observation of dynamic mode switching in interfacial-tension-driven convection near a codimension-two point. *Phys. Rev. E* **54**, R3102.
- Johnson, D. & Narayanan, R. 1997 Geometric effects on convective coupling and interfacial structures in bilayer convection. *Phys. Rev. E* **56**, 5462.
- Johnson, D., Narayanan, R. & Dauby, P. C. 1998 The effect of air on the pattern formation in liquid–air bilayer convection: how passive is air? *Phys. Fluids* (Submitted.)
- Koschmieder, E. L. 1993 *Bénard cells and Taylor vortices*. Cambridge University Press
- McFadden, G. B., Coriell, S. R., Boisvert, R. F., Glicksman, M. E. & Fang, Q. T. 1984 Morphological stability in the presence of fluid flow in the melt. *Metal. Trans. A* **15**, 2117.
- Phil. Trans. R. Soc. Lond. A* (1998)

- Müller, G. 1988 *Crystal growth from the melt*. Berlin: Springer.
- Rednikov, A., Colinet, P., Velarde, M. G. & Legros, J. C. 1998 Rayleigh–Marangoni oscillatory instability in a horizontal liquid layer heated from above: coupling between internal and surface waves. *J. Fluid Mech.* (Submitted.)
- Renardy, Y. Y. 1996 Pattern formation for oscillatory bulk-mode competition in a two-layer Bénard problem. *Z. Angew Math. Phys.* **47**, 567.
- Renardy, Y. Y. & Renardy, M. 1985 Perturbation analysis of steady and oscillatory onset in a Bénard problem with two similar liquids. *Phys. Fluids* **28**, 2699.
- Rosenblat, S., Davis, S. H. & Homsy, G. M. 1982 Nonlinear Marangoni convection in bounded layers. I. Circular cylindrical containers. *J. Fluid Mech.* **120**, 91.
- Schwabe, D. 1981 Marangoni effects in crystal growth melts. *Physicochem. Hydrodyn.* **2**, 263.
- Turner, J. S. 1985 Multicomponent convection. *A. Rev. Fluid Mech.* **17**, 11.
- Zaman, A. & Narayanan, R. 1996 Interfacial and buoyancy-driven convection: the effect of geometry and comparison with experiments. *J. Colloid Interf. Sci.* **179**, 151.
- Zhao, A. X., Wagner, C., Narayanan, R. & Friedrich, R. 1995 Bilayer Rayleigh–Marangoni convection: transitions in flow structures at the interface. *Proc. R. Soc. Lond. A* **451**, 487.

Discussion

J. R. HELLIWELL (*Department of Chemistry, University of Manchester, UK*). Reference has been made to oscillatory convection flow patterns in fluids and that this is known to cause defects (dislocations and fault lines) in crystal growth. My own particular research interests include the growth of protein crystals for X-ray crystal-structure analysis and how the quality of protein crystals can be improved, and thereby exploited, for higher resolution X-ray crystallographic data collection. I have been using CCD and interferometry diagnostic monitoring of protein crystal growth, and have seen benefits of microgravity if the crystals do not move, and if the mother liquor is not subject to convection (including Marangoni convection). The benefits of these conditions manifest as reduced crystal mosaicity and likewise a lack of, or only a few, mosaic blocks in X-ray topographs of crystals in such cases. In his experiment, how can Dr Johnson be sure that it is specifically oscillatory flow patterns that especially caused defects in his type of crystal?

D. JOHNSON. We cannot be sure that oscillatory convection is always responsible for defects in crystals. However, research cited by Hurle (1994) has indicated that oscillatory behaviour generated through double diffusion is the cause of striations along the growth axis in directional solidification. The point of this paper, however, is to show that oscillatory behaviour need not arise merely from opposing forces that are seen in thermo-solutal, otherwise known as double-diffusive, convection. Such oscillatory behaviour can arise by geometrical effects. Indeed as the crystal grows, the aspect ratio of the liquid phase changes and there are certain aspect ratios where the energy states may coexist leading to codimension-two points that can cause oscillatory convection.

S. K. WILSON (*Department of Mathematics, University of Strathclyde, Glasgow, UK*). I complement the authors on a penetrating investigation of a complicated physical situation. As I understand it, they have found examples of slow oscillations between two different steady flow patterns in the vicinity of codimension-two points calculated theoretically using linear theory for the onset of steady convection in a finite-sized container. May I ask if truly oscillatory (rather than quasi-steady) convection is ever observed, and if it would be possible to undertake the same kind of investigation for the onset of oscillatory convection?

D. JOHNSON. Yes, under certain circumstances, we believe that oscillatory convection can be observed in liquid-gas bilayer experiments. Theoretical calculations that were done indicate the absence of such convection at the onset. In that case what is the origin of oscillations in our experiments? The answer lies in the fact that a Hopf bifurcation lies in the vicinity of the onset but only in the post-onset region. The Hopf bifurcation mode or oscillatory mode was excited by the presence of codimension-two points. These points were generated by the fact that at certain aspect ratios two competing flow states coexist and in a manner of speaking the system wants to choose between the flow states leading to continual oscillations.

Rayleigh convection in a closed cylinder—Experiments and a three-dimensional model with temperature-dependent viscosity effects

A. X. Zhao, F. C. Moates, and R. Narayanan

Department of Chemical Engineering, University of Florida, Gainesville, Florida 32611

(Received 12 October 1994; accepted 10 March 1995)

In this paper our most recent research results on natural convection in a closed cylinder, where our interest focuses on pattern structure dependence on aspect ratio and on temperature-dependent viscosity, are summarized. The main results are (a) the experiments on the onset pattern and conditions for pure Rayleigh convection in circular cylinders compare favorably with linearized stability results of Hardin *et al.* [Int. J. Num. Methods Fluids **10**, 79 (1990)], as well as three-dimensional nonlinear calculations made by us; and (b) experiments and nonlinear calculations indicate a variation of the patterns at and near the codimension two points when large temperature differences are introduced, so as to cause a substantial change in viscosity. © 1995 American Institute of Physics.

I. INTRODUCTION

The physics of Rayleigh convection is well understood and the classical theory has been reviewed in the treatise by Chandrasekhar¹ and in the recent book by Koschmieder.² In this problem, a layer of fluid is heated from below, and one of the objectives is to determine the conditions for the onset of flow from an erstwhile quiescent state, as well as the associated pattern. The critical temperature difference for the onset of flow is given in terms of the Rayleigh number. This group expresses the ratio of the buoyancy force, which precipitates the convection, to the effects that dissipate the flow, viz thermal and momentum diffusivities. In the theory, the critical Rayleigh number is seen as a bifurcation point from the unstable quiescent solution. The experimental determination of critical Rayleigh numbers is often affected by the presence of vertical sidewalls and the review by Azouni³ deals with the modulation of sidewalls on convection.

Stork and Müller⁴ performed experiments to determine the critical conditions at the onset of convection, and they compared their results with calculations of Charlson and Sani.⁵ Some of these calculations were recently corrected and extended by Hardin *et al.*⁶ An important observation that can be made from these calculations is that at critical conditions two azimuthal modes can coexist at certain aspect ratios. These are called codimension two points, and it turns out that they are spaced well apart at small aspect ratios (radius/height), but occur more frequently as the aspect ratio increases. It is also seen from these calculations that as the aspect ratio increases the various bifurcation points corresponding to various azimuthal modes lie close to each other.

The experimental verification of the calculations is the main reason for our interest in this problem. Most experiments were performed by applying a series of temperature differences across a bounded liquid layer and visualizing the flow to determine the onset state. It can be seen from the definition of the Rayleigh number that when experiments are conducted in deep liquid layers, the critical temperature differences become very small (scaling inversely with the cube of depth). However, the time constant to reach steady conditions increases quadratically. Consequently, we may ask

whether any adverse effects can occur by lowering the liquid depth so as to get better temperature control across the liquid layer, thereby reducing the time constant so that frequent changes of experimental conditions can then become possible. The main consideration is that the thermophysical properties can now vary considerably over the liquid height. While it is evident that the critical Rayleigh number will now deviate from the predictions of classical theory that assumes constant properties, it is not so clear how the patterns will change and in what regions of aspect ratio these changes will be prominent. The purpose of this paper is to provide the evidence, both numerically and experimentally, which illustrates that viscosity variation does affect the position of the codimension two points. A part of this study is devoted to the numerical modeling of nonlinear three-dimensional (3-D) convection showing the patterns near the onset for fluids of constant thermophysical properties. Additionally, the effect of temperature-dependent viscosity on flow patterns is shown numerically along with experimental verification.

II. THE EXPERIMENTAL APPARATUS

A schematic of the experimental test unit is shown in Fig. 1. Experiments were conducted with Dow Corning silicone oil sandwiched between two plates. The lower boundary was made of anodized aluminum (thickness=3 mm),

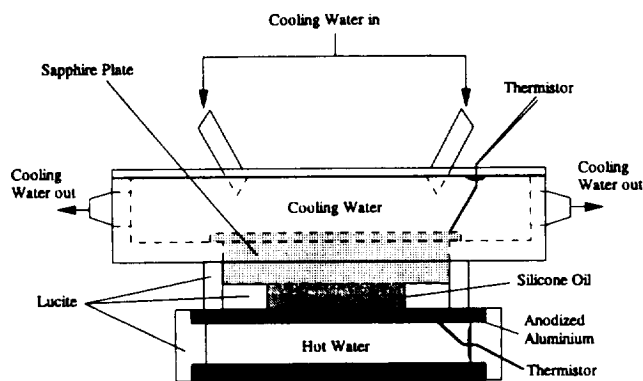


FIG. 1. Schematic of experimental apparatus for Rayleigh convection.

TABLE I. The properties of the Dow Corning silicone oil used in the experiments.

Thermal conductivity	0.001 588 W/cm K
Specific heat	1.463 J/g K
Density	0.968 g/cm ³
Thermal diffusivity	0.001 cm ² /s
Kinematic viscosity at 35 °C	0.697 cm ² /s
Thermal expansion coefficient	0.000 96/K

while the upper boundary was an optically transparent sapphire (thickness = 10 mm). Flow visualization was made possible by aluminum flakes that were dispersed throughout the oil. The sidewalls were precisely machined Lucite. The oil was deaired under vacuum so as to remove most of the entrapped air. It was then loaded into the test section, taking care to avoid the presence of bubbles. The dimensions of the test section were measured with a micrometer and were accurate within 0.1 mm. The lower side of the anodized aluminum plate was in contact with a uniformly stirred water bath, which, in turn, was heated from below by an electric resistance heater. The bath was filled with water and bubbles were removed. It was felt that a uniformly stirred bath under the test section was better than direct contact of the aluminum plate with a resistance heater, as we were interested in avoiding externally imposed thermal signatures on the test section. The upper sapphire plate was in contact with a continuously flowing water bath. The temperature difference across the test section was assumed to be the temperature drop between the lower surface of the aluminum plate and the upper surface of sapphire, as both aluminum and sap-

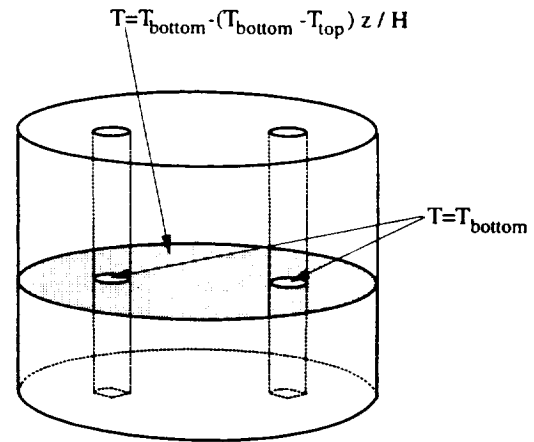


FIG. 3. The 3-D temperature disturbance used in the calculations.

phire have large conductivities compared to the silicone oil. The thermophysical properties of the Dow Corning silicone oil used are given in Table I. Lucite has same thermal diffusivity as silicone oil within a percent and is 12%–15% more thermally conductive. Thus, the temperature gradients in the sidewalls and working fluid, i.e., silicone oil are very close, leading to a “conducting sidewall” thermal boundary condition. We will observe in a later section that the main results of this paper do not depend significantly whether the sidewall thermal condition is insulating or conducting. It may be noted that the thermal diffusivities of aluminum (0.97 cm²/s) and highly conductive sapphire (0.1633 cm²/s) are large compared to silicone oil, and so the time constants for a temperature change to establish steady conditions in these solid plates were quite short. The temperature differences were measured with a pair of resistance temperature detectors attached to the water bath side of aluminum and sapphire plate. They were calibrated by an Omega 700 thermistor with the accuracy for temperature difference measuring within a 0.05 °C. The dynamic viscosity of silicone oil versus temperature is given as $\mu = 0.004 471 86 e^{1545.11/T} \text{ g/cm s}$. This came from the viscosity measurement at several temperature levels. The dynamic viscosity was measured in a coaxial cylinder, normal open cup Haake RV-12 and the viscosity measurements were accurate within 4%, assuming Newtonian behavior. The water temperature in the bath above the sapphire plate was controlled at a fixed point, while the water temperature in the bath below the aluminum plate was changed according to the heating patterns for each experimental run. The temperature differences across the test section were controlled with a PID

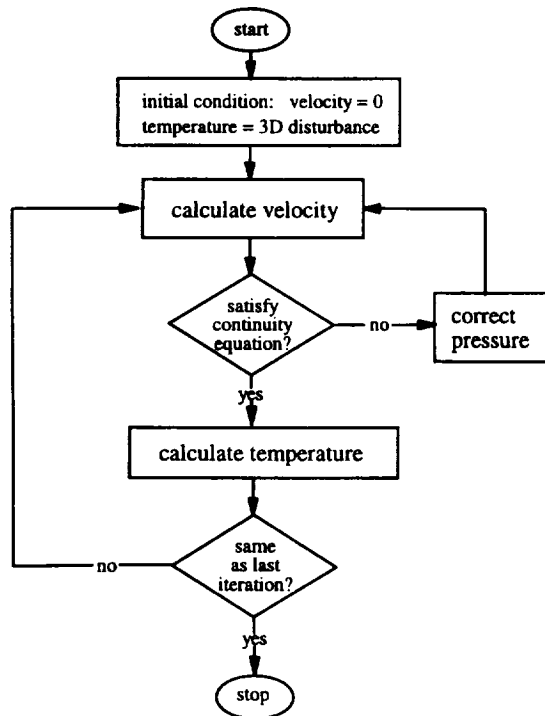


FIG. 2. The flow chart of the calculation procedure.

TABLE II. The onset Rayleigh number and flow pattern indices reported by Hardin *et al.*⁶

R/H	Critical Ra	Flow pattern
1	2260	(0,2)
1.8	1835	(1,3)
2.5	1781	(0,4)
0.75	2592	(1,1)

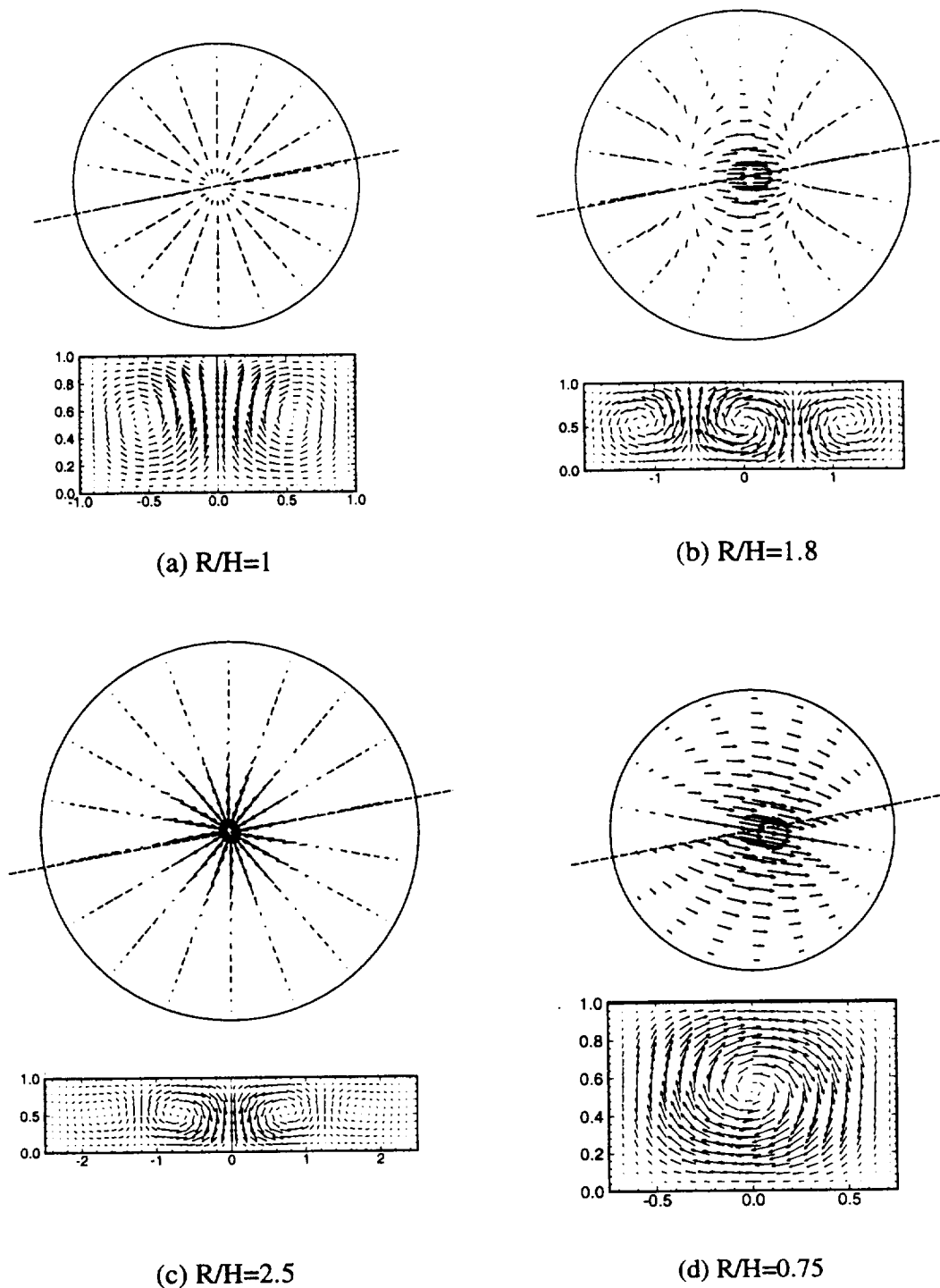


FIG. 4. The flow patterns from the calculations with constant viscosity: (a) $R/H=1$, $Ra=2270$; (b) $R/H=1.8$, $Ra=1900$; (c) $R/H=2.5$, $Ra=1800$; and (d) $R/H=0.75$, $Ra=2600$.

controller, which was tuned for the experimental conditions. The heating pattern in all of the experimental runs consisted of several segments at different values of temperature differences around the onset point, and each of them had a slow ramping-up period and a constant temperature difference period greater than four times the thermal time constants of the test section. These time constants were calculated from the thermal diffusivity and the largest length scale in the test section.

III. THE MODEL

The calculation was performed in a cylindrical coordinate system where z is the vertical coordinate. The governing equations are of the well-known Boussinesq form, except that the viscosity is taken to be a function of temperature. On scaling the governing equations in a manner similar to Hardin *et al.*,⁶ the following definition of Rayleigh number (Ra) is arrived at $Ra = \beta g \Delta T H^3 / \kappa \nu$. Here, H is the depth of the

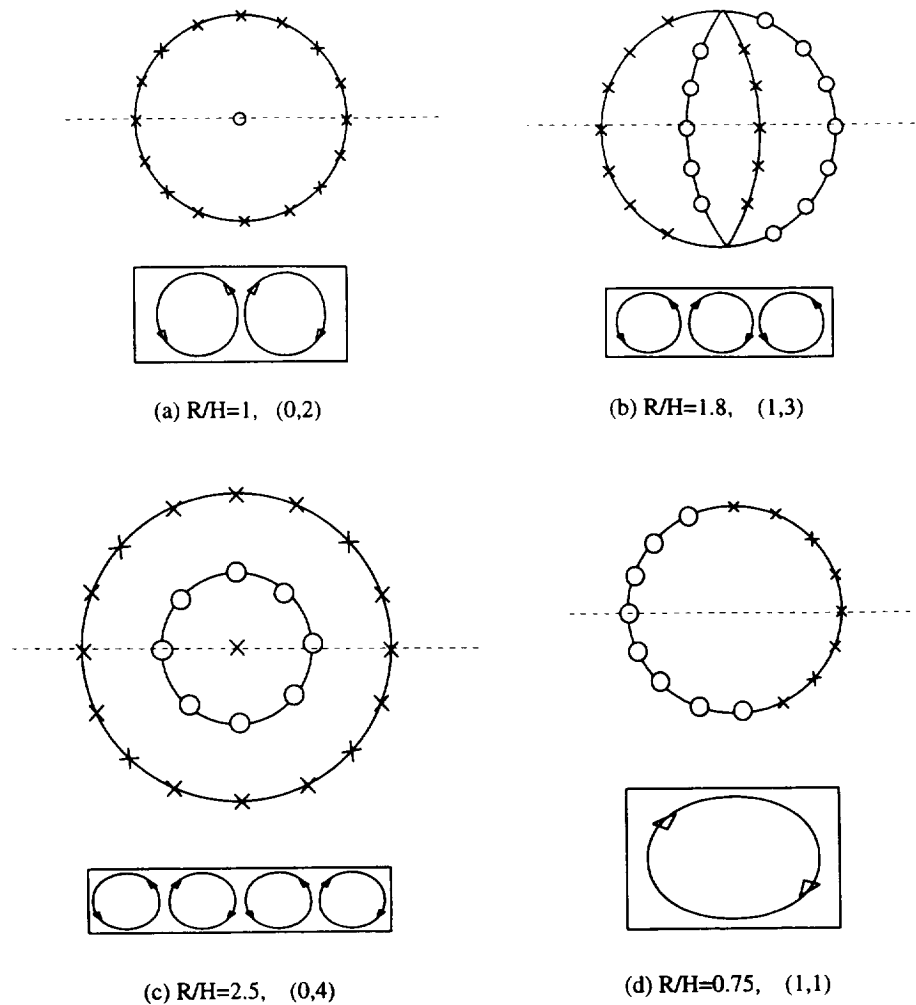


FIG. 5. The schematics of flow patterns from Hardin *et al.*⁶ (a) $R/H=1$, (b) $R/H=1.8$, (c) $R/H=2.5$, and (d) $R/H=0.75$. Here \times indicates the falling fluid while \circ indicates the rising fluid.

fluid and ΔT is the temperature drop across it, g is the gravitational constant, β is the thermal expansion coefficient, which is positive, and ν and κ are kinematic viscosity and thermal diffusivity at a reference temperature.

The density was taken to be linearly dependent upon temperature, based on information from the Dow Corning Company that supplied the oil. The other thermophysical properties were obtained from the Dow Corning Company and are reported to be insensitive to temperature changes within the range used in this study. It is for this reason that only the viscosity variation with temperature was considered important in this study.

The boundary conditions assumed no slip and no flow on velocities at the rigid surfaces, with vanishing temperature perturbations at the horizontal boundaries. Along the vertical boundaries most of the calculations assumed insulating sides, even though thermally conducting sidewall conditions that used a constant temperature gradient in the solid vertical walls would be more appropriate. As mentioned later, the conclusions of this investigation did not change very much when insulating vertical sidewall conditions were used.

The SIMPLE⁷ (Semi-Implicit Method for Pressure Linked Equations) algorithm was employed to carry out the nonlin-

ear calculations. The flow chart in Fig. 2 shows the procedure of the calculation.

IV. DISCUSSION OF THE RESULTS

In order to test the accuracy of the model, the computations were performed for the classical Rayleigh problem, by which is meant a closed, rigid, and circular cylinder containing a "Boussinesq" fluid heated from below and insulated along the vertical sides. As the model is a nonlinear 3-D simulation, no attempt was made to obtain the exact bifurcation point. Instead, the Rayleigh number was an input parameter to the model. A 3-D disturbance on the linear distribution of temperature was introduced to generate the onset of convection. Figure 3 shows the temperature distribution as an initial condition for the calculations. The initial temperature distribution was horizontally uniform at a value that was linear in the z direction, except the two areas marked, where it was equal to the bottom temperature. The resulting steady pattern was calculated from this disturbance. When the Rayleigh number was close to the bifurcation point reported by Hardin *et al.*,⁶ the predicted pattern was identical to what

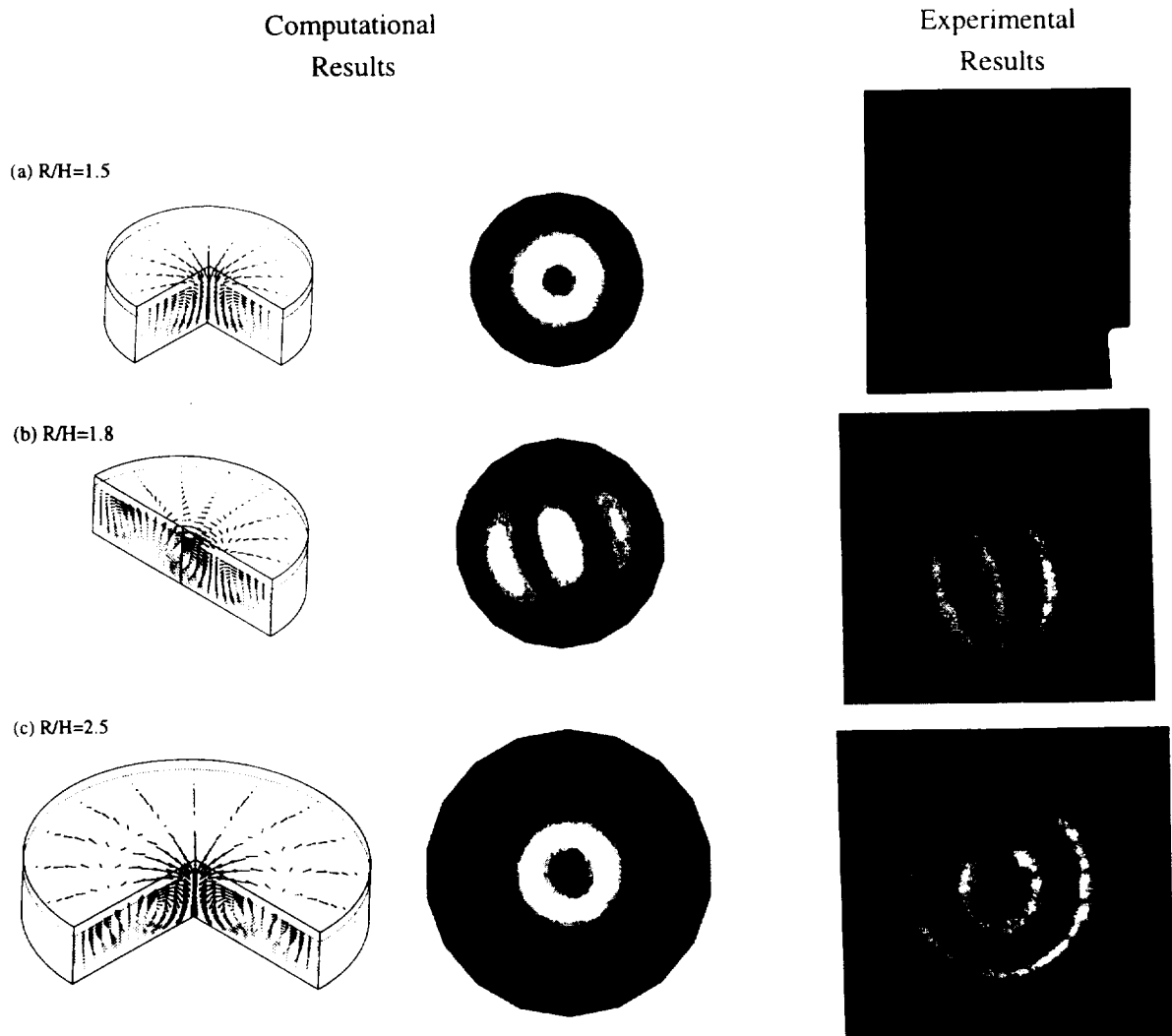


FIG. 6. The comparison of flow patterns between experiments and the calculations with a variation of viscosity: (a) $R/H=1.5$, $\Delta T=19.0$ °C; (b) $R/H=1.8$, $\Delta T=18.5$ °C; and (c) $R/H=2.5$, $\Delta T=18.0$ °C.

was reported by them. A quantitative comparison of the velocity and temperature field was not possible, as Hardin *et al.*⁶ did not report this aspect of their study. The results of our calculations are given in Figs. 4(a)–4(d) and those of Hardin *et al.*⁶ are given in Table II for a variety of aspect ratios (R/H), where R is the radius of the test section. Note that two graphs, with the top view and cross section, are presented for each case in Fig. 4. The location where the cross-section graph was made is indicated by a dashed line in the top view graph. The input Rayleigh numbers for each case are shown in the caption of Fig. 4. Table II contains the bifurcation point and the pair of indices that shows the flow structure at onset. The first index represents the azimuthal mode number while the second index represents the maximum number of roll cells across the diameter of the cylindrical test section. For example, a flow mode (0,2) represents the schematic shown in Fig. 5(a), while mode (1,3) is seen in Fig. 5(b), mode (0,4) in Fig. 5(c), and mode (1,1) in Fig. 5(d). Again, two graphs are presented for each case in Fig. 5. In the top view graph, the circles indicate the flow coming up from the plane of the paper, while the crosses show the flow going down into the plane. It may be observed that the re-

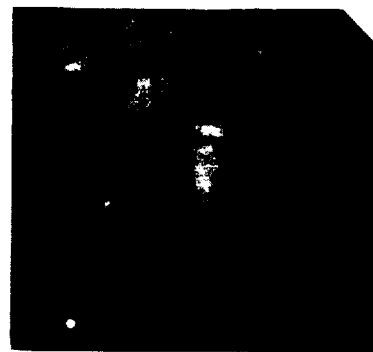
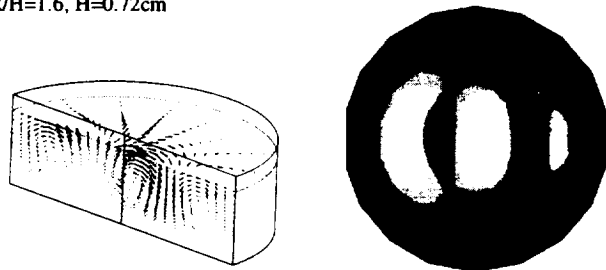
sults of the calculations as shown in Fig. 4 are in good agreement with those given in Table II and Fig. 5.

The next phase of the study involved the experimental determination of the patterns and comparison with the numerical modeling. Experiments were conducted in a variety of aspect ratios, and since the viscosity varied across the depth of the layer, our interest was focused on the patterns that would evolve as a result of this complication. Calculations were done so as to incorporate the viscosity variation. The results of this comparison are shown in Figs. 6(a)–6(c) for aspect ratios of 1.5, 1.8, and 2.5, respectively. The calculation results are shown in two graphs for each case: (1) a 3-D flow pattern at the outer surfaces of a part of the cylinder, and (2) a flow plan at a constant “ z ” plane near the top. Experimental results are presented by the photographs taken from the top of the test section. In these photographs, the white regions are the locations where mainly horizontal flows occurred, while the black regions were occupied by mainly vertical flows. In each case, the comparison is excellent. The experimental runs were repeatable and the same working fluid was used in each experimental run. The flow visualization was made possible by the introduction of alu-

Computational
Results

Experimental
Results

(a) $R/H=1.6$, $H=0.72\text{cm}$



(b) $R/H=1.6$, $H=0.42\text{cm}$



FIG. 7. The comparison of computational results and experimental results at the aspect ratio near the codimension two point: (a) $R/H=1.6$, $H=7.2$ mm, $\Delta T=3.9$ °C; (b) $R/H=1.6$, $H=4.2$ mm, $\Delta T=19.9$ °C.

minum flakes, which were in the submicron range size into the liquid so as to form a uniform slurry. The difference in the numerical results shown in Fig. 4 and Fig. 6 is that the latter assumed a viscosity variation. Even though the actual experiment simulated the conducting sidewall case, the model reflected the insulating sidewall case. In fact, a separate calculation with the conducting sidewall case for aspect ratios 1.5 and 1.8 showed very little discernible change in patterns from the result, where an insulating wall condition was used. The comparison given in Fig. 6 is very encouraging, and there seems to be very little to distinguish these results from the perfect Rayleigh problem results of Figs. 4(b) and 4(c). Because the viscosity variation was taken into account, the comparison between experiments and model are shown for the actual temperature difference (ΔT) used in our experiment.

This raises the question of what effect, if any, the viscosity variation has on the patterns at onset. It is surmised that the location of a codimension two point must be predictably affected. A codimension two point is one where two modes coexist for the same critical Rayleigh number. In other words, it is the aspect ratio at which a switch in patterns takes place from one state to another. Straughan⁸ has shown in the case of an unbounded layer of fluid that the critical wave number is reduced when a viscosity variation

with temperature is assumed. This observation should therefore immediately translate into a shifting of the codimension two point to the right, i.e., toward larger aspect ratio, at least for the case of a cylinder with artificial conditions of vorticity free sidewalls. It is to be noted that the unfolding of the critical Rayleigh number versus wave number curve into the relationship between Rayleigh number and aspect ratio has been used in the past by Charlson and Sani⁵ and Rosenblat,⁹ among many others. To test the hypothesis that the codimension two point would be shifted to the right if a fluid of varying viscosity were used, a number of experiments were conducted in various aspect ratios with tall and short heights of liquid layers. The corresponding calculations were made with the assumption of insulating sidewalls as the position of the codimension two point depends only slightly on this change. For example, Hardin *et al.*⁶ report that the codimension two point for conducting walls occurs at an aspect ratio of 1.59 and at an aspect ratio of about 1.58 for the case of insulating sidewalls. According to the calculations of Hardin *et al.*,⁶ a flow mode of (0,2) should occur immediately to the left of the computed codimension two point, while a mode of (1,3) should occur immediately to the right. Figure 7 shows the comparison of patterns between modeling and experi-

ment for an aspect ratio of 1.6 for a tall fluid height of 7.2 mm, with a temperature difference of 3.9 °C and for a short fluid height of 4.2 mm, with a temperature difference of 19.9 °C. The comparison between modeling and experiments is again very good and a remarkable change in patterns was observed. The tall fluid set into a mode (1,3) and the short fluid set into a mode of (0,2), indicating that the codimension two point had shifted to the right when a larger temperature difference was introduced, such that the variation of viscosity became large enough to make the shifting distinguishable. This observation thereby agreed qualitatively with our forecast, which, in turn, was based on the calculations of Straughan⁸ for a laterally unbounded fluid.

V. SUMMARY

Comparison of experimental results with results of detailed 3-D calculations for Rayleigh convection in a closed cylinder was made. Very good agreement was obtained between theory and experiment. The viscosity variation did not affect the onset flow patterns significantly from the constant viscosity case, except at the vicinity of the codimension two points. Based on the theoretical prediction of Straughan⁸ for a laterally unbounded fluid, it was conjectured that the codimension two points would shift toward larger aspect ratios if viscosity variation were to be considered. This conjecture was shown to be correct in our study and once again we obtained excellent agreement between experiment and the corresponding numerical modeling.

ACKNOWLEDGMENTS

We acknowledge the National Science Foundation (NSF) for supporting A. X. Zhao under NSF Grant No. CTS-9307819, and NASA for supporting F. C. Moates and R. Narayanan under Grant No. NAG-1-1474. The computations were performed on the CRAY/C90 at the Pittsburgh Supercomputing Center.

¹S. Chandrasekhar, *Hydrodynamic and Hydromagnetic Stability* (Dover, New York, 1961).

²E. L. Koschmieder, *Bénard Cells and Taylor Vortices* (Cambridge University Press, Cambridge, 1993).

³M. A. Azouni, "Survey of thermoconvective instabilities of confined fluids," *J. Non-Equilibrium Thermodyn.* **4**, 321 (1979).

⁴K. Stork and U. Müller, "Convection in boxes: Experiments," *J. Fluid Mech.* **54**, 599 (1972).

⁵G. S. Charlson and R. L. Sani, "Thermoconvective instability in bounded cylindrical fluid layer," *Int. J. Heat Mass Transfer* **13**, 1479 (1970).

⁶G. R. Hardin, R. L. Sani, D. Henry, and B. Roux, "Buoyancy-driven instability in a vertical cylinder: Binary fluids with Soret effect. Part I: General theory and stationary stability results," *Int. J. Num. Meth. Fluids* **10**, 79 (1990).

⁷S. V. Patankar, *Numerical Heat Transfer and Fluid Flow* (Hemisphere, New York, 1980).

⁸B. Straughan, "Stability criteria for convection with large viscosity variations," *Acta Mech.* **61**, 59 (1986).

⁹S. Rosenblat, "Thermal convection in a vertical cylinder," *J. Fluid Mech.* **122**, 395 (1982).